# Estudio teórico de los procesos fotofísicos de la metilfeoforbida a

# Theoretical study of photophysical processes of methylpheophorbide a

Hernán Darío Rueda Bueno

A thesis submitted in partial fulfillment of the requirements for the degree of Master of Science in Chemistry

Masters dissertation

Advisors

Martha Cecilia Daza Espinosa

Dra. en Ciencias-Química

Markus Hans Oliver Doerr

Dr.rer.nat.

Universidad Industrial de Santander

Facultad de Ciencias

Escuela de Química

Bucaramanga

2025

*To my mother, Patricia Bueno ,*

*whom I'm grateful for her love and support during this process.*

*To the loving memory of my grandparents,*

*Gabriel Bueno and Carmen Mogollón.*

**Acknowledgments**

Well, well, well, it is time to write acknowledgments. First of all, I would like to express my deepest gratitude to my supervisors Prof. Dr. Martha Daza and Prof. Dr. Markus Doerr for guiding me through the intricacies of my research. Thank you for your patience, support, and confidence over these years.

Moreover, I would like to express my deepest appreciation to the jury. Specially to Prof. Jhon Perez and Enrique Mejía for offering valuable insight and support during our discussions about photophysics. Then, I want to specially thank my office colleagues Marlon Suárez, Juan Camilo Reyes, Pedro Guzmán and Frank Moreno, with whom I had a great time working, who taught me so many helpful tips, tricks, and rich discussions about the project. Thanks should also go to Patricia Cuevas, Laura Pérez and Karol Chanagá, whom encouraged me along the project, specially during the writing process of the paper.

I'd also like to extend my gratitude to Nathalia Buitrago, who also encouraged me along the project and even helped me to improve my graphical abstract for my first paper.

Going on, I'd also like to extend my gratitude to Prof. Alirio Palma and Prof. Lina Acosta who still make a regular appearance to motivate me. Next, I also wish to thank Diana Ardila, Diana Vera, Geraldine Álvarez and Diego Rodríguez, who encouraged me during the realization of the project and the writing process of the paper.

I would like to extend my sincere thanks to my family and friends for their support. A special thanks go to Álvaro Hernández, Carlos Ordoñez, Camilo Caballero, David Botero, Brayan Grimaldos and Santiago Ramírez for the nice conversations, support, and believing in my abilities. Without their uplifting spirit this project would not be possible.

我还要感谢中文。最初学习中文只是作为一种爱好，让我能从日常的计算工作中抽离喘息。但渐渐地，它让我能在中文论坛里解决一些关于系间窜越的问题，并结识了一个充满趣味与善意的文化。

最后，感谢您——我亲爱的读者，愿意花时间阅读这些致谢，甚至翻译这段文字。愿这份求知欲能伴你一生，引领你追求更美好的生活。

**Table of contents**

## List of tables

## List of figures

## List of abbreviations

**AH** Adiabatic Hessian

**AHAS** Adiabatic Hessian After a Step

**ACQ** Agreggation-Caused Quenching

**AIE** Agreggation-Induced Emission

**BO** Born-Oppenheimer

**C-PCM** Conductor-like Polarizable Continuum Model

**DFT** Density Functional Theory

**DFT/MRCI** Density Functional Theory/Multireference Configuration Interaction

**DLPNO-STEOM-CCSD** Domain Based Local Pair Natural Orbitals implementation of the similarity transformed equation of motion coupled cluster theory with single and double excitations

**FC** Franck-Condon Approximation

**FCHT** Franck-Condon-Herzberg-Teller Approximation

**GGA** Generalized Gradient Approximation

**HF** Hartree-Fock

**INLINEW** Gaussian Line Width

**ISC** Intersystem Crossing

**LDA** Local Density Approximation

**LIP** Linearly Interpolated Pathway

**LSDA** Local Spin Density Approximation

**MCD** Magnetic Circular Dichroism

**MPh** Methylpheophorbide a

**NIR** Near-Infrared

**PDT** Photodynamic Therapy

**PS** Photosensitizer

**QDPT** Quasi-Degenerate Perturbation Theory

**ROS** Reactive Oxygen Species

**SCF** Self-Consistent Field

**SOC** Spin-Orbit Coupling

**SOCME** Spin-Orbit Coupling Matrix Element

$\partial$**SOCMEs** First-order derivatives of the SOCMEs with respect to the normal mode coordinates

**SPECRES** Spectral Resolution

**TD-DFT** Time-Dependent Density Functional Theory

**TDA** Tamm-Dancoff Approximation

**TDM** Transition Dipole Moment

**VEE** Vertical Excitation Energy

**VG** Vertical Gradient

**WFT** Wave Function Theory

## ABSTRACT

**TITLE:** Theoretical study of photophysical processes of methylpheophorbide a*

**AUTHOR:** Rueda Bueno, Hernán Darío**

**KEYWORDS:** Chlorin, methylpheophorbide, photophysics, fluorescence, phosphorescence, intersystem crossing.

**DESCRIPTION:** Pheophorbide a is a dephytylation and demetallation product of chlorophyll a isolated from plants and algae. Pheophorbide a has been used as a photosensitizer to treat microbes, cancer and multidrug resistance. Methylpheophorbide a (MPh) is another photosensitizer with interesting photophysical properties such as stronger absorption at longer wavelengths compared to the absorption of porphyrins and a high singlet oxygen production quantum yield ($\Phi_{\Delta} = 0.62$). To gain deeper insight into the photophysics of MPh, two computational protocols were employed to elucidate the photophysical properties of methylpheophorbide a (MPh). These protocols use Fermi' s golden rule within a path integral formalism. Time-dependent density functional theory (TD-DFT) calculations at the CAM-B3LYP/def2-SVP(C-PCM) level of theory were performed. Our calculations reproduce reasonably well the vibronic structure of the Q-band of the absorption spectrum of MPh. After photoexcitation, MPh can decay to the ground state via fluorescence or it can undergo intersystem crossing. Three triplet excited states ($T_1$, $T_2$ and $T_3$) are found below the $S_1$ state with an overall spin-vibronic ISC rate constant of $4.61 \times 10^7$ $s^{-1}$ and $6.14 \times 10^7$ $s^{-1}$ for the first and second protocol, respectively, in good agreement with the experimental value of $7.90 \times 10^7$ $s^{-1}$. While the calculated fluorescence rate constant by employing the first protocol is about four times higher than the experimental value, the second protocol predicted a calculated fluorescence rate constant five times higher than the experimental value. Consistent with the experimentally observed behavior, our calculations predict that MPh is not phosphorescent.

## RESUMEN

**TÍTULO** Estudio teórico de los process fotofísicos de la metilfeoforbida a*

**AUTOR:** Rueda Bueno, Hernán Darío**

**PALABRAS CLAVE:** Clorina, metilfeoforbida, fotofísica, fluorescencia, fosforescencia, entrecruzamiento de sistemas.

**DESCRIPCIÓN:** La feoforbida a es un producto de desfitilación y demetalación de la clorofila a aislada de plantas y algas. La feoforbida a se ha utilizado como fotosensibilizador para combatir microbios, cáncer y resistencia a múltiples fármacos. La metilfeoforbida a (MPh) es otro fotosensibilizador con interesantes propiedades fotofísicas, como una absorción más fuerte a longitudes de onda más largas en comparación con la absorción de porfirinas y un alto rendimiento cuántico de producción de oxígeno singlete ($\Phi_\Delta$ = 0.62). Para profundizar en la fotofísica de MPh, se empleó un protocolo computacional que permite la elucidación de las propiedades fotofísicas de la metilfeoforbida a (MPh). Este protocolo utiliza la regla de oro de Fermi dentro de un formalismo de integral de camino. Se realizaron cálculos utilizando la teoría del funcional de la densidad dependiente del tiempo (TD-DFT) en el nivel de teoría CAM-B3LYP/def2-SVP(C-PCM). Nuestros cálculos reproducen aceptablemente bien la estructura vibrónica de la banda Q del espectro de absorción de MPh. Después de la fotoexcitación, MPh puede decaer al estado fundamental mediante fluorescencia o puede experimentar entrecruzamientos de sistemas. Se encontraron tres estados excitados triplete ($T_1$, $T_2$ y $T_3$) por debajo del estado $S_1$con una constante de velocidad ISC vibrónica de espín de 4.61 x $10^7$ $s^{-1}$ y 6.14 x $10^7$ $s^{-1}$ para el primer y segundo protocolo, respectivamente, de acuerdo con el valor experimental de 7.90 x $10^7$ $s^{-1}$. Mientras que el cálculo de la constante de velocidad de fluorescencia al emplear el primer protocolo es aproximadamente cuatro veces mayor que el valor experimental, el segundo protocolo predijo una constante de velocidad de fluorescencia calculada cinco veces mayor que el valor experimental. Consistente con el comportamiento observado experimentalmente, nuestros cálculos predicen que la MPh no es fosforescente.

## Introduction

Photosensitization is a process where a substance, known as a photosensitizer (PS), absorbs light and subsequently transfers the energy to other molecules, typically oxygen, in its environment. Among the vast number of photosensitizers, methylpheophorbide a (MPh) (Figure 1) is a prominent photosensitizer due to its low dark cytotoxicity(Ha et al., 2022) and remarkable phototoxicity.(Ha et al., 2022; Wang et al., 2014) Methylpheophorbide a derivatives are widely used as antiviral(Jimenez-Aleman et al., 2021) and antiparasitic agents,(Miranda, Gerola, et al., 2017; Miranda, Volpato, et al., 2017) fluorescent probes,(Ryazanova et al., 2020; Yasuda et al., 2018) in the phototransformation of organic contaminants(Luo et al., 2018) and in photodynamic therapy (PDT).(Aksel et al., 2020; Miranda, Gerola, et al., 2017; Miranda, Volpato, et al., 2017; Saide et al., 2020) PDT is a therapeutic approach in which a photosensitizer (PS) is irradiated with light, leading to reactive oxygen species (ROS) formation via energy transfer from the lowest triplet excited state to triplet oxygen. An ideal photosensitizer should display low systemic and dark toxicity, strong absorption bands at low energy (NIR to red visible light) to reach and treat deep tumors,(Aksel et al., 2020; Miranda, Volpato, et al., 2017; Saide et al., 2020; Szurko et al., 2009) and a high quantum yield of singlet oxygen formation.(Szurko et al., 2009) In order to enhance the production of singlet oxygen, it is crucial that the intersystem crossing process from the highest triplet excited state to the lowest triplet excited state is favoured. A general approach to enhance the ISC process is to reduce aggregation-caused quenching (ACQ). Aggregates appear in aqueous media due to the formation of intermolecular $\pi-\pi$ stacking among photosensitizer molecules.(Liu et al., 2022) Therefore, coupling a PS with nanotechnology such as nanoparticles and liposomes may increase the solubility in water and solve the problem.(Gunaydin et al., 2021) An alternative method to prevent ACQ is to increment the aggregation-induced emission (AIE) by constraining molecular movement.(Pang et al., 2022) In doing so, $\pi-\pi$ stacking is avoided, being ISC the only

dominant non-radiative channel.(Liu et al., 2022; Meng et al., 2022)

Another important application of pheophorbide a derivatives is in the design of fluorescent probes.(Ryazanova et al., 2020; Yasuda et al., 2018) A prerequisite for the design of a fluorescent probe is the selection of a suitable fluorescent dye that exhibits good stability, low toxicity, and selective fluorescence enhancement for the recognition of the target chemical species.(Jiang et al., 2023) Despite the small spin-orbit coupling matrix elements (SOCMEs) exhibited by the free-base porphyrin,(Perun et al., 2008), free-base porphin,(Kleinschmidt et al., 2006) and chlorins, it is known that for the latter system, fluorescence and intersystem crossing are competitive processes.(Bhandari et al., 2021)

The use of computational studies may prove advantageous in improving the photophysical properties of certain molecules. However, due to the size of these systems, the application of efficient computational protocols is a necessity. In the existing literature, there are few computational studies about the photophysical processes of tetrapyrrolic systems. Common computational methods used to study the photophysics of these systems include the combination of density functional theory/multireference configuration interaction (DFT/MRCI) and the combination of density functional theory and time-dependent density functional theory (DFT/TD-DFT). The photophysical properties at the ground state geometry of chlorin derivatives, such as vertical excitation energy (VEE) and UV-Vis spectra, have previously been investigated within the framework of density functional theory (DFT) and time-dependent density functional theory (TD-DFT).(Parusel and Grimme, 2000, 2001; Shrestha et al., 2016; Zhang and Stillman, 2018; Zhang et al., 2017). A quantum chemical investigation of the vibronic structure of the absorption spectrum of a porphyrin derivative has recently been performed by Sirohiwal and coworkers applying the DLPNO-STEOM-CCSD and DFT/TD-DFT methods.(Sirohiwal et al., 2020) to compute VEEs and the vibronic structure. In a study by Reimers et al. the vibronic structure of the absorption spectra of porphyrin derivatives has

been investigated employing the CAM-B3LYP functional.(Reimers et al., 2013, 2022). In addition to the vibronic structure of the absorption spectrum of porphyrins, the ultrafast decay within the Q-bands of a chlorophyll-a derivative has been investigated.(Reiter et al., 2022) Other investigations have been focused on the study of photophysical processes. Perun and coworkers calculated the TD-DFT and (DFT/MRCI) vertical excitation energies at the ground state geometry and the adiabatic excitation energies of the lowest excited states of free-base porphyrin. The latter method was also employed to compute the SOCMEs and the ISC rate constant.(Perun et al., 2008) Recently, Bhandari and coworkers used a DFT/TD-DFT protocol to calculate the ISC rate constant ($k_{ISC}$), the absorption spectrum and the fluorescence rate constant ($k_F$) of porphine, bacteriochlorin and chlorin systems.(Bhandari et al., 2021)

Experimentally the photophysical properties of MPh have been investigated by Wang and coworkers,(Wang et al., 2014) who determined the singlet oxygen quantum yield ($\Phi_\Delta = 0.62$), the intersystem crossing ($k_{ISC} = 0.79 \times 10^8\ s^{-1}$) and fluorescence ($k_F = 0.32 \times 10^8\ s^{-1}$) rate constants.

In this work, we employed a recently developed path integral approach(de Souza et al., 2018, 2019) based on time-dependent density functional theory (TD)-DFT to elucidate the decay processes of methylpheophorbide a in toluene, and to test assess the suitability of these methodologies for describing the photophysical properties of this system.

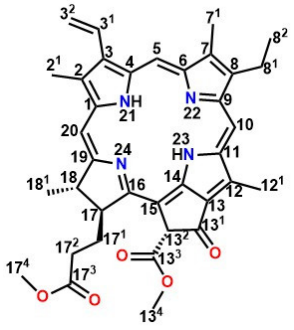

**Figure 1.** Chemical structure of methylpheophorbide a (MPh).

# 1 Objectives

## 1.1 General objective

Contribute to the rational design of methylpheophorbide a derivatives for photodynamic therapy and pollutants decomposition.

## 1.2 Specific objectives

- Choose the best functional and basis set to calculate the fluorescence, phosphorescence and intersystem crossing rate constant of methylpheophorbide a.
- Compute the absorption and emission spectra of methylpheophorbide a.

# 2 Conceptual framework

## 2.1 Overview

The aim of this chapter is to summarize the conceptual framework of molecular quantum mechanical methods that were used in this research project.

## 2.2 Quantum chemical methods

### 2.2.1 The non-relativistic Schrödinger equation and the Born-Oppenheimer approximation

The current electronic structure methods can be classified in two main approaches: wave function theory (WFT) and density functional theory (DFT).(Hohenberg and Kohn, 1964; Kohn and Sham, 1965; Runge and Gross, 1984)

The wave function $\Psi_i$(R,r) of any atomic or molecular system is a function that defines all observable physical quantities. This information is found by applying certain mathematical procedures (operators) to the function. Once the wave function is found, all the observables of the atom or molecule can, in principle, be determined. This wave function is computed by solving the Schrödinger equation Eq.(1)

$$\hat{\mathrm{H}}\Psi_{\mathrm{i}}(\mathrm{R},\mathrm{r}) = \mathrm{E}_{\mathrm{i}}\Psi_{\mathrm{i}}(\mathrm{R},\mathrm{r}) \tag{1}$$

In Eq.(1) $\hat{\mathrm{H}}$ is the complete electronic Hamiltonian of the system and corresponds to the operator for the energies $\mathrm{E_i}$ of a given electronic state i. Each electronic state is associated with a wave function $\Psi_i$(R,r) which depends on the electronic and parametrically on the nuclear coordinates. In order to describe molecular processes it is critically important to specify a molecular Hamiltonian.(Gómez et al., 2020) The complete molecular Hamiltonian operator Eq.(2) in atomic units

is:

$$\hat{H} = \overbrace{-\frac{1}{2}\sum_{i}^{n}\nabla_i^2}^{\hat{T}_e} \overbrace{-\frac{1}{2}\sum_{a}^{m}\nabla_a^2}^{\hat{T}_n} \overbrace{-\sum_{a}^{m}\sum_{i}^{n}\frac{Z_a}{|R_a - r_i|}}^{\hat{V}_{ne}} + \overbrace{\sum_{i}^{n}\sum_{j>i}^{n}\frac{1}{|r_i - r_j|}}^{\hat{V}_{ee}} + \overbrace{\sum_{a}^{m}\sum_{b>a}^{m}\frac{Z_a Z_b}{|R_a - R_b|}}^{\hat{V}_{nn}} \quad (2)$$

Where the terms labeled as $Z_a$ is the nuclear charge, $R_a$ is the coordinate of the nucleus a, $r_i$ is the coordinate of the electron i, m is the total number of nuclei and n is the total number of electrons.

The molecular Hamiltonian operator includes the kinetic energy of the electrons ($\hat{T}_e$), the kinetic energy of the nuclei ($\hat{T}_n$), the Coulombic interactions between electrons and nuclei ($\hat{V}_{ne}$), and the electron-electron ($\hat{V}_{ee}$) and nuclear-nuclear ($\hat{V}_{nn}$) repulsion.

Therefore, the Schrödinger equation can be written as:

$$\Big(\hat{T}_e(r) + \hat{T}_n(R) + \hat{V}_{ne}(R,r) + \hat{V}_{ee}(r) + \hat{V}_{nn}(R)\Big)\Psi_i(R,r) = E_i\Psi_i(R,r) \quad (3)$$

Due to the coupling of nuclear and electronic degrees of freedom, it is not possible to describe the electronic and nuclear motion. Therefore, approximations are applied to study multi-electron systems. The most fundamental approximation is the adiabatic or Born-Oppenheimer (BO) approximation. The BO approximation takes into account the prominent difference in the masses of electrons and nuclei. Due to this difference, the nuclei can be regarded as fixed relative to the motion of the electrons. However, if the nuclei have larger kinetic energies, it is not possible to separate the electronic and nuclear degrees of freedom.(Stanke, 2016)

In the BO approximation, the electronic motion described by the electronic wave function $\psi_i(R,r)$ and the nuclear motion described by the nuclear wave function $\chi_i(R)$ can be separated

and treated independently, Eq.(4).

$$\Psi_{\mathrm{i}}(\mathrm{R},\mathrm{r}) = \psi_{\mathrm{i}}(\mathrm{R};\mathrm{r})\chi_{\mathrm{i}}(\mathrm{R}) \tag{4}$$

The electronic wave function $\psi_{\mathrm{i}}(\mathrm{R};\mathrm{r})$ depends parametrically on the nuclear coordinates and explicitly on the electron coordinates. It is a solution of the electronic Schrödinger equation:

$$\left(\hat{\mathrm{T}}_{\mathrm{e}}(\mathrm{r}) + \hat{\mathrm{V}}_{\mathrm{ne}}(\mathrm{R},\mathrm{r}) + \hat{\mathrm{V}}_{\mathrm{ee}}(\mathrm{r})\right)\psi_{\mathrm{i}}(\mathrm{R};\mathrm{r}) = \mathrm{E}_{\mathrm{i}}(\mathrm{R})\psi_{\mathrm{i}}(\mathrm{R};\mathrm{r}) \tag{5}$$

$\mathrm{E}_{\mathrm{i}}(\mathrm{R})$ is the potential energy of a given nuclear configuration. The computation of the potential energies for all the nuclear configurations allows us to study the potential energy (hyper) surface (PES). This approximation reduces the complexity of the eigenvalue problem Eq.(1). Nevertheless, approximation techniques of the electronic wave function have been implemented to study multi-electron systems.

**2.2.2 The Hartree-Fock approximation** Hartree-Fock (HF) theory is the most basic approximation to compute the wave function and the energy of a multi-electron system. Within the HF theory the electronic wave function is represented by a Slater determinant of single-electron wave functions (spin-orbitals, $\psi_{\mathrm{N}}(\mathrm{x}_{\mathrm{N}})$), which depend on three spatial coordinates and one spin coordinate, collectively represented by $\mathrm{x}_{\mathrm{N}}$. A Slater determinant leads to the fulfillment of the Pauli principle.(Jensen, 2017) However, the electron-electron interaction is not taken into account.

$$\Psi_{\mathrm{HF}}(\mathrm{x}_1,\mathrm{x}_2...\mathrm{x}_\mathrm{i}) = \frac{1}{\sqrt{\mathrm{N!}}}\begin{vmatrix} \psi_1(\mathrm{x}_1) & \psi_2(\mathrm{x}_2) & ... & \psi_\mathrm{N}(\mathrm{x}_\mathrm{N}) \\ \psi_1(\mathrm{x}_1) & \psi_2(\mathrm{x}_2) & ... & \psi_\mathrm{N}(\mathrm{x}_\mathrm{N}) \\ \vdots & \vdots & \ddots & \vdots \\ \psi_\mathrm{N}(\mathrm{x}_1) & \psi_\mathrm{N}(\mathrm{x}_2) & ... & \psi_{\mathrm{N},}(\mathrm{x}_\mathrm{N}) \end{vmatrix} \tag{6}$$

Where $\psi_\mathrm{N}(\mathrm{x}_\mathrm{N})$ is the *N*-th spin-orbital. The determinantal wave function can also be represented by a linear combination of Hartreee products.

$$\Psi_{\mathrm{HF}}(\mathrm{x}_1,\mathrm{x}_2...\mathrm{x}_\mathrm{i}) = |\psi_1(\mathrm{x}_1)\psi_2(\mathrm{x}_2)...\psi_\mathrm{N}(\mathrm{x}_\mathrm{N})\rangle \tag{7}$$

The total energy related to a single Slater determinant is described by the following Hamiltonian within the BO approximation:

$$\hat{\mathrm{H}} = \overbrace{-\frac{1}{2}\sum_\mathrm{i}^\mathrm{n}\nabla_\mathrm{i}^2}^{\hat{\mathrm{T}}_\mathrm{e}} \overbrace{-\sum_\mathrm{a}^\mathrm{m}\sum_\mathrm{i}^\mathrm{n}\frac{\mathrm{Z_a}}{|\mathrm{R_a}-\mathrm{r_i}|}}^{\hat{\mathrm{V}}_\mathrm{ne}} + \overbrace{\sum_\mathrm{i}^\mathrm{n}\sum_{\mathrm{j}>\mathrm{i}}^\mathrm{n}\frac{1}{|\mathrm{r_i}-\mathrm{r_j}|}}^{\hat{\mathrm{V}}_\mathrm{ee}} \tag{8}$$

$$\hat{\mathrm{H}} = \sum_{\mathrm{i}=1}^\mathrm{n}\hat{\mathrm{h}}_\mathrm{i} + \sum_\mathrm{i}^\mathrm{n}\sum_{\mathrm{j}>\mathrm{i}}^\mathrm{n}\frac{1}{|\mathrm{r_i}-\mathrm{r_j}|} \tag{9}$$

The first term in Eq.(9) includes the kinetic energy and the coulombic interactions between electrons and nuclei in the one-electron operator $\hat{\mathrm{h}_\mathrm{i}}$. The second term $\hat{\mathrm{g}}_{1,2} = \frac{1}{|\mathrm{r_i}-\mathrm{r_j}|}$ is the two-electron operator.(Jensen, 2017)

In order to describe the total electronic energy, the coulomb $\hat{\mathrm{J}}_\mathrm{i}$ and the exchange operator $\hat{\mathrm{K}}_\mathrm{i}$ can be expressed as:

$$\hat{\mathrm{J}}_{\mathrm{i}}(\mathrm{x}_1)\,|\psi_{\mathrm{j}}(\mathrm{x}_1)\rangle = \langle\psi_{\mathrm{i}}(\mathrm{x}_2)|\,\hat{\mathrm{g}}_{1,2}\,|\psi_{\mathrm{i}}(\mathrm{x}_2)\rangle\,|\psi_{\mathrm{j}}(\mathrm{x}_1)\rangle \tag{10}$$

$$\hat{\mathrm{K}}_{\mathrm{i}}(\mathrm{x}_1)\,|\psi_{\mathrm{j}}(\mathrm{x}_1)\rangle = \langle\psi_{\mathrm{i}}(\mathrm{x}_2)|\,\hat{\mathrm{g}}_{1,2}\,|\psi_{\mathrm{j}}(\mathrm{x}_2)\rangle\,|\psi_{\mathrm{i}}(\mathrm{x}_1)\rangle \tag{11}$$

The summation over all occupied spin-orbitals leads to the definition of the total Coulomb $\hat{\mathrm{J}} = \sum_{\mathrm{i}} \hat{\mathrm{J}}_{\mathrm{i}}$ and exchange operator $\hat{\mathrm{K}} = \sum_{\mathrm{i}} \hat{\mathrm{K}}_{\mathrm{i}}$ .

Therefore, the total electronic energy can be written as:

$$\mathrm{E} = \sum_{\mathrm{i}} \langle\psi_{\mathrm{i}}|\,\hat{\mathrm{h}}_1\,|\psi_{\mathrm{i}}\rangle + \frac{1}{2}\sum_{\mathrm{i}}^{\mathrm{n}}\sum_{\mathrm{j}}^{\mathrm{n}} \langle\psi_{\mathrm{i}}|\,(\hat{\mathrm{J}} - \hat{\mathrm{K}})\,|\psi_{\mathrm{i}}\rangle \tag{12}$$

According to the variational principle, $\delta\mathrm{E} = 0$, the lowest energy computed by a single Slater determinant is an upper bound of the true ground state of the multi-electron system. This principle, due to the orthonormality constraint, allows us to determine the canonical spin-orbitals which leads to the lowest energy of a Slater determinant. This constrained optimization is performed by using Lagrange multipliers and the resulting orbitals are solutions of the self-consistent field (SCF) equations:

$$\langle\psi_{\mathrm{i}}|\,\hat{\mathrm{F}}\,|\psi_{\mathrm{i}}\rangle = \sum_{\mathrm{i}} \langle\psi_{\mathrm{i}}|\,\hat{\mathrm{h}}_1\,|\psi_{\mathrm{i}}\rangle + \sum_{\mathrm{j}} \langle\psi_{\mathrm{i}}\psi_{\mathrm{j}}|\,|\psi_{\mathrm{i}}\psi_{\mathrm{j}}\rangle \tag{13}$$

$$\langle\psi_{\mathrm{i}}|\,\hat{\mathrm{F}}\,|\psi_{\mathrm{i}}\rangle = \sum_{\mathrm{i}} \langle\psi_{\mathrm{i}}|\,\hat{\mathrm{h}}_1\,|\psi_{\mathrm{i}}\rangle + \overbrace{\langle\psi_{\mathrm{i}}\psi_{\mathrm{j}}|\psi_{\mathrm{i}}\psi_{\mathrm{j}}\rangle}^{\text{coulomb}} - \overbrace{\langle\psi_{\mathrm{i}}\psi_{\mathrm{j}}|\psi_{\mathrm{j}}\psi_{\mathrm{i}}\rangle}^{\text{exchange}} \tag{14}$$

In Eq 14, the second and third term are the Coulomb and Exchange integrals, respectively.

$$\hat{\mathrm{F}}\,\psi_{\mathrm{i}} = \varepsilon_{\mathrm{i}}\,\psi_{\mathrm{i}} \tag{15}$$

where $\hat{\mathrm{F}}$ is the Fock operator. The diagonalization of the Fock matrix implies the determination of the canonical spin-orbitals, which is equivalent to solve the Hartree-Fock equations. However, the diagonalization of the Fock matrix depends on the spin-orbitals, which are eigenfunctions of this operator. Therefore, the solutions of these equations requires an iterative process. Due to the non-trivial process of finding the suitable molecular orbitals, the spin functions of the spin-orbitals are integrated out to obtain spatial orbitals ($\vartheta_{\mathrm{i}}$). Therefore, a wave function is described as linear combinations of spatial orbitals, which are expanded on a set of K known basis functions, $\theta$:

$$\vartheta_{\mathrm{i}} = \sum_{\mu}^{\mathrm{K}} \mathrm{C}_{\mu \mathrm{i}} \theta_{\mu} \tag{16}$$

The main disadvantage of the HF method is the lack of electron correlation, which encompasses static and dynamic correlation.(Ghosh et al., 2018) The static part involves the near-degeneracy of numerous configurations. On the other hand, the dynamic correlation is related to the instantaneous interaction between electrons, which does not exist in the HF theoretical framework.(Jensen, 2017) Hence, the computed HF energy is an upper limit to the exact energy of the system. The difference between the total electronic energy of the system and the HF energy is the correlation energy.(Neese, 2009)

**2.2.3 Density functional theory (DFT)** For large and complex systems, wave function-based methods are not are not affordable due to 3N degrees of freedom (excluding spin) for an N-multielectron system.

$$\rho(\mathrm{x}) = \mathrm{N} \int ... \int |\Psi(\mathrm{x}_1, \mathrm{x}_2, ..., \mathrm{x}_{\mathrm{N}})|^2 \mathrm{dx}_2 ... \mathrm{dx}_{\mathrm{N}} = \mathrm{N} \tag{17}$$

Where $\rho$(r) is a probability density related to the probability of finding any of the N electrons

anywhere on a volume dr with arbitrary spin-orbital x.

In DFT, an artificial single particle system with non-interacting electrons displays three degrees of freedom and an equivalent density to the exact density found in the real system.Casida and Huix-Rotllant, 2012; Neese, 2009 Therefore, DFT is the preferred single reference method to investigate this type of system. It is based on two Hohenberg-Kohn theorems:

1. The ground-state electronic properties are estimated by the electron density $\rho(\mathrm{x})$, which displays one-to-one correspondence with an external potential $\mathrm{V_{ext}}$.

2. The electronic density of the ground state $\rho_0$ is determined using the variational method. (Hohenberg and Kohn, 1964)

Accordingly, the electronic ground state energy can be written as

$$\mathrm{E}_0[\rho_0] = \mathrm{T}[\rho_0] + \mathrm{V_{ne}}[\rho_0] + \mathrm{V_{ee}}[\rho_0] \tag{18}$$

Where $\mathrm{T}[\rho_0]$ is the kinetic energy, $\mathrm{V_{ne}}[\rho_0]$ is the coulombic interactions between electrons and nuclei and $\mathrm{V_{ee}}[\rho_0]$ is the electron-electron repulsive energy.(Zobel and González, 2019)

To describe the interactions between the electrons and nuclei in the non-interacting system, an external potential is introduced to the system. Therefore, the total energy takes the following form:

$$\mathrm{E}[\rho_0] = \mathrm{T_s}[\rho_0] + \mathrm{V_{ext}}[\rho_0] + \mathrm{J}[\rho_0] + \mathrm{E_{xc}}[\rho_0] \tag{19}$$

Where $\mathrm{J}[\rho_0]$ is the electron-electron repulsion energy, $\mathrm{V_{ne}}[\rho_0]$ is the coulombic interactions between electrons and nuclei, $\mathrm{T_s}[\rho_0]$ is the exact kinetic energy functional and $\mathrm{E_{xc}}[\rho_0]$ is the

exchange-correlation functional.(Neese, 2009) It is possible to obtain the energy of the system by applying the second Hohenberg-Kohn theorem to the Eq. 19 and employing an iterative SCF-like procedure:

$$\left[\frac{-\hbar^2}{2m}\nabla^2 + v_{eff}(r)\right]\phi_i(r) = \varepsilon_i\phi_i(r) \tag{20}$$

With the effective potential $v_{eff}(r,t) = v_{xc}(r,t,\psi_0) + v_{ne}(r,t) + J(r,t)$.(Jensen, 2017; Talotta, 2018) While the second $v_{ext}(r,t)$ and third term $J(r,t)$ are known, the exchange-correlation potential term $v_{xc}(r,t,\psi)$ is unknown. Therefore, the main issue of DFT is finding the best approach to account for the exchange-correlation functional of the system. Numerous functionals that include the exchange-correlation energy $E_{xc}[\rho]$ have been implemented on DFT. The most elemental approach to account for the exchange-correlation energy is the local density approximation (LDA) functionals. Here the energy is calculated from the electron density of a uniform electron gas. For open-shell systems the local spin density approximation (LSDA) is generated as a consequence of including the spin into the LDA approximation.(Jensen, 2017)

When the gradient of the density ($\nabla\rho$) is taken into account, a better approximation to the $E_{xc}[\rho]$ is obtained since the real density of the systems is not uniform. This approach is called Generalized Gradient Approximation (GGA). In addition to the gradient of the density ($\nabla\rho$), higher order derivatives of the density can be included on the functionals. Such functionals are called *meta*-GGA functionals when the laplacian of the density ($\nabla^2\rho$) is included within the expansion. Another way to adapt the exchange correlation energy on a functional is the hybrid GGA functionals, which combines the local density with higher order derivatives of the electron density plus a contribution of the HF exchange-correlation energy. The most well-known hybrids are B3LYP(Becke, 1993) and PBE0(Adamo and Barone, 1999). However, B3LYP fails when

charge-transfer excitations are involved due to the wrong behavior of the exchange potentials at long-range.(Yanai et al., 2004) Nevertheless, by incorporating a parameter that balances the HF exchange contribution according to the distance, the Range-separated functionals describe large-range interactions such as CAM-B3LYP(Yanai et al., 2004) and $\omega$B97X(Chai and Head-Gordon, 2008).(Jensen, 2017)

**2.2.4 Time-dependent density functional theory (TD-DFT)** Time-dependent density functional theory (TD-DFT) allows the elucidation of excited-state decay processes. The formalism of this theory is based on the Runge-Gross theorem. This theorem states that a one-to-one correspondence exists between the time-dependent electron density $\rho$(r,t) and the external time-dependent potential $\mathrm{V_{ext}}$(r,t) for a system evolving from an initial state $\Psi_0$.(Casida and Huix-Rotllant, 2012; Talotta, 2018) The Kohn-Sham equation Eq.(20) in terms of the time-dependent Schrödinger equation can be used to calculate the time-dependent electron density $\rho$(r,t):

$$\mathrm{i}\frac{\partial}{\partial \mathrm{t}}\phi_{\mathrm{i}}(\mathrm{r},\mathrm{t}) = \left[-\frac{\nabla^2}{2} + \mathrm{v_{eff}}(\mathrm{r},\mathrm{t})\right]\phi_{\mathrm{i}}(\mathrm{r},\mathrm{t}) \tag{21}$$

The solution of the Eq.(21) is not an easy task since it is represented by an eigenvalue equation with non-hermitian character and the SCF approach is not valid.(Rocca et al., 2012) Nonetheless, the equation can be written as a pseudo-hermitian eigenvalue equation:(Stratmann et al., 1998)

$$\begin{bmatrix} \mathrm{A} & \mathrm{B} \\ \mathrm{B}^* & \mathrm{A}^* \end{bmatrix} \begin{bmatrix} \mathrm{X} \\ \mathrm{Y} \end{bmatrix} = \omega \begin{bmatrix} 1 & 0 \\ 0 & -1 \end{bmatrix} \begin{bmatrix} \mathrm{X} \\ \mathrm{Y} \end{bmatrix} \tag{22}$$

with $\omega$ being the vertical excitation energies, X and Y the particle-hole and hole-particle excitations, while the matrices A and B depend on the chosen functional. The most used approach to simplify the solution of the Eq.(22) is the Tamm-Dancoff approximation (TDA),(Hirata and

Head-Gordon, 1999) where the hole-particle excitations are discarded as a consequence of fixing the B matrix to zero.(Franz, 2021) Thus, the eigenvalue equation is defined as

$$\mathrm{AX} = \Xi \mathrm{X} \tag{23}$$

Additionally, in some cases the TDA results are better or very close to the full linear response TD-DFT results(Casanova-Paez and Goerigk, 2020; Isborn et al., 2011).

## 2.3 Absorption and decay of electronically excited states of organic chromophores

**2.3.1 Overview** Absorption of UV-Vis radiation ($\mathrm{S}_0 \rightarrow \mathrm{S}_\mathrm{n}$) is the process that initiate the photophysical relaxation processes in organic chromophores. Despite the short lifetimes of the electronic excited states, two types of intramolecular decay processes exist: radiative and non-radiative. The predominant relaxation pathway depends on how probable is that a certain transition between two electronic states occurs. These transition probabilities are calculated through the rate constant (k) parameter. Additionally, these transition probabilities depend on other parameters such as the structure and the energy of the system. The main purpose of this project is to define two computational protocols to elucidate the photophysical processes of methylpheophorbide a. Therefore this section defines the theoretical framework for the main important concepts of photophysical processes and the calculation of their rate constants.

**2.3.2 Light absorption** The absorption of light by a molecule (PS + *hv* $\rightarrow$*PS) implies the conversion of a photon (*hv*) into the electronic excitation energy (*) of a molecule(Turro et al., 2009) and occurs on attosecond to picosecond timescales ($10^{-18} - 10^{-12}$).(Gutzler et al., 2021). This process only takes place when the incident photon matches the difference in energy between states of a molecule (energy gap, $\Delta$E). However, if the energy of the incident photon is higher than

the energy gap, the excess energy is transformed into vibrational and rotational energy.

The UV-Vis absorption spectrum of organic chromophores or dyes involves vibrational transitions of different electronic excited states with different probabilities. In this project, the spin-free Born-Oppenheimer framework will be used to investigate the vibronic absorption and emission of light.

**2.3.3 The Franck-Condon (FC) principle** The Franck-Condon principle takes into account the Born-Oppenheimer approximation as was introduced in section 2.2.1, to explain the probability of a radiative or non-radiative transition and the broadening of the emission and absorption spectra. Franck-Condon stated that the most probable transition occurs between the electronic states with similar nuclear configuration and similar vibrational states. Therefore, the most intense absorption is obtained for the transitions between two states at their respective minima (0-0 transition).

**2.3.4 Vibronic structure and Gouterman's model** The correct simulation of the absorption or emission spectrum involves the inclusion of the vibronic structure, i.e., the vibronic (electronic/vibrational) excitations and purely electronic excitations. Vibronic structure mainly depends on the transition dipolar moments (TDM) between the initial and final states and their contribution from the displacements along the normal modes. This contribution can be seen as a mixing of the initial and final excited states wave functions which produce a combination of their transition dipole moments due to an electron-nuclear perturbation.(Dierksen and Grimme, 2004) There are two types of transitions: the dipole-allowed transitions and the dipole-forbidden transitions. The dipole-allowed transitions are either strongly or weakly-dipole allowed transitions. When strongly dipole-allowed transitions are involved on the vibronic spectrum calculation, the FC approximation is sufficient. However, to correctly simulate the vibronic spectrum of a system that displays weakly-dipole allowed transitions or forbidden transitions, the computation of the vibronic cou-

pling (Herzberg-Teller effects) is recommended.

Low-energy electronic transitions of chlorin derivatives are usually described by the Gouterman model.(Gouterman, 1959, 1961; Gouterman et al., 1963) This model derives from the decrease of the $\mathrm{D_{16h}}$ symmetry to the $\mathrm{D_{4h}}$ symmetry originated from the addition of four pyrrole rings to the cyclic polyene $\mathrm{C_{16}H_{16}}^{2-}$. The $\mathrm{D_{4h}}$ point group comprises two non-degenerate HOMOs ($\mathrm{a_{1u}}$ and $\mathrm{a_{2u}}$) and two degenerate LUMOs ($\mathrm{eg_x}$ and $\mathrm{eg_y}$) with the magnetic quantum numbers $\mathrm{M_L}$ = $\pm$ 4 and $\mathrm{M_L}$ = $\pm$5, respectively.

Transitions among those four molecular orbitals HOMO, HOMO-1, LUMO, LUMO+1 generate the Q band and B band or Soret band. These types of bands are y or x-polarized. Thus, in ascending order of energy, the bands predicted for chlorins are $\mathrm{Q_y}$, $\mathrm{Q_x}$, $\mathrm{B_x}$ and $\mathrm{B_y}$. This model also considers the vibronic structure of chlorin-related compounds.(Gouterman, 1961) The Q transitions are crucial for describing the exciton transport of chlorophyll-like molecules.(Reimers et al., 2013, 2022; Sirohiwal et al., 2020; Song et al., 2019; Yin et al., 2007)

**2.3.5 Radiative decay processes** In radiative decay processes the excess of excitation energy is released as a photon. These relaxation processes may encompass a change of the total electronic spin. Thus, the radiative processes can be divided into spin-allowed and spin-forbidden processes. The spin-allowed process involves transitions between states of the same multiplicity and a subsequent release of a photon: $\mathrm{S_1 \rightarrow S_0 + hv}$, called "fluorescence" and display a rate constant $\mathrm{k_F}$. The spin-forbidden process involves transitions between states of different multiplicity and a subsequent release of a photon. $\mathrm{T_1 \rightarrow S_0 + hv}$, called phosphorescence and display a rate constant $\mathrm{k_P}$ which is generally slower than the $\mathrm{k_F}$ due to the forbidden character of the transition.

**2.3.6 Radiationless decay processes** Radiationless processes are essentially non-adiabatic processes due to the breakdown of the Born-Oppenheimer approximation. Thus, mixing of different

electronic excited states is necessary to characterize such transitions. These processes can be classified as spin-allowed or spin-forbidden. The spin-allowed process involves transitions between states of the same multiplicity: $\mathrm{S_1 \rightarrow S_0 + heat}$ and $\mathrm{S_n \rightarrow S_1 + heat}$ transitions encompasses the "internal conversion (IC)" with a rate constant $\mathrm{k_{IC}}$. On the other hand, the radiationless spin-forbidden process is called "intersystem crossing" and involves transitions between states of different multiplicity $\mathrm{S_1 \rightarrow T_n + heat}$, with a rate constant $\mathrm{k_{ISC}}$ or transitions such as $\mathrm{T_n \rightarrow S_1 + heat}$ which describes the "reverse intersystem crossing" with a rate constant $\mathrm{k_{RISC}}$.

#### 2.3.6.1 Intersystem crossing

Intersystem crossing process is induced by Spin-orbit coupling (SOC). SOC is a relativistic effect that cause an inversion of the spin by mixing states with different multiplicities.

Within a relativistic framework, the electronic Hamiltonian ($\hat{\mathrm{H}}_{\mathrm{el}}$) is given by the addition of the spin-orbit Hamiltonian ($\hat{\mathrm{H}}_{\mathrm{SO}}$) and the electrostatic Hamiltonian ($\hat{\mathrm{H}}_{\mathrm{es}}$):

$$\hat{\mathrm{H}}_{\mathrm{el}} = \hat{\mathrm{H}}_{\mathrm{SOC}} + \hat{\mathrm{H}}_{\mathrm{es}} \tag{24}$$

where $\hat{\mathrm{H}}_{\mathrm{es}}$ includes the "spin-free" states as diagonal elements; $\hat{\mathrm{H}}_{\mathrm{SOC}}$ is the spin-orbit operator coupling the electronic spin and orbital motion and mixing singlet-triplet states. This operator is generally incorporated as a perturbative correction in the non-relativistic framework.(Marian, 2021; Penfold et al., 2018)

The Breit-Pauli SOC Hamiltonian is defined as:

$$\hat{\mathrm{H}}_{\mathrm{SO}}^{\mathrm{BP}} = \frac{1}{2\mathrm{m_e^2 c^2}} \sum_{\mathrm{i}} \left[ \underbrace{\sum_{\mathrm{a}} \frac{\mathrm{Z_a}}{\mathrm{r_{ia}^3}} (\hat{\mathrm{r}}_{\mathrm{ia}} \times \hat{\mathrm{p}}_{\mathrm{i}}) \cdot \hat{\mathrm{s}}_{\mathrm{i}}}_{\text{one-electron}} - \underbrace{\sum_{\mathrm{j} \neq \mathrm{i}} \frac{1}{\mathrm{r_{ij}^3}} (\hat{\mathrm{r}}_{\mathrm{ij}} \times \hat{\mathrm{p}}_{\mathrm{i}}) \cdot (\hat{\mathrm{s}}_{\mathrm{i}} + 2\hat{\mathrm{s}}_{\mathrm{j}})}_{\text{two-electron}} \right] \tag{25}$$

where $\mathrm{m_e}$ is the electron mass, *c* is the speed of light. $\hat{\mathrm{r}}_{\mathrm{ia}}$ is the relative position of the electron with respect to a nucleus *a* with atomic number $\mathrm{Z_a}$, $\hat{\mathrm{p}}_{\mathrm{i}}$ represents the linear momentum of the electron *i* and spin $\hat{\mathrm{s}}_{\mathrm{i}}$. Therefore, the one-electron term denotes the spin-same-orbit interaction. On the other hand, the two-electron term represents the interaction between the electrons *i* and *j*. Due to the complexity associated with the manipulation of this operator, the most common approach is to define an effective one-electron operator in which the two-electron terms are included in the one-electron terms in an effective-potential manner:

$$\hat{\mathrm{H}}_{\mathrm{SO}}^{\mathrm{eff}} = \frac{1}{2\mathrm{m_e^2 c^2}} \sum_{\mathrm{a}} \sum_{\mathrm{i}} \frac{\mathrm{Z_a^{eff}}}{\mathrm{r_{ai}^3}} \hat{\mathrm{l}}_{\mathrm{i}} \cdot \hat{\mathrm{s}}_{\mathrm{i}} \tag{26}$$

with the angular momentum $\hat{\mathrm{l}}_{\mathrm{i}}$ and $\hat{\mathrm{s}}_{\mathrm{i}}$ is the spin operator of the electron *i*. The two-electron terms are taken into account by an effective nuclear charge $\mathrm{Z_a^{eff}}$ which represents the screening of the one-electron term induced by the two-electron terms.(Marian, 2021; Penfold et al., 2018)

**2.3.7 The Fermi's golden rule** Fermi's golden rule is an approach to calculate the transition probability between a initial i state and a final j state of a radiative or non-radiative process. It is based on the first-order perturbation theory in which an external perturbation leads to the transition between states. This theory is not valid when the density of final states at the density of the initial state is high, while the Fermi's golden rule is unsuitable to calculate transitions that involve a conical intersection.(do Casal et al., 2023; Marian, 2021) The Fermi's golden rule for an absorption or emission process can be written as

$$\mathrm{k_{ij}} = \frac{2\pi}{\hbar} \left| \langle \Psi_{\mathrm{i}} | \, \hat{\mathrm{H}} \, | \Psi_{\mathrm{j}} \rangle \right|^2 \delta(\mathrm{E_i - E_j}) \tag{27}$$

Where Eq.(27) includes a dirac delta $\delta$ which, in this case, transforms the energy domain to

the time domain and the transition rate constant and spectrum are calculated from an autocorrelation function.(de Souza et al., 2018, 2019).

**2.3.8 Computation of radiative and non-radiative rate constants** The path integral formalism (de Souza et al., 2018, de Souza et al., 2019) that connects the vibrational modes of the initial and final states was employed to calculate the excited-state decay processes.

The Fermi's golden rule for an emission process between an initial $\Psi_{\mathrm{i}}$ and a final $\Psi_{\mathrm{f}}$ state is given as

$$\mathrm{k}(\omega)_{\mathrm{ij}} = \frac{4\omega^3\eta^2}{3\hbar \mathrm{c}^3}\left|\langle\Psi_{\mathrm{i}}|\,\hat{\mu}\,|\Psi_{\mathrm{j}}\rangle\right|^2 \delta(\mathrm{E_i}-\mathrm{E_j}\pm\hbar\omega) \tag{28}$$

Where $\eta$ is the refractive index of the solvent, $\Psi_{\mathrm{ij}}$ is the wave function of the initial i or final j state; $\hbar\omega$ represent the absorption or the emission of a photon and $\hat{\mu}$ is the dipole operator for the fluorescence and phosphorescence rate constant.

The ISC rate constant can also be calculated by the Fermi's golden rule within the path integral formalism:

$$\mathrm{k}(\omega)_{\mathrm{ij}} = \frac{2\pi}{\mathrm{h}}\left|\langle\Psi_{\mathrm{i}}|\,\hat{\mathrm{H}}_{\mathrm{SOC}}\,|\Psi_{\mathrm{j}}\rangle\right|^2 \delta(\mathrm{E_i}-\mathrm{E_j}) \tag{29}$$

Here, $\hat{\mathrm{H}}_{\mathrm{SOC}}$ denotes the SOC operator, $|\Psi_{\mathrm{ij}}\rangle$ is the wave function of the initial i or final f state. The rate in Eq.(29) describes the direct spin-orbit coupling interaction ($\mathrm{k}_{\mathrm{ISC}}^{\mathrm{FC}}$).

When the vibronic contribution is included in the radiative or nonradiative rate calculation, the first order TDM is expanded into a Taylor series in a set of vibrational coordinates (Q) at the equilibrium geometry ($\mathrm{Q}_0$). Therefore, the expansion is defined as

$$\langle \Psi_i | \hat{O} | \Psi_j \rangle = \underbrace{\langle \Psi_i^{el} | \hat{O} | \Psi_j^{el} \rangle |_{q_{0=0}} \langle \Psi_i^{vib} | \Psi_j^{vib'} \rangle}_{FC} + \underbrace{\sum_k (\frac{\partial}{\partial q_k} \langle \Psi_i^{el} | \hat{O} | \Psi_j^{el} \rangle) \langle \Psi_i^{vib} | q_k | \Psi_j^{vib'} \rangle}_{HT} \quad (30)$$

Where $|\Psi_{ij}^{el}\rangle$ and $|\Psi_{ij}^{vib}\rangle$ are the electronic and vibrational wave functions between the initial i and final states j, $q_k$ is the vibrational coordinate of the k vibrational mode, $\hat{O}$ is the transition dipole operator $\mu$ for the fluorescence and phosphorescence or the SOC operator $\hat{H}_{SOC}$ for the ISC rate constant calculation, respectively. This approximation corresponds to the contribution of vibronic SOC to the ISC rate constant ($k_{ISC}^{FCHT}$). The effect of the vibronic coupling on the photophysical properties was computed using the Duschinsky matrix and Herzberg-Teller effects. (Baiardi et al., 2013)

## 3 State of art

In the existing literature, there are few computational studies about the photophysical processes of tetrapyrrolic systems. Common computational methods used to study the photophysics of these systems include the combination of density functional theory/multireference configuration interaction (DFT/MRCI) and the combination of density functional theory and time-dependent density functional theory (DFT/TD-DFT). The photophysical properties at the ground state geometry of chlorin derivatives, such as vertical excitation energy (VEE) and UV-Vis spectra, have previously been investigated within the framework of density functional theory (DFT) and time-dependent density functional theory (TD-DFT).(Parusel and Grimme, 2000, 2001; Shrestha et al., 2016; Zhang and Stillman, 2018; Zhang et al., 2017) A quantum chemical investigation of the vibronic structure of the absorption spectrum of a porphyrin derivative has recently been performed by Sirohiwal and coworkers applying the DLPNO-STEOM-CCSD and DFT/TD-DFT methods.(Sirohiwal et al., 2020) In a study by Reimers et al. the vibronic structure of the ab-

sorption spectra of porphyrin derivatives has been investigated employing the CAM-B3LYP functional.(Reimers et al., 2013, 2022) In addition to the vibronic structure of the absorption spectrum of porphyrins, the ultrafast decay within the Q-bands of a chlorophyll-a derivative has been investigated.(Reiter et al., 2022) Other investigations have been focused on the study of photophysical processes. Perun and coworkers calculated the TD-DFT and (DFT/MRCI) vertical excitation energies at the ground state geometry and the adiabatic excitation energies of the lowest excited states of free-base porphyrin. The latter method was also employed to compute the SOCMEs and the ISC rate constant.(Perun et al., 2008) Recently, Bhandari and coworkers used DFT/TD-DFT protocol to calculate the ISC rate constant ($\mathrm{k_{ISC}}$), the absorption spectrum and the fluorescence rate constant ($\mathrm{k_F}$) of porphine, bacteriochlorin and chlorin systems.(Bhandari et al., 2021)

Experimentally the photophysical properties of MPh have been investigated by Wang and coworkers,(Wang et al., 2014) who determined the singlet oxygen quantum yield ($\Phi_\Delta$ = 0.62) and the intersystem crossing ($\mathrm{k_{ISC}}$ = 0.79 x $10^8$ $\mathrm{s^{-1}}$) and fluorescence ($\mathrm{k_F}$ = 0.32 x $10^8$ $\mathrm{s^{-1}}$) rate constants.

## 4 Methodology

To systematically determine the geometry of the energetically lowest conformer of MPh, we used the CREST software(Pracht et al., 2020) with the extended semi-empirical tight-binding method GFN2-xTB to explore the conformational space.(Bannwarth et al., 2019) The lowest energy conformer was selected and used as the starting structure for the geometries of the electronic ground and excited states, applying the CAM-B3LYP(Yanai et al., 2004) functional along with the def2-SVP(Weigend and Ahlrichs, 2005, Weigend, 2006) basis set as implemented in the ORCA 5.0 package.(Neese, 2022) The RIJCOSX approximation was used to accelerate the calculations.(Neese et al., 2009,Izsák and Neese, 2011) Subsequently, two protocols were defined. The first protocol involves the geometry optimization of MPh in the ground state ($\mathrm{S_0}$); first sin-

glet ($S_1$), second singlet ($S_2$), second triplet ($T_2$), third triplet ($T_3$) and fourth triplet ($T_4$) under full TD-DFT,(Runge and Gross, 1984, Ekström et al., 2010) due to a triplet instability during the optimization the low-lying first triplet ($T_1$) was optimized using Unrestricted Kohn-Sham (UKS) formalism. The oscillator strengths, 0-0 energy, vertical (VEE) and adiabatic ($\Delta E_{SS}$, $\Delta E_{ST}$) excitation energies were determined from single-point calculations performed at the ground and excited states minima under full TD-DFT. The absorption and emission spectra, as well as the fluorescence, intersystem crossing and phosphorescence rate constants were calculated using the path integral approach implemented in the ESD module of ORCA 5.0. were also calculated employing full TD-DFT.

The second protocol involves the geometry optimization of MPh in the ground state ($S_0$); first singlet ($S_1$), second singlet ($S_2$) and second triplet ($T_2$) under full TD-DFT, (Runge and Gross, 1984, Ekström et al., 2010) the low-lying first triplet ($T_1$), third triplet ($T_3$) and fourth triplet ($T_4$) states were optimized using the Tamm-Dancoff approximation (TDA). The oscillator strengths, 0-0 energy, vertical (VEE) and adiabatic ($\Delta E_{SS}$, $\Delta E_{ST}$) excitation energies were determined from single-point calculations performed at the ground and excited states minima under TDA. (Hirata and Head-Gordon, 1999). Additionally, TDA was employed to calculate the radiative ($k_F$, $k_P$) and non-radiative ($k_{ISC}$) rate constants.

Both protocols were used to calculate the absorption and emission spectra; the fluorescence, intersystem crossing, and phosphorescence rate constants using the path integral approach implemented in the ESD module of ORCA 5.0. (Baiardi et al., 2013; de Souza et al., 2018, 2019) ISC rates were also calculated employing this methodology. The spin-orbit coupling (SOC) matrix elements Eq.(29) were estimated by using the quasi-degenerate perturbation theory (QDPT) (Suzuki and Okamoto, 1984) to calculate the singlets-triplets mixing obtained from the TD-DFT geometry optimizations. The SOC integrals were calculated using the exact coulomb terms and the mean-field

approximation for the exchange terms (AMFI spin-orbit coupling treatment), (Neese, 2005) taking into account the solvent effects. The effect of the level of theory on absorption, fluorescence and ISC properties was estimated using single points calculations at the CAM-B3LYP/def2-SVP geometries in combination with the functionals CAM-B3LYP,(Yanai et al., 2004) $\omega$B97X,(Chai and Head-Gordon, 2008) PBE0,(Adamo and Barone, 1999) along with the def2-SVP,(Weigend, 2006; Weigend and Ahlrichs, 2005) def2-TZVP(Weigend, 2006; Weigend and Ahlrichs, 2005) basis sets and full TD-DFT or Tamm-Dancoff approximation (TDA) for the first and second protocol, respectively.(Hirata and Head-Gordon, 1999) Additionally, the effect of the gaussian line shape and the number of roots for the ISC rate constant calculation were investigated. While the choice of the first 5 singlet and spin-adapted triplet excited states for the calculation of the $\mathrm{k_{ISC}}$ seems to be sufficient, 30 singlet and spin-adapted triplets excited states were used for phosphorescence spectrum and rate constant computation. A gaussian line shape was set, with an intrinsic linewidth (INLINEW keyword of the ESD module) of 10 $\mathrm{cm^{-1}}$ for ISC rate constant and for phosphorescence spectrum; and 150 $\mathrm{cm^{-1}}$ for the fluorescence spectrum and for the Q band vibronic structure. The Q band vibronic structure and the rest of the photophysical properties of MPh were calculated using the excited-state dynamics (ESD) module of the ORCA package. Our calculations were computed using the adiabatic hessian (AH) approach for the x- and y- polarized components of the Q band. The temperature was set to 298.15 K to compare with the experimental spectrum (in dichloromethane).(Rodriguez Prada, 2018) The vibronic progression (sticks) at 298.15 K was calculated by specifying the INLINEW keyword to 0.1, spectral resolution (SPECRES keyword of the ESD module) to 0.1, and discarding the normal modes with frequencies below 350 $\mathrm{cm^{-1}}$. On the other hand, the vibronic progression (sticks) at 0 K was calculated by specifying the INLINEW keyword to 0.1, SPECRES keyword to 0.01, and discarding the lowest normal modes with frequencies below 350 $\mathrm{cm^{-1}}$. For fluorescence and phosphorescence, normal modes with frequen-

cies above 350 $\mathrm{cm}^{-1}$ were also taken into account. However, for ISC, only normal modes with frequencies above 100 $\mathrm{cm}^{-1}$ were chosen. All calculations were computed in toluene employing a conductor-like polarizable continuum model (C-PCM).(Barone and Cossi, 1998) The resulting equilibrium structures had no imaginary frequencies. The photophysics of MPh was investigated using the path-integral approach within the TD-DFT framework at the CAM-B3LYP/def2-SVP level of theory. In this framework, the fluorescence and phosphorescence rate constants are calculated by Eq.(28), the ISC rate constant is calculated using the Eq.(29), and the vibronic contribution to the radiative or non-radiative rate constants are calculated by applying the Eq.(30).

The effect of the vibronic coupling on the photophysical properties was computed using the Duschinsky matrix and Herzberg-Teller effects.

# 5 Results and discussion

## 5.1 Choice of computational methods

It is widely known that an adequate modeling of an experimental system depends on the technical aspects of the employed computational protocol such as computational cost and quality of results. Therefore, it is important to determine the most suitable computational protocol for any system beforehand. Since (TD)-DFT are quantum-chemical methods that provides good quality of results and acceptable computational cost for large systems(Castro Júnior and Rocha, 2022; Yoshinaga and Rocha, 2021), these methods were employed in the present work. In order to get insights into the photophysics of methylpheophorbide a (MPh), the developed computational protocol was compared to experimental properties such as absorption spectrum and photophysical rate constants. Additionally, the experimental absorption spectrum was used to select the optimal parameters of the computational protocol as it has been used in other works(Franz, 2021).

The choosing of a reasonable combination of a functional and a basis sets is one of the most critical parameters we have to consider during the development of a computational methodology. For this reason, combinations between the functionals CAM-B3LYP, $\omega$B97X and the basis sets def2-SVP and def2-TZVP, were tested in this work. In order to test the effect of the Tamm-Dancoff approximation on the calculated VEE, we calculated the VEE with and without TDA (Figure 26). The effect of the TDA is a blue-shift of up to 0.16 eV with respect to the calculated TD-DFT energies, resulting in deviations of the calculated VEE of up to 0.49 eV from the experimental band maxima. Similar blue shifts have been observed using this functional in a recent study of the absorption spectra of phtalocyanins.(Martynov et al., 2019) Due to the similar results with both functionals and considering that CAM-B3LYP displayed good performance on similar systems(Reimers et al., 2013; Sirohiwal et al., 2020), CAM-B3LYP was selected as (TD)-DFT functional to investigate the photophysics of MPh.

The effect of the basis set on the MPh calculated absorption spectrum was also investigated (Figure 27). The effect of the basis set under TDA or full TD-DFT on the absorption spectrum is approximately 0.04 eV. Since the effect of the basis set is small and the basis set def2-TZVP is computationally more expensive than the def2-SVP basis set, the latter was chosen as (TD)-DFT basis set for the upcoming photophysical properties calculations of MPh.

To verify that the vibronic spectrum of MPh calculated in toluene is comparable to the experimental UV-Vis spectrum in dichloromethane, we calculated the vertical excitation energies in dichloromethane and in toluene (Figure 28). Compared to the vertical excitation energies in dichloromethane, the red-shift of the calculated VEE with respect to the experimental spectrum of the lowest excited state $S_1$ in toluene (2.18 eV) is very similar to the one calculated in dichloromethane (2.20 eV). Moreover, the VEE of the second excited state $Q_x$ in toluene also appears to be red-shifted by 0.02 eV, which is very close to the calculated VEE in dichloromethane

(2.54 eV). Therefore, solvent effect differences are small and they do not change whether full TD-DFT or TDA is employed (Figure 29). This justifies the comparison of the experimental MPh absorption spectrum in dichloromethane with the computed spectra in toluene.

Comparisons between experimental band maximum energies and computed VEEs are incorrect since the contributions of vibrational levels are not considered(Bai et al., 2020; Berraud-Pache et al., 2019; Sirohiwal et al., 2020). Therefore, the effect of important parameters for the calculation of vibronic structure such as Gaussian bandwidth, number of points of the correlation function and the discarding of vibrational modes were also tested. It was observed that a large Gaussian bandwidth (250 $cm^{-1}$) and a short Gaussian bandwidth (50 $cm^{-1}$) were not in good agreement with experimental findings Figure 30. Hence, a Gaussian shape of (150 $cm^{-1}$) was chosen to shed light on absorption and fluorescence processes. On the other hand, a Gaussian bandwidth of (10 $cm^{-1}$) was chosen for the computation of ISC and phosphorescence processes due to the great sensitivity to the energy differences of the ISC rates, which is an explicit calculation on the former and an implicit calculation on the latter process.

Next, the influence of the number of points used for the Fourier transform step on the absorption spectrum was investigated. The results are shown in Figure 31. As can be seen, there is no effect of the number of points on the calculated absorption spectrum. Thus, we chose to use the Cooley-Tukey algorithm that ORCA uses by default to decide the number of points for the upcoming calculations. Nevertheless, this algorithm sometimes fails and the calculation does not converge. To ensure converges of the ISC rate calculation, we decided to fix 524288 points for the ISC Fourier transform step.

Due to the numerous degrees of freedom that chlorophyll derivatives have, problems related to the applicability of the harmonic approximation may arise(Cerezo et al., 2013). Then, discard-

ing vibrational modes in which torsional modes might be included will improve the applicability of the harmonic approximation and the shape of the spectrum. However, it is necessary to mantain a balance between discarded vibrational modes and quality of the calculated spectrum to avoid removing important vibrational contributions to the spectrum or rate constants. Following this consideration, we found that the shape of the spectrum considerably improved after discarding modes between 300-400 $cm^{-1}$ and we chose discarding modes below 350 $cm^{-1}$ for absorption, fluorescence and phosphorescence calculations. For the calculation of ISC rate constants, all normal modes with frequencies below 100 $cm^{-1}$ were discarded to avoid the elimination of important vibronic SOC contributions.

## 5.2 Photophysics investigation under the first protocol

**5.2.1 Ground state minimum and vertical excitation energies** The TD-DFT vertical excitation energies of MPh are listed in Table 1. At the ground state minimum, TD-CAM-B3LYP calculations show transitions between Gouterman's orbitals (Figure 2). The Gouterman orbitals are delocalized over the entire molecule with the exception of the $C_{17}$ methyl ester group.

The first singlet excited state $S_1$ vertical excitation energy amounts to 2.18 eV with an oscillator strength of f(L) = 0.292. The dominant contribution for this state corresponds to a $\pi_H \rightarrow \pi^*_L$ transition. The second singlet excited state $S_2$ is dominated (weight of 69%) by the $\pi_{H\text{-}1} \rightarrow \pi^*_L$ transition with an oscillator strength of f(L) = 0.075. Furthermore, the third singlet excited state $S_3$ state is dominated (weight of 67%) by the $\pi_H \rightarrow \pi^*_{L+1}$ transition with an oscillator strength of 1.439. The lowest $T_1$ and $T_4$ states have the $\pi_{H\text{-}1} \rightarrow \pi^*_L$ and $\pi_{H\text{-}1} \rightarrow \pi^*_{L+1}$ transitions as the dominant configurations. Additionally, $T_2$ and $T_3$ have the dominant configurations of $\pi_H \rightarrow \pi^*_L$ and $\pi_H \rightarrow \pi^*_{L+1}$ respectively. Above $S_2$ there are more $\pi \rightarrow \pi^*$ transitions, whose energies correspond to bands outside the Q-region of the absorption spectrum. Therefore, they won't be considered

for the present work.

As mentioned before, these dominant configurations can be explained using the Gouterman ' s model. According to this model, the dominant configurations of the $S_1$ and $S_2$ states are associated with the $Q_y$ and $Q_x$ bands respectively.

**Table 1.** *Vertical singlet and triplet excitation energies (eV) in toluene (calculated applying full TD-DFT), and the magnitudes of transition dipole moments (Debye) calculated at the CAM-B3LYP/def2-SVP ground state geometry (employing full TD-DFT).*

| **Electronic state** | **Electronic structure** | **TD-CAM-B3LYP[b]** | **Experiment** | **($\|\mu\|$, Debye)** |
|---|---|---|---|---|
| $S_1$ | (0.81) $\pi_H \rightarrow \pi^*_L$<br>(0.14)$\pi_{H-1} \rightarrow \pi^*_{L+1}$ | 2.18 (0.292) | 1.85[c] 1.86[de] | 5.94 |
| $S_2$ | (0.69) $\pi_{H-1} \rightarrow \pi^*_L$<br>(0.26)$\pi_H \rightarrow \pi^*_{L+1}$ | 2.52 (0.075) | 2.30[d] 2.31[ce] | 2.81 |
| $S_3$ | (0.67) $\pi_H \rightarrow \pi^*_{L+1}$<br>(0.25)$\pi_{H-1} \rightarrow \pi^*_L$ | 3.33 (1.439) | - | 10.67 |
| $T_1$ | (0.56) $\pi_{H-1} \rightarrow \pi^*_L$<br>(0.19)$\pi_H \rightarrow \pi^*_L$<br>(0.14)$\pi_H \rightarrow \pi^*_{L+1}$ | 0.81 | - | - |
| $T_2$ | (0.74) $\pi_H \rightarrow \pi^*_L$<br>(0.20)$\pi_{H-1} \rightarrow \pi^*_L$ | 1.52 | - | - |
| $T_3$ | (0.73) $\pi_H \rightarrow \pi^*_{L+1}$<br>(0.11)$\pi_{H-1} \rightarrow \pi^*_L$ | 2.06 | - | - |
| $T_4$ | (0.79) $\pi_{H-1} \rightarrow \pi^*_{L+1}$ | 2.44 | - | - |

Continued on next page

**Table 1 – continued from previous page**

| Electronic state | Electronic structure | TD-CAM-B3LYP[b] | Experiment | ($\|\mu\|$, Debye) |
|---|---|---|---|---|

[a]Dominant contributions at CAM-B3LYP/def2-SVP level of theory.

[b] Oscillator strength (length) on parenthesis.

[c]Ref.(Balashova et al., 2021) maximum of absorption band.

[d]Ref.(Rodriguez Prada, 2018) maximum of absorption band.

[e]Ref.(Briat et al., 1967) maximum of absorption band.

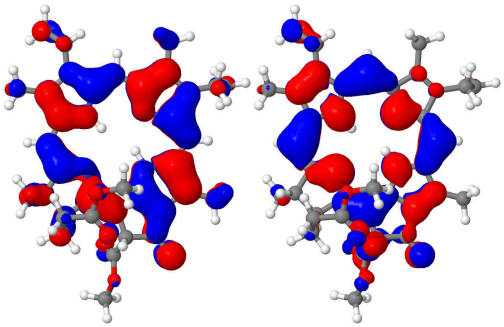

**(a)** ($\pi_H$) E = 0.00 eV **(b)** ($\pi_{H-1}$) E = -0.31 eV

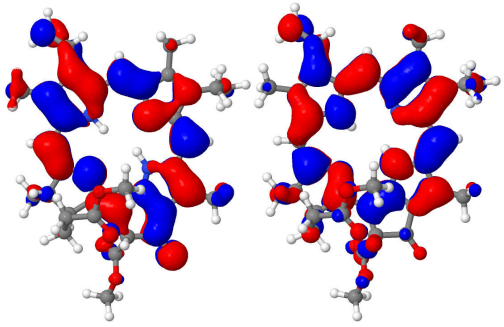

**(c)** ($\pi_L$) E = 4.31 eV **(d)** ($\pi_{L+1}$) E = 5.09 eV

**Figure 2.** Frontier molecular orbitals at the $S_0$ geometry of methylpheophorbide a (isovalue 0.01). The energies are listed relative to the energy of the HOMO.

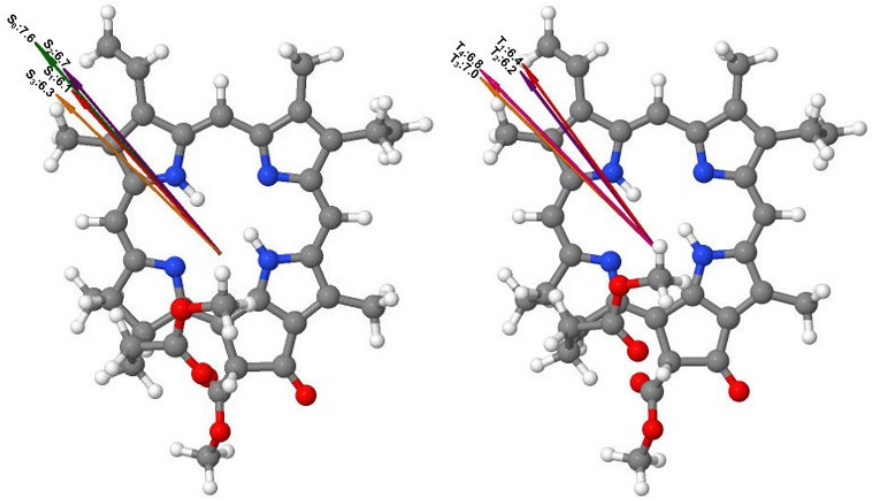

**Figure 3.** Negative dipole moments of the lowest singlet $S_0$-$S_3$ and triplet $T_1$-$T_4$ excited states in MPh, calculated at the CAM-B3LYP/def2-SVP ground state geometry under full TD-DFT. The magnitudes of the dipole moments are given in Debye.

To shed light into the influence of a polar solvent on the excitation energies of the excited states, we analyzed the dipole moments of the low-lying excited states (see Figure 3), the $S_2$, $T_3$ and $T_4$ states should show a small energetic destabilization in the presence of a polar solvent. On the other hand, $S_1$, $S_3$ and $T_1$-$T_2$ should be stronger destabilized relative to the ground state in polar solvents.

**5.2.2 Geometries of the excited state minima** The optimized structures of $S_0$-$S_2$ and $T_1$-$T_3$ are depicted in Figure 4. Due to the rigid structure, the geometric differences among the excited state geometries are small. The principal differences include the C–C methine bridges distances, the C–C distances of the first protonated pyrrole ring and the C–N distances of the deprotonated pyrrole rings, which are also characteristic for the porphyrin(Perun et al., 2008).

In the $S_1$ state, the elongation of the $C_2$–$C_3$, $C_6$–$C_7$, $C_6$–$N_{22}$, $C_9$–$C_{10}$, $C_{11}$–$C_{12}$ and $C_{15}$–$C_{16}$ distances amounts to 2 pm. While the $C_4$–$C_5$ distance is elongated 3 pm, the $C_5$–$C_6$ distance is

shortened by the same value. Moreover, the $C_{19}$–$C_{20}$–$C_1$ methine bridge exhibits an asymmetric stretching pattern. In the $S_2$ state, the $C_3$–$C_4$, $C_5$–$C_6$, $C_{19}$–$C_{20}$ and $C_{16}$–$N_{24}$ distances are shortened 2 pm; the $C_2$–$C_3$, $C_4$–$C_5$ and $C_{19}$–$N_{24}$ distances are elongated by 3 pm. The main difference of this state is the elongation of the $C_1$–$C_{20}$ distance which amounts to 4 pm. In the $S_3$ state, the most significant structural changes are elongations of the $C_9$–$C_{10}$, $C_{11}$–$C_{12}$, $C_2$–$C_3$, $C_4$–$C_5$. $C_6$–$N_{22}$, $C_{15}$–$C_{16}$, $C_{19}$–$C_{24}$, $C_{20}$–$C_1$ distances by 3, 3, 2, 2, 2, 2, 2, 2 pm and shortening of the $C_9$–$N_{22}$, $C_{10}$–$C_{11}$ and $C_{16}$–$N_{24}$ by 2 pm. In the $T_1$ state, the $C_4$–$C_5$ distance and the $C_5$–$C_6$ distance are extended by 7 pm and shortened by 6 pm, respectively. The $C_2$–$C_3$ and $C_6$–$N_{22}$ distances are elongated by 5 pm. In the $T_2$ state, the main difference between both structures is the elongation of the $C_4$–$C_5$, $C_6$–$C_7$, $C_8$–$C_9$, $C_{15}$–$C_{16}$, $C_{20}$–$C_1$ distances by 5, 3, 3, 3, 3 pm. The distances $C_5$–$C_6$, $C_{16}$–$N_{24}$, $C_{19}$–$N_{24}$, $C_{19}$–$C_{20}$ are shortened by 4, 3, 4, 3 pm, respectively. In the $T_3$ state, the principal variations are the elongation of the $C_4$–$C_5$, $C_5$–$C_6$, $C_8$–$C_9$ $C_9$–$C_{10}$, $C_{10}$–$C_{11}$, $C_{11}$–$C_{12}$, $C_{19}$–$C_{20}$ distances by 2, 2, 2, 3, 2, 3 and 2 pm.

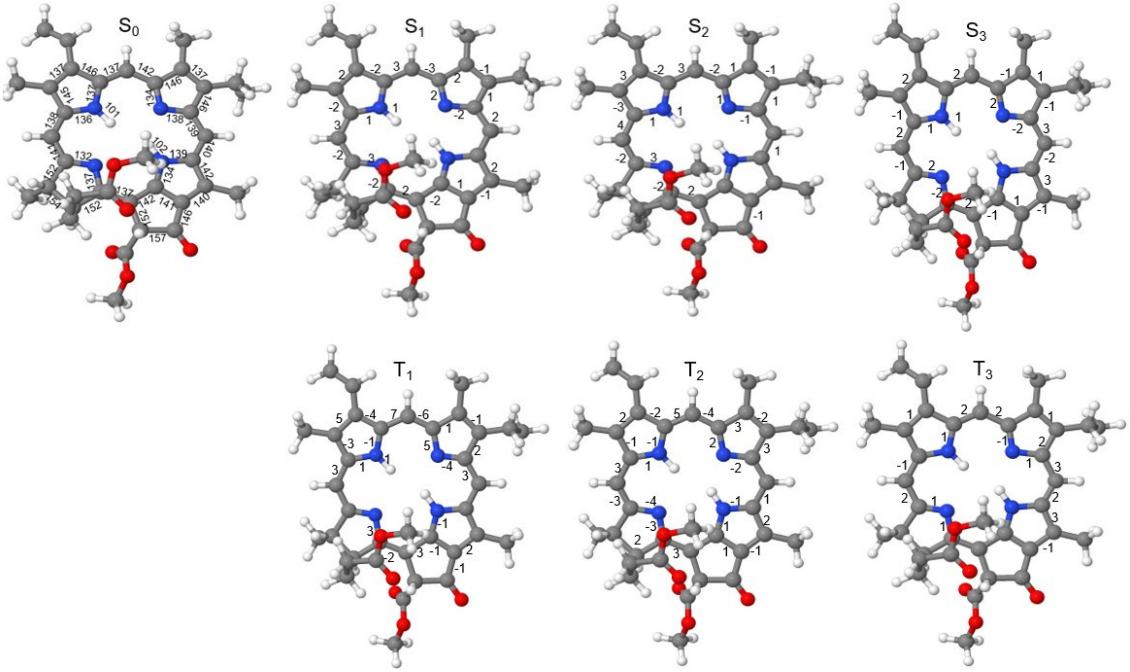


**Figure 4.** Selected bond lengths (in pm) of the ground and excited states of the ground state and differences relative to the ground state structure. Only non-zero values are given.

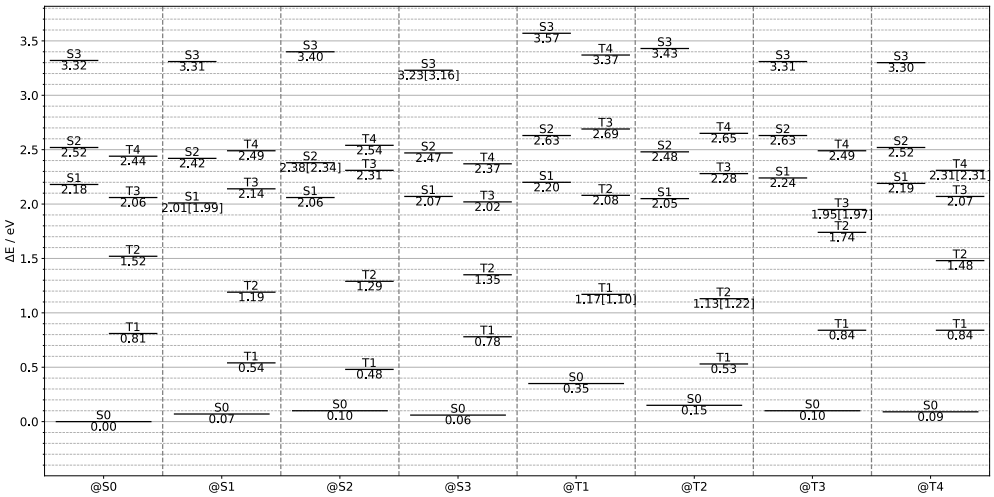


**Figure 5.** State energies (DFT, [eV]) calculated at the optimized geometries of the $S_0$, $S_1$, $S_2$, $S_3$, $T_1$, $T_2$, $T_3$, $T_4$ states of methylpheophorbide a. All energies are set relative to the ground state energy at $S_0$ geometry and computed under full TD-DFT.

The energies of the ground and excited states are depicted in Figure 5. The adiabatic exci-

tation energy is equal to 2.01 eV (1.99 eV considering zero-point vibrational energy) within the framework of full TD-DFT. From an energetic perspective, the structural relaxation effects on the energy of the $S_1$ state corresponds to a stabilization of 0.17 eV. On the other hand, relaxation effects shows a minor influence on the $S_2$ and $S_3$ excited states, with respective values of 0.10 and 0.09 eV.

TD-DFT optimization of the corresponding $T_1$ minimum turned out to be more difficult than expected. The TD-DFT optimization of the $T_1$ geometry led to a triplet instability. Therefore the $T_1$ minimum was calculated using Unrestricted Kohn-Sham (UKS) level of theory. The adiabatic energy of the $T_1$ state is 1.17 eV (1.10 eV including ZPVE), which are in the range of adiabatic energy values for a series of chlorins from 1.08-1.68 eV calculated at the B3LYP/6-31G(d) level of theory in gas phase(Palma et al., 2008). Structural relaxation has a major influence on the $T_2$ state (0.39 eV) and a less influence on the $T_3$ state (0.11 eV), $T_4$ state (0.13 eV). Since the $T_1$, $T_2$ and $T_3$ states exhibit lower energies than $S_1$ (2.18 eV), intersystem crossing is possible between the $S_1$ excited state and the $T_1$, $T_2$ and $T_3$ states.

**5.2.3 Q-band region of the absorption spectrum** The Q-band region of the calculated and the experimental absorption spectrum is shown in Figure 6. To rationalize the differences between the experimental and the calculated Q-band, we may consider the influence of several factors on the calculated spectrum such as the equilibrium geometry and the decoherence of the Q-band. In a previous study by Sirohiwal it has been found that the calculated excitation energies may change according to the level of theory applied for geometry optimization(Sirohiwal et al., 2020). Another parameter that may affect the calculated absorption band is the choice of the conformer. In our calculations we have used the lowest energy conformer as the initial geometry for the investigation of photophysical processes of MPh. Although we did not investigate the effect of the conformer geom-

etry on the Q-band vibronic structure, in a related study in our group on a similar system we found that the choice of the conformer affects the shape of the Q-band(**suarez_photophysical_2024**). Other factors related to structural flexibility that have an effect on the description of the Q-band are the torsional modes, which reduce the applicability of the harmonic approximation. We discarded vibrational modes below 350 $cm^{-1}$, which include the torsional modes of the ester and methyl groups.

The shape of the Q-band is also affected by a non-adiabatic mixing between the $Q_y$ and $Q_x$ bands. This non-adiabatic mixing is the main reason for the failure of Gouterman' s model to describe some spectroscopic properties such as the main polarization direction of the transition, which is represented by the subscripts(Reimers et al., 2022; Song et al., 2019). However, our calculations do not allow us to comprehend the nonadiabatic coupling of states, as we are using adiabatic dynamics. Since our results show that the overall calculated spectrum matches reasonably well with the experimental spectrum, we may assume that the contribution of the nonadiabatic coupling to the MPh absorption spectrum is not very important here.

To investigate the effect of the level of theory on the absorption properties of MPh, we used the CAM-B3LYP/def2-SVP optimized geometries and performed single point calculations with the density functionals CAM-B3LYP, $\omega$B97X, PBE0 and the basis sets def2-SVP, def2-TZVP (see Table 13). The calculated VEEs for $S_1$ are very similar with the three functionals, with differences of $\leq$ 0.05 eV. Larger differences between the three functionals are found for the $S_2$ state. The utilization of the smaller, less computationally demanding def2-SVP basis has a minimal impact on the VEEs, with blue shifts of less than 0.05 eV observed for the $S_1$ and $S_2$ transitions with the CAM-B3LYP functional.

Table 13 shows that $S_1$ state exhibits the largest oscillator strength at the ground state ge-

ometry. The calculated VEEs for $S_1$ are very similar with the three functionals, with differences $\leq$ 0.05 eV. Larger differences between the three functionals are found for the $S_2$ state. For the $S_1$ transition the CAM-B3LYP/def2-SVP VEE is about 0.3 eV higher than the experimental band maximum, while the $S_2$ transition shows a difference of approximately 0.2 eV. It should be noted that the band maximum and the vertical excitation energy do not coincide and the VEE is about 0.2 eV higher than the calculated band maximum. Using the smaller, and computationally less demanding def2-SVP basis has only a small effect on the VEEs (blue shifts of less than 0.05 eV for the $S_1$ and $S_2$ transitions with the CAM-B3LYP functional).

The vibronic spectra computed using only the Franck-Condon (FC) term in Eq.(30) and taking into account the Herzberg-Teller term (FCHT) are shown in Figure 6. The Franck-Condon approximation gives an adequate description of the spectrum. As expected from the oscillator strengths of the $S_1$ and $S_2$ transitions, the Herzberg-Teller contribution has little effect on the shape of the spectrum.

From an energetic point of view, the calculated vibronic progression associated with the $S_0 \rightarrow S_1$ absorption spectrum shows a band maximum at 1.86 eV and spans the whole Q-region. The band located at 2.21 eV is mostly related to the $S_0 \rightarrow S_2$ vibronic progression. Both bands correspond to 0-0 transitions, as can be seen in the vibronic spectrum at 0K (Figure 6). Based on the Gouterman model, the $Q_y$ band is described by HOMO$\rightarrow$LUMO and HOMO-1$\rightarrow$LUMO+1 excitations and the $Q_x$ band is associated with HOMO-1$\rightarrow$LUMO and HOMO$\rightarrow$LUMO+1 transitions, consistent with our calculations(Sirohiwal et al., 2020). Additionally, the assigment of the $Q_y$ band is also supported by the MCD spectrum of MPh(Reimers et al., 2013).

In order to check the consistency of our calculations with the experimental data, we compared the VEEs calculated at the ground state geometry with the calculated band maxima. The VEEs

are blue-shifted by 0.19 eV and 0.18 eV with respect to the calculated $S_1$ and $S_2$ band maxima (Figure 6), which is within the range found in a recent benchmark study by Bai and coworkers ($0.11 \pm 0.08$ eV)(Bai et al., 2020).

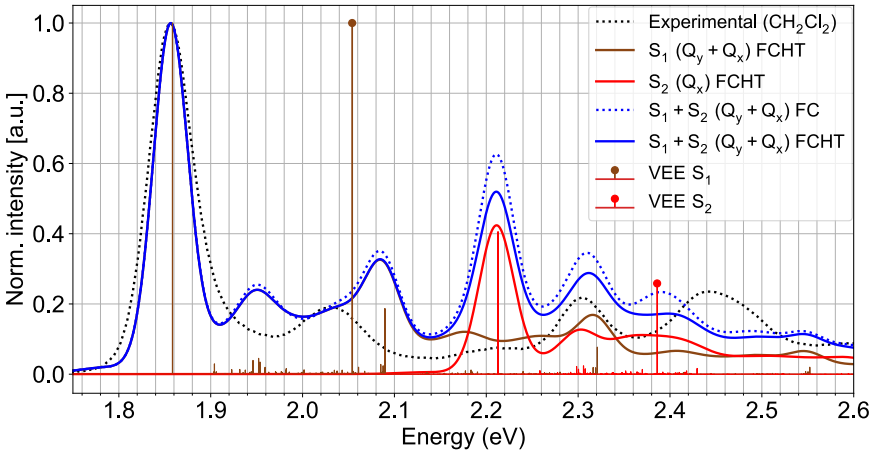


**Figure 6.** Computed vibronic structure of the Q region of the absorption spectrum employing the adiabatic Hessian model, and including Franck-Condon (FC) and Franck-Condon and Herzberg-Teller (FCHT) terms at 298.15 K. The Gaussian bandwidth was set to 150 $\mathrm{cm}^{-1}$ and vibrational modes below 100 $\mathrm{cm}^{-1}$ were discarded. The stick spectrum was calculated at 0 K. A stick spectrum calculated at 298.15 K is presented in Figure 33. The calculated spectra were displaced 0.13 eV to the left to align with the experimental band maximum.

#### 5.2.3.1 Vibronic structure calculated by VG and AHAS approximations

In contrast to the calculated absorption spectrum employing the Adiabatic Hessian (AH) approximation, the simulated absorption spectra under Vertical Gradient (VG) (Figure 7) and Adiabatic Hessian After After Step (AHAS) (Figure 8) did not significantly improved after discarding vibrational modes. Since the VG and AHAS approximations extrapolate the excited state hessian from the ground state, the calculated excited state vibrational modes do not describe the vibronic absorption structure. Therefore, the simulated spectra do not resemble the experimental bands.

On the other hand, the different band shapes of both approximations might be explained by taking into account the excited state hessian extrapolation methods. While the VG approximation

considers that the excited state geometry and vibrational modes can be extrapolated from the excited state hessian which is equal to the ground state hessian, the AHAS approximation considers that the excited state hessian can be extrapolated from the ground state geometry after an optimization step. Therefore, the excited state vibrational modes changes when the AHAS approximation is employed but they are equal to the ground state vibrational modes when the VG approximation is used.

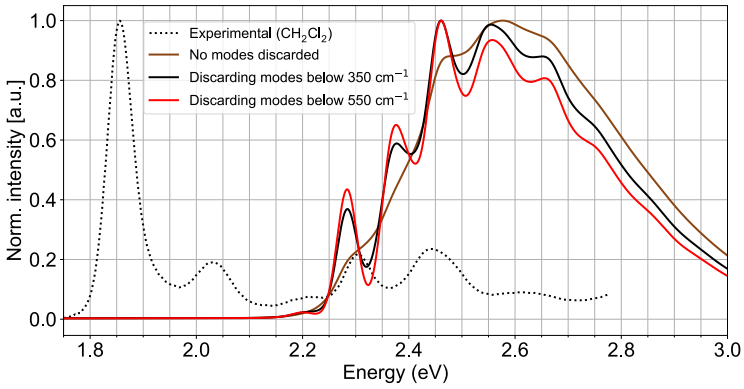


**Figure 7.** Computed vibronic structure of the Q region of the absorption spectrum employing the VG approximation and FCHT contribution at 298.15K. The Gaussian bandwidth was set to 150 $\mathrm{cm}^{-1}$.The vibrational modes below 350 $\mathrm{cm}^{-1}$ were discarded.

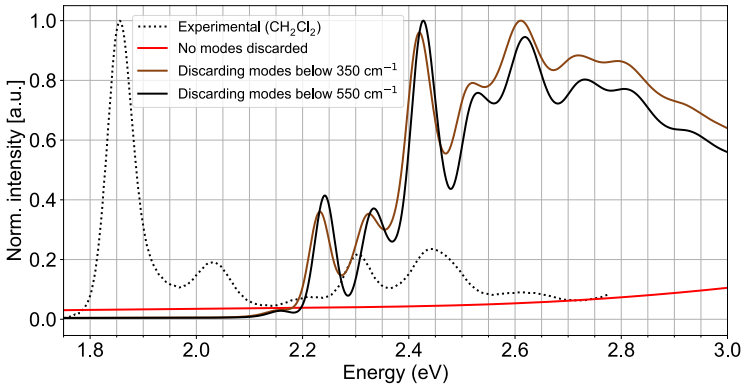


**Figure 8.** Computed vibronic structure of the Q region of the absorption spectrum employing the AHAS approximation and FCHT contribution at 298.15K. The Gaussian bandwidth was set to 150 $\mathrm{cm}^{-1}$.The vibrational modes below 350 $\mathrm{cm}^{-1}$ were discarded.

**5.2.4 Fluorescence and phosphorescence** The computed fluorescence spectra of MPh is presented in Figure 9. The influence of the FCHT contribution on the fluorescence spectra is an increment of emission intensity exhibited by the tails, similar to what is observed in the absorption spectrum. The calculated fluorescence band maximum $\lambda_{\mathrm{F}}$ of MPh is 1.99 eV and the fluorescence rate constant is 1.24 x $10^8$ $s^{-1}$ using the FC approximation (Table 2). Including HT effects in the calculations results in a fluorescence rate constant of 1.65 x $10^8$ $s^{-1}$ (Figure 10). The overestimation of the fluorescence rate may be a consequence of the overestimation of the $S_0$-$S_1$ energy difference in our calculations.

**Table 2.** *Adiabatic energy difference ($\Delta E_{S0\text{-}S1}$, eV), fluorescence rate constant ($k_F$, $s^{-1}$), fluorescence band maximum ($\lambda_F$, eV), transition dipole moment between the $S_1$ and $S_0$ states ($\mu^2$ [$S_1 \rightarrow S_0$], $au^2$) and oscillator strength $f_{osc}$, computed at the TD-DFT/CAM-B3LYP(C-PCM)/def2-SVP level of theory.*

| **Property** | **Value** | **Experiment ($s^{-1}$)** |
|---|---|---|
| $\Delta E_{S0-S1}$ | 2.01 | - |
| $k_F$ | 1.24 x $10^8$ | 0.32 x $10^8$ |
| $\lambda_F$ | 1.99 | 1.83 |
| $\mu^2$ ($S_1 \rightarrow S_0$) | 2.38 | - |
| $f_{osc}$ | 3.03 x $10^{-1}$ | - |

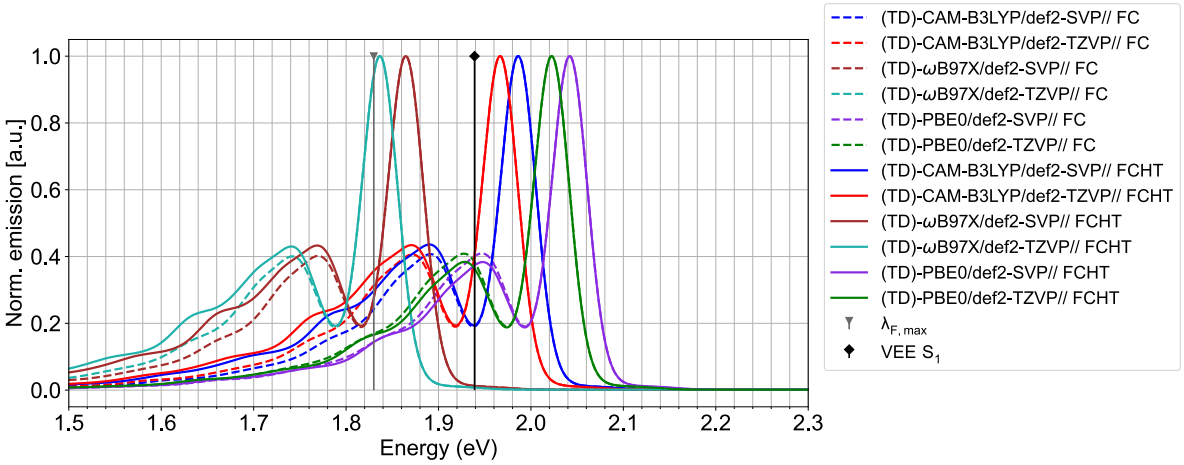


**Figure 9.** Predicted fluorescence spectra calculated with different functionals and basis sets using the FC and FCHT approximations. The CAM-B3LYP/def2-SVP optimized geometry was used in all calculations. The experimental band maximum is shown in gray.

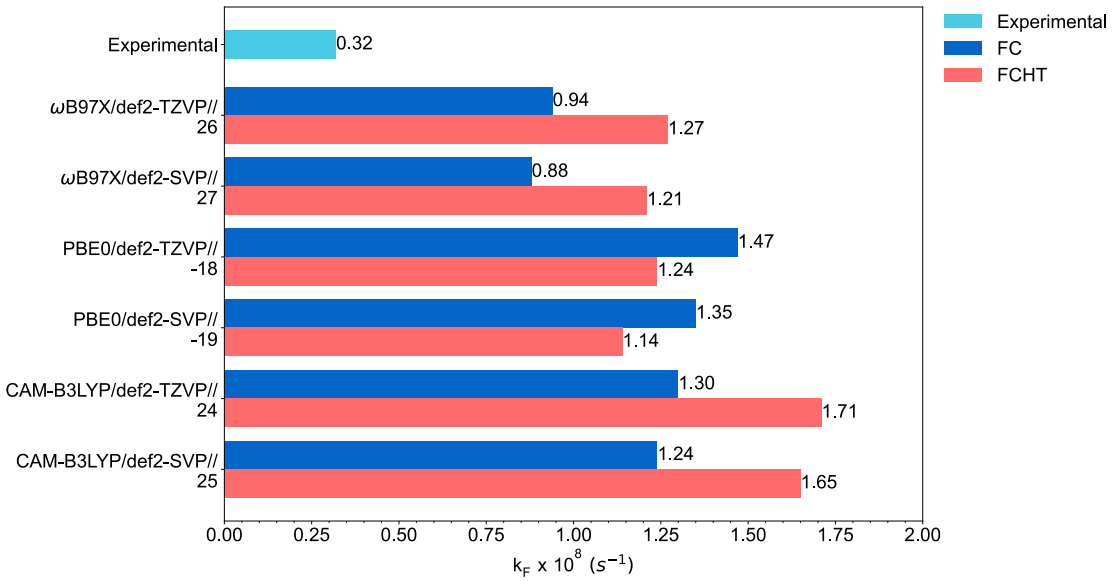


**Figure 10.** Fluorescence rate constants computed at different levels of theory employing the FC and FCHT approximations effects. The CAM-B3LYP/def2-SVP optimized geometry was used in all calculations. The values under the labels are the relative Herzberg-Teller contributions.

As for the absorption spectra, the effect of the level of the theory on the fluorescence spectra and the fluorescence rate constant has also been tested. The results are shown in Figure 9 and Figure 10 . Figure 10 shows a small effect of the density functional on the fluorescence rate. The effect of Herzberg-Teller effects is also relatively small. As for the absorption spectra, the effect of switching from the def2-SVP to the def2-TZVP basis set is a small red shift of the fluorescence band of up to 0.02 eV. There is, however, an effect of the functional on the simulated fluorescence spectrum. The computed fluorescence band maxima using the functional $\omega$B97X agrees very well with the experimental fluorescence band maximum, with a small deviation ($\leq$ 0.03 eV). In addition, the rest of the computed TD-DFT band maxima are in line with the experimental emission band maximum, with a deviation of $\approx$ 0.21 eV, which is within the expected range for the applied methodology. Moreover, the vertical emission energy shifts match relatively well with the experimental fluorescence band maximum (0.05 eV). Due to the similarity of the calculated values and for consistency, we chose the TD-DFT/CAM-B3LYP(C-PCM)/def2-SVP level of theory to calculate the fluorescence properties of our system considering only the FC approximation.

Experimentally it is found that MPh is essentially non-phosphorescent. However, in order to check the consistency of our calculations with these findings we computed the phosphorescence rate constant ($k_P$) (see Table 3). Since the path integral approach uses spin-adapted triplets for the computation of the triplet state, it can be assumed that the geometries of the $T_{1,+1}$, $T_{1,0}$, $T_{1,-1}$ triplet sublevels are degenerate and equally populated (high temperature average). Our results are in agreement with the experimental findings. A very slow phosphorescence process ($k_P$ = 7.26 x $10^{-1}$ $s^{-1}$) is expected due to the small transition dipole moments ($10^{-5}$-$10^{-4}$ a.u.)

**Table 3.** *Phosphorescence rate constant* $k_P(s^{-1})$*, transition dipole moments* $|\mu^2\ (S_0 \leftarrow T_{1,a})|$ *(a.u.) and radiative lifetimes* $\tau_P$ *(s) for the three spin sublevels of the* $T_1$ *state computed at the ground state minimum.*

| **Sublevel** | $\|\mu^2$ **(S₀← T₁,ₐ)**$\|$ | $\mathbf{k_P}$ **(298.15K)** | $\boldsymbol{\tau_P}$ |
|---|---|---|---|
| $T_{1,+1}$ | 2.88 x $10^{-4}$ | 4.88 x $10^{-1}$ | 2.05 x $10^{-2}$ |
| $T_{1,0}$ | 7.11 x $10^{-5}$ | 6.86 x $10^{-2}$ | 1.46 x $10^{1}$ |
| $T_{1,-1}$ | 1.02 x $10^{-4}$ | 1.62 x $10^{-2}$ | 6.17 x $10^{-1}$ |
| High temperature average | | 7.26 x $10^{-1}$ | 0.14 x $10^{1}$ |

### 5.2.5 Intersystem crossing channels

#### 5.2.5.1 Calculated ISC rate constant by the RI-SOMF(1X) SOC-operator

The calculated ISC rates by employing RI- SOMF(1X) SOC-treatment are shown in Table 4. The ISC rates are determined primarily by three main factors, namely (1) the difference in the adiabatic energy between the participating states, (2) the strength of the spin-orbit coupling (SOC) in a quantitative representation by the SOCMEs, and (3) the degree of overlap between the vibrational wave functions of the non-radiative channel. Another factor that influences the ISC rate constant is the change of the orbital type during the process. According to El-Sayed's rule, the SOCMEs between ($\pi \rightarrow \pi^*$) and ($\pi \rightarrow \pi^*$) states are smaller than those between states of different orbital type. Even if the direct spin-orbit coupling (first term of Eq.(30)) is small, ISC rates can be significantly enhanced by Herzberg-Teller effects (vibronic spin-orbit coupling, second term of Eq.(30)).

The adiabatic energies of the low-lying excited states (Figure 5) display three accessible ISC

channels: $S_1(\pi\rightarrow\pi^*) \rightsquigarrow T_1(\pi\rightarrow\pi^*)$, $S_1\ (\pi\rightarrow\pi^*) \rightsquigarrow T_2(\pi\rightarrow\pi^*)$ and $S_1(\pi\rightarrow\pi^*) \rightsquigarrow T_3(\pi\rightarrow\pi^*)$. One of the most important parameters that has to be considered in order to choose the most appropriate computational protocol is the treatment for the SOC operator, which will be used on Eq.(29). According to a recent work of Neese and coworkers(Neese, 2005) and de Souza and coworkers(de Souza et al., 2019), the RI-SOMF(1X) SOC treatment is recommended for accurate SOC calculations including the phosphorescence rate constant. Therefore the RI-SOMF(1X) method was the first option to calculate ISC rate constants. The first test calculation included all the vibrational frequencies, a small Gaussian bandwidth (inlinew keyword in ORCA nomenclature) of 10 $cm^{-1}$ and default number of points of the Fourier transform (npoints keyword in ORCA nomenclature) determined by the Cooley-Tuckey algorithm.

**Table 4.** *Computed ISC rate constants $k_{ISC}$ ($s^{-1}$) for MPh (298.15K) using Franck-Condon-Herzberg-Teller approximation ($k_{\mathrm{ISC}}^{\mathrm{FCHT}}$) and experimental results at room temperature employing RI-SOMF(1X) SOC-treatment and full TD-DFT.*

| ISC channel | $\Delta E_{ST}$ (eV) | Inlinew ($cm^{-1}$) | Npoints | $k_{ISC}^{FCHT}$ ($s^{-1}$) | $k_{ISC}$ (exp.) |
|---|---|---|---|---|---|
| $S_1$-$T_1$ | +0.85 | 10 | 262144 | -2.68 x $10^3$ | |
| $S_1$-$T_2$ | +0.88 | 10 | 524288 | 9.12 x $10^5$ | 7.90 x $10^{7}$[a] |
| $S_1$-$T_3$ | +0.065 | 10 | 131072 | -1.53 x $10^2$ | |

[a] ref.Wang et al., 2014.

As can be seen (Table 4), the only positive ISC rate constants were obtained by using 524288 points and a Gaussian bandwidth of 10 $cm^{-1}$ for the FT step. Therefore this number of points will be fixed to determine the effect of the Gaussian bandwidth on the ISC rate constant.

**Table 5.** *Spin-orbit coupling matrix elements (SOCMEs, $cm^{-1}$) and computed ISC rate constants $k_{ISC}$ ($s^{-1}$) for MPh (298.15K) using Franck-Condon-Herzberg-Teller approximation ($k_{\mathrm{ISC}}^{\mathrm{FCHT}}$) and experimental results at room temperature employing RI-SOMF(1X) SOC-treatment and full TD-DFT.*

| **Triplet sublevel** | **$\Delta E_{ST}$ (eV)** | **SOCME ($cm^{-1}$)** | **$k_{ISC}^{FCHT}$ ($s^{-1}$)** | **$k_{ISC}$ (exp.)** |
|---|---|---|---|---|
| $S_1$-$T_1$ | +0.85 | 0.13 | 7.39 x $10^3$ | |
| $S_1$-$T_2$ | +0.88 | 0.032 | 9.12 x $10^5$ | 7.90 x $10^{7a}$ |
| $S_1$-$T_3$ | +0.065 | 0.024 | 9.93 x $10^2$ | |
| Total $\mathbf{k_{ISC}}$ | - | - | 9.20 x $10^5$ | |

[a] ref.Wang et al., 2014.

Table 5 shows that 524288 points and a Gaussian bandwidth of 10 $cm^{-1}$ are enough to compute the Fourier transform employed by our ISC calculations. However, the calculated ISC rate constant is several orders of magnitude lower than the experimental ISC rate constant. Next, the dependency of the $k_{\mathrm{ISC}}^{\mathrm{FCHT}}$ on the Gaussian bandwidth was explored.

To test the dependency of the $k_{\mathrm{ISC}}^{\mathrm{FCHT}}$ on the Gaussian bandwidth, we computed the intersystem crossing rates for different Gaussian bandwidths (Table 15). According to these results the $k_{\mathrm{ISC}}^{\mathrm{FCHT}}$ is very sensitive to the variation of the Gaussian bandwidth because decreasing the Gaussian bandwidth enhances the intersystem crossing rates up to a factor of nine. Here, when a Gaussian bandwidth of 0.1 $cm^{-1}$ was used, we obtained an $k_{\mathrm{ISC}}^{\mathrm{FCHT}}$ of 8.34 x $10^6$ $s^{-1}$, which is in line with the experimental $k_{\mathrm{ISC}}$ (0.79 x $10^8$ $s^{-1}$). However, it might be possible that the grid of the calculations with a small Gaussian bandwidth (0.1-1.0 $cm^{-1}$) and 524288 points is too sparse and many oscillations were skipped. In addition, the number of points assigned for those calculations

by the Cooley-Tuckey algorithm is high (up to 33 million of points) and those calculations are very computationally expensive. Therefore 524288 points and a Gaussian bandwidth of 10 $cm^{-1}$ were chosen for all upcoming ISC computations.

As we noted before, dealing with torsional vibrational modes on this system is not an easy task. Hence, the effect of discarding vibrational modes below 100 $\mathrm{cm}^{-1}$ on the ISC rate constant calculation was tested:

**Table 6.** *Spin-orbit coupling matrix elements (SOCMEs, $cm^{-1}$) and computed ISC rate constants $k_{ISC}$ ($s^{-1}$) for MPh (298.15K) using Franck-Condon-Herzberg-Teller approximation ($k_{\mathrm{ISC}}^{\mathrm{FCHT}}$) and experimental results at room temperature employing the RI-SOMF(1X) SOC-treatment and full TD-DFT.*

| **Triplet sublevel** | **$\Delta E_{ST}$ (eV)** | **SOCME ($cm^{-1}$)** | **$k_{ISC}^{FCHT}$ ($s^{-1}$)** | **$k_{ISC}$ (exp.)** |
|---|---|---|---|---|
| $S_1$-$T_1$ | +0.85 | 0.13 | 1.05 x $10^7$ | |
| $S_1$-$T_2$ | +0.88 | 0.032 | 3.40 x $10^6$ | 7.90 x $10^{7}$[a] |
| $S_1$-$T_3$ | +0.065 | 0.024 | 2.21 x $10^6$ | |
| Total $\mathbf{k_{ISC}}$ | - | - | 1.61 x $10^7$ | |

[a] ref.Wang et al., 2014.

It is found that the $\mathrm{k_{ISC}}$ is enhanced when vibrational modes are discarded (Table 6). The increase of $\mathrm{k_{ISC}}$ may occur due to an improvement on the applicability of the harmonic oscillator after the discarding some torsional vibrational modes. However, the calculated ISC rate constant is about a factor of five lower than the experimental ISC rate constant. Thus, it is desirable to have an alternative approach to calculate an $\mathrm{k_{ISC}}$ that includes the contribution of all of the vibrational modes and yields a rate constant comparable to the experiment. The calculation of $\mathrm{k_{ISC}}$ using

AMFI SOC operator was explored as an alternative.

#### 5.2.5.2 ISC rate constant calculated using the AMFI SOC-operator

The AMFI SOC-operator has been extensively used to explore the intersystem-crossing of medium and large systems(Kleinschmidt et al., 2006; Perun et al., 2008). Unlike RI-SOMF(1X), AMFI computes analytically the Coulomb energy and it uses one SOC center to compute the mean-field energy. The calculated $k_{ISC}$ as a result of discarding the vibrational modes below 100 $cm^{-1}$ are shown in Table 7. Due to the small SOCMEs, a direct ISC rate of $\approx 8.79 \times 10^6$ $s^{-1}$ is computed, which is a factor of nine lower than the experimental value. Inclusion of Herzberg-Teller effects (vibronic SOC) significantly enhances the ISC rates by a factor of five ($\approx 4.61 \times 10^7$ $s^{-1}$) and the dominant channel is $S_1(\pi\rightarrow\pi^*) \rightsquigarrow T_1(\pi\rightarrow\pi^*)$. Thus, it can be concluded that the AMFI-SOC treatment is sufficient in describing the ISC process of MPh and it was chosen to investigate the ISC process of MPh.

**Table 7.** *Spin-orbit coupling matrix elements (SOCMEs, $cm^{-1}$) and computed ISC rate constants $k_{ISC}$ ($s^{-1}$) for MPh (298.15K) using the Franck-Condon ($k_{\mathrm{ISC}}^{\mathrm{FC}}$) and Franck-Condon-Herzberg-Teller approximation ($k_{\mathrm{ISC}}^{\mathrm{FCHT}}$) and experimental results at room temperature employing the AMFI SOC-treatment and full TD-DFT.*

| **Triplet sublevel** | **$\Delta E_{ST}$ (eV)** | **SOCME ($cm^{-1}$)** | **$k_{ISC}^{FC}$ ($s^{-1}$)** | **$k_{ISC}^{HT}$ ($s^{-1}$)** | **$k_{ISC}$ (exp.)** |
|---|---|---|---|---|---|
| $S_1$-$T_1$ | +0.85 | 0.21 | $5.92 \times 10^6$ | $3.14 \times 10^7$ | |
| $S_1$-$T_2$ | +0.88 | 0.064 | $9.91 \times 10^4$ | $9.94 \times 10^6$ | $7.90 \times 10^{7}$[a] |
| $S_1$-$T_3$ | +0.065 | 0.12 | $2.77 \times 10^6$ | $4.78 \times 10^6$ | |
| Total $k_{ISC}$ | - | - | $8.79 \times 10^6$ | $4.61 \times 10^7$ | |

[a] ref.Wang et al., 2014.

To shed light into how HT effects enhance the ISC rate, we analyzed the $\partial$SOCME contributions of the three ISC channels. All calculated $\partial$SOCME values (Table 16) are small. The largest $\partial$SOCME is 0.022 $cm^{-1}$, which involves in-plane vibrations that promotes the coupling between the $S_1(\pi\pi^*)$ and $T_2(\pi\pi^*)$ states of MPh, which is slightly higher than the $\partial$SOCME (0.017 $cm^{-1}$) for the $S_1(\pi\rightarrow\pi^*) \rightsquigarrow T_3$, which corresponds to in-plane vibrations. However, the dominant channel is $S_1(\pi\rightarrow\pi^*) \rightsquigarrow T_1$, in which the maximum variation of $\partial$SOCME is 0.0035 $cm^{-1}$, which corresponds to a combination of in-plane and out-of-plane vibrations. Thus, the vibronic SOC contributions to the ISC rate constants are independent of a specific type of vibrational mode.

To test the consistency of our calculations with respect to the level of theory, we calculated the intersystem crossing rates for different combinations of functionals and basis sets (see Figure 11). Vibronic SOC considerably enhances the ISC rate constants more than one order of magnitude. However, all the calculated vibronic rate constants ($k_{ISC}^{FCHT}$) at different levels of theory are in line with the experiment.

#### 5.2.5.3 Linearly interpolated paths

To gain insight into the non-radiative decay pathways after photoexcitation, linearly interpolated potential energy pathways (LIPs) between singlet and triplet state minima were computed.

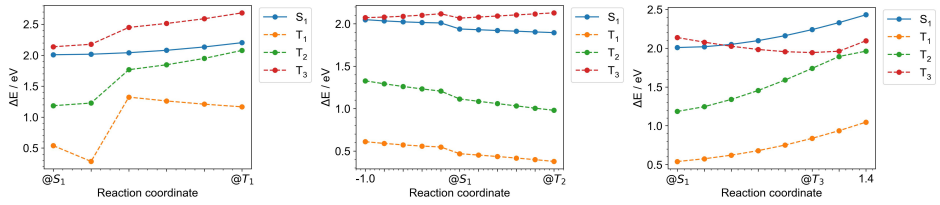


**(a)** $S_1 \rightarrow T_1$ **(b)** $S_1 \rightarrow T_2$ **(c)** $S_1 \rightarrow T_3$

**Figure 12.** Single-point calculations along a linearly interpolated path between the $S_1$(RC = 0) and target electronic state minima (RC = 1.0). The plotted energies are TD-DFT energies relative to the $S_0$ energy.

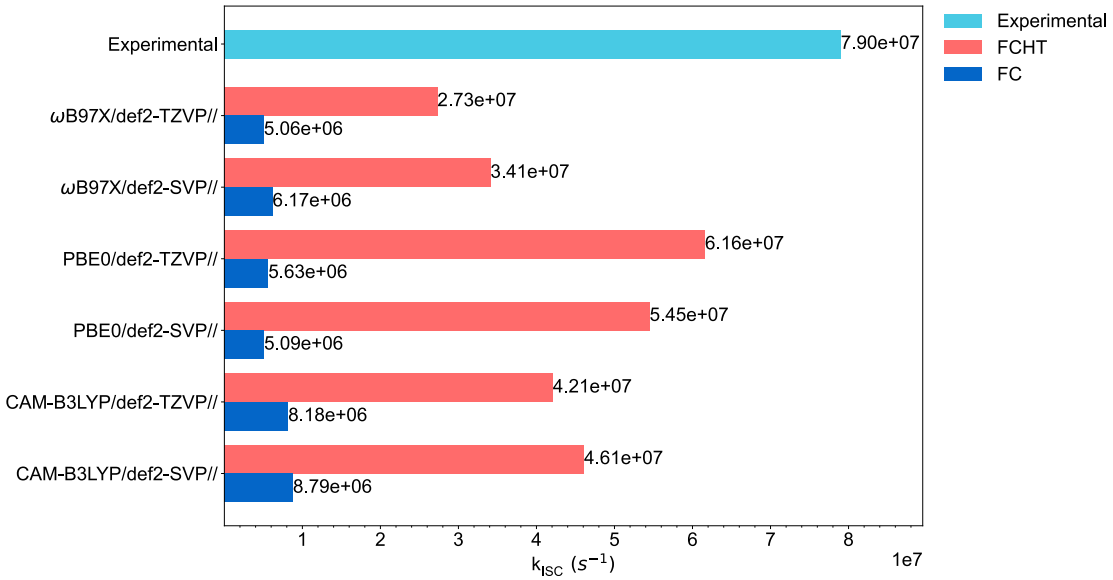


**Figure 11.** Effect of the level of theory on the ISC rate constants $k_{ISC}$ employing the FC (Franck-Condon) and Franck-Condon-Herzberg-Teller (FCHT) approximations. All calculations were performed at the CAM-B3LYP/def2-SVP optimized geometries, and using the SOCMEs calculated at the CAM-B3LYP/def2-SVP level of theory.

When energies are calculated with full TD-DFT, triplet instabilities may appear, as can be shown by the decrease of triplets energy in Figure 12(a). Therefore, a minimum on the $T_1$ with positive hessian could not be found by employing full TD-DFT. A crossing of the $S_1$ and $T_3$ PESs with a small energy barrier of 0.04 eV occurs along a pathway connecting their adiabatic minima (Figure 12(c)). In addition, this crossing is also found along the LIP between the $S_1$ and $T_2$ minima Figure 12(b) with a higher energy barrier ($\approx$ 0.1 eV) at about RC = -1.0. On the other hand, an internal conversion between $T_2$ and $T_3$ might occur due to another crossing located at ($\approx$ 0.07 eV) (Figure 12(c)).

#### 5.2.5.4 Jablonski diagram

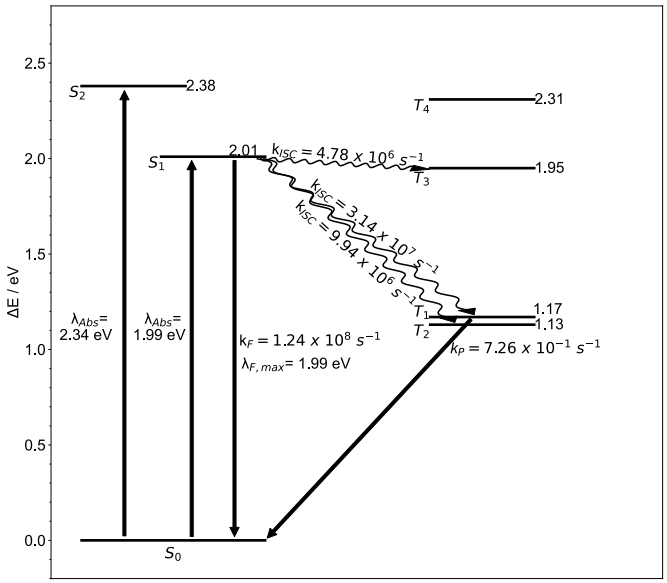


**Figure 13.** Jablonski diagram of MPh as a result of employing the first protocol. All energies are given relative to the ground state energy at the $S_0$ geometry.

According to our results, the following relaxation pathway (Figure 13) is proposed for MPh in toluene: once the MPh is excited to its bright $S_1$ state ($\lambda_{abs}$ = 1.99 eV), the main relaxation deactivation channel involves fluorescence with a rate constant of 1.24 x $10^8$ $s^{-1}$) due to the overestimation of the adiabatic energy of $S_1$. An alternative decay channel involve ISC via three channels $\{S_1(\pi \rightarrow \pi^*) \rightsquigarrow T_1, T_2, T_3(\pi \rightarrow \pi^*)\}$, in which $S_1(\pi \rightarrow \pi^*)$ and $T_1(\pi \rightarrow \pi^*)$ is the most efficient decay channel with a rate constant of 3.14 x $10^7$ $s^{-1}$). The depopulation of the $T_1$ state may involve an internal conversion process to the electronic ground state or an energy transfer to triplet oxygen, which in turn forms the singlet oxygen ($^1O_2$) (type II photoreaction), as it is experimentally determined ($\Phi_\Delta$ = 0.62).

As noted before, the $T_2$ and $T_3$ states are populated via ISC. Additionally, the $T_2$ state might be populated by an internal conversion between the $T_3$ and $T_2$ states.

## 5.3 Photophysics investigation under the second protocol

**5.3.1 Ground state minimum and vertical excitation energies** The TDA-DFT and TD-DFT vertical excitation energies of MPh are listed in Table 8 and the dominant Kohn-Sham molecular orbitals are depicted in Figure 14.

The first singlet excited state $S_1$ is dominated (weight of 75%) by the $\pi_{\mathrm{H}} \rightarrow \pi^*_{\mathrm{L}}$ transition with an oscillator strength of 0.330. The dominant contribution of the $S_2$ state (weight of 62%) corresponds to a $\pi_{\mathrm{H\text{-}1}} \rightarrow \pi^*_{\mathrm{L}}$ transition with an oscillator strength of 0.061. Both dominant transitions are consistent with the Gouterman model. Additionally, The $S_3$ state has some charge-transfer character due to the transitions from the $\pi_{\mathrm{H\text{-}2}}$ orbital; but this charge-transfer character is neither reflected in the dipole moments (see Figure 15), nor in the difference densities. The fourth excited state singlet $S_4$ is dominated (weight of 41%) by the $\pi_{\mathrm{H}} \rightarrow \pi^*_{\mathrm{L+1}}$ with an oscillator strength of 2.449. The lowest $T_1$ state has the $\pi_{\mathrm{H}} \rightarrow \pi^*_{\mathrm{L}}$ transition as the dominant configuration, while $T_2$, $T_3$ and $T_4$ have the dominant configurations of $\pi_{\mathrm{H\text{-}1}} \rightarrow \pi^*_{\mathrm{L}}$, $\pi_{\mathrm{H}} \rightarrow \pi^*_{\mathrm{L+1}}$ and $\pi_{\mathrm{H\text{-}1}} \rightarrow \pi^*_{\mathrm{L+1}}$ respectively. Above $S_2$ there are $\pi \rightarrow \pi^*$ transitions, whose energies correspond to bands outside the Q-region of the absorption spectrum. Therefore, they are not considered in the present work.

To test the performance of our protocol for describing the excited states, we compared the VEE of MPh employing Tamm-Dancoff approximation (TDA-CAM-B3LYP) and full TD-DFT (TD-CAM-B3LYP). The orbital contributions to the excitations calculated with TDA and full TD-DFT are very similar. However, the $S_3$ and $S_4$ states swap order at the ground state geometry, which are not relevant for the description of the Q-band vibronic spectrum. In addition, $T_1$ and $T_2$ states also swap the energetic order. The change of the state ordering might be related to the triplet instability associated with the $T_1$ and $T_2$ states as a result of employing full TD-DFT.(Peach et al., 2011)

The CAM-B3LYP/def2-SVP VEE is about 0.5 eV higher than the experimental band maximum, for the $S_2$ transition the difference is about 0.3 eV. It is worth mentioning that the band maximum and the vertical excitation energy do not coincide and that the VEE is more than 0.1 eV higher than the calculated band maximum.

**Table 8.** *Vertical singlet and triplet excitation energies (eV) in toluene (calculated applying the Tamm-Dancoff approximation), and the magnitudes of transition dipole moments (Debye) calculated at the CAM-B3LYP/def2-SVP ground state geometry (employing the Tamm-Dancoff approximation).*

| **Electronic state**[a] | **Electronic structure** | **TDA-CAM-B3LYP**[b] | **TD-CAM-B3LYP** | **Experiment** | **($\|\mu\|$, Debye)** |
|---|---|---|---|---|---|
| $S_1$ | (0.75) $\pi_H \rightarrow \pi^*_L$<br>(0.19)$\pi_{H-1} \rightarrow \pi^*_{L+1}$ | 2.34 (0.330) | 2.18 (0.292) | 1.85[c] 1.86[de] | 6.10 |
| $S_2$ | (0.62) $\pi_{H-1} \rightarrow \pi^*_L$<br>(0.33)$\pi_H \rightarrow \pi^*_{L+1}$ | 2.65 (0.061) | 2.52 (0.075) | 2.30[d] 2.31[ce] | 2.46 |
| $S_3$ | (0.27) $\pi_{H-1} \rightarrow \pi^*_{L+1}$<br>(0.24)$\pi_{H-2} \rightarrow \pi^*_L$<br>(0.17) $\pi_{H-2} \rightarrow \pi^*_{L+1}$<br>(0.12) $\pi_H \rightarrow \pi^*_{L+1}$ | 3.65 (0.874) | 3.42 (1.140) | - | 7.95 |
| $S_4$ | (0.41) $\pi_H \rightarrow \pi^*_{L+1}$<br>(0.22) $\pi_{H-1} \rightarrow \pi^*_{L+1}$<br>(0.21) $\pi_{H-1} \rightarrow \pi^*_L$ | 3.69 (2.449) | 3.33 (1.439) | - | 13.2 |
| $T_1$ | (0.56) $\pi_H \rightarrow \pi^*_L$<br>(0.32)$\pi_{H-1} \rightarrow \pi^*_L$ | 1.55 | 1.52 | - | - |
| $T_2$ | (0.57) $\pi_{H-1} \rightarrow \pi^*_L$<br>(0.37)$\pi_H \rightarrow \pi^*_L$ | 1.77 | 0.81 | - | - |

| Electronic state[a] | Electronic structure | TDA-CAM-B3LYP[b] | TD-CAM-B3LYP | Experiment | ($\|\mu\|$, Debye) |
|---|---|---|---|---|---|
| $T_3$ | (0.85) $\pi_H \rightarrow \pi^*_{L+1}$ | 2.24 | 2.06 | - | - |
| $T_4$ | (0.86) $\pi_{H-1} \rightarrow \pi^*_{L+1}$ | 2.59 | 2.44 | - | - |

[a]Dominant contributions at CAM-B3LYP/def2-SVP level of theory (calculated applying the Tamm-Dancoff approximation).

[b] Oscillator strength (length) on parenthesis.

[c]Ref.(Balashova et al., 2021) maximum of absorption band.

[d]Ref.(Rodriguez Prada, 2018) maximum of absorption band.

[e]Ref.(Briat et al., 1967) maximum of absorption band.

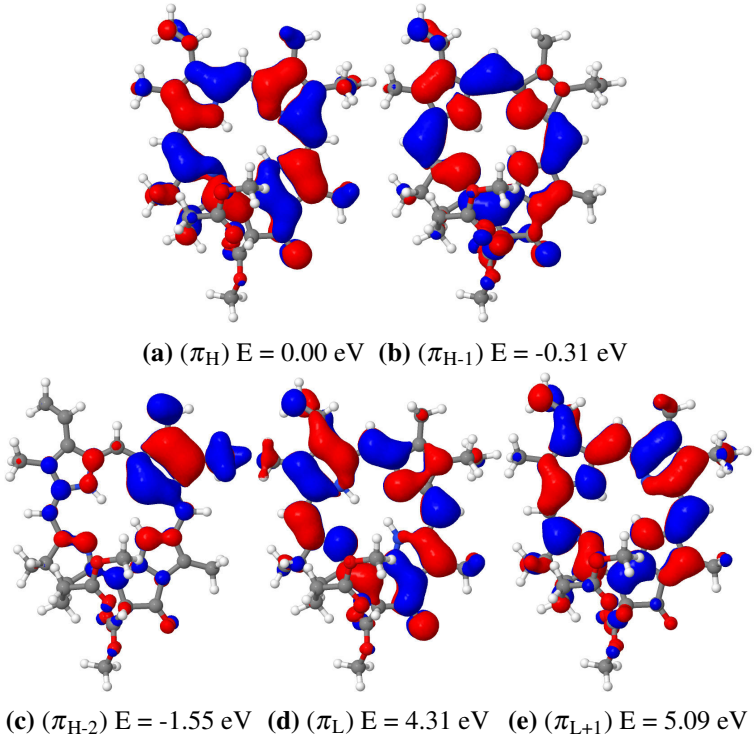

**(a)** ($\pi_H$) E = 0.00 eV **(b)** ($\pi_{H-1}$) E = -0.31 eV

**(c)** ($\pi_{H-2}$) E = -1.55 eV **(d)** ($\pi_L$) E = 4.31 eV **(e)** ($\pi_{L+1}$) E = 5.09 eV

**Figure 14.** Frontier molecular orbitals at the $S_0$ geometry of methylpheophorbide a (isovalue 0.01). The energies are listed relative to the energy of the HOMO.

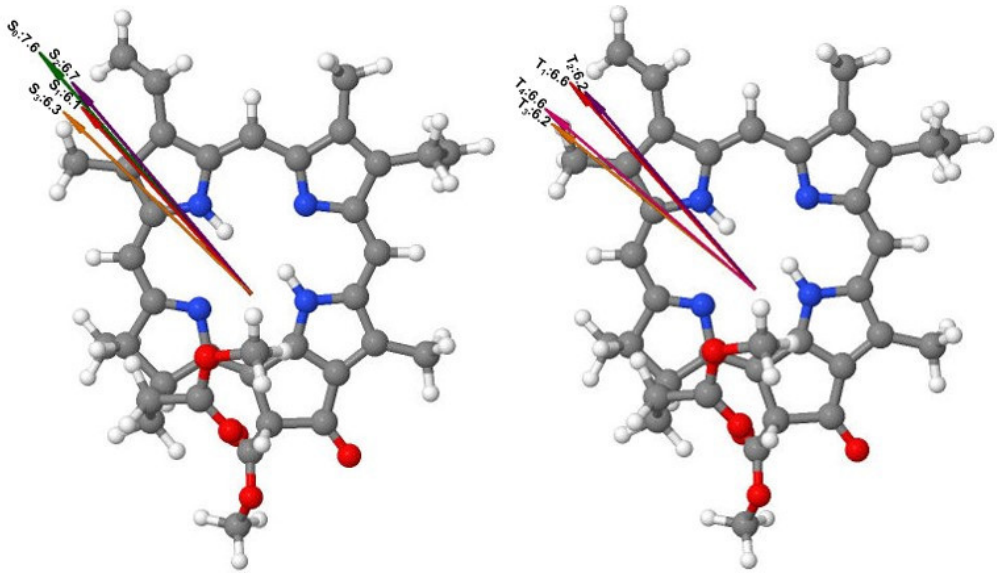


**Figure 15.** Negative dipole moments of the lowest singlet $S_0$-$S_3$ and triplet $T_1$-$T_4$ excited states in MPh, calculated at the CAM-B3LYP/def2-SVP ground state geometry under TDA. The magnitudes of the dipole moments are given in Debye.

To gain some insight into the effect of a polar solvent on the energetic stabilization or destabilization of the excited states, we investigated the dipole moments of the low-lying excited states (see Figure 15), the $S_2$, $T_1$ and $T_4$ states should display a small energetic destabilization in the presence of a polar solvent. In contrast, $S_1$, $S_3$ and $T_2$-$T_3$ are expected to be somewhat stronger destabilized relative to the ground state in polar solvents.

**5.3.2 Geometries of the excited state minima** Since the optimization of the lowest-excited state singlets is the same for both of the protocols, the following discussion will be focused on the triplets geometry differences (Figure 16). In the $T_1$ state, the $C_4$–$C_5$ distance and the $C_5$–$C_6$ distance are extended by 6 pm and shortened by 5 pm, respectively. The $C_3$–$C_4$, $C_9$–$N_{22}$ distances are shortened by 4 pm and the $C_6$–$N_{22}$ distance is elongated by 4 pm. In the $T_3$ state, the principal variations are the $C_9$–$C_{10}$, $C_{11}$–$C_{12}$ distance elongation of 4 pm and the $C_{10}$–$C_{11}$ distance

shortening of 3 pm.

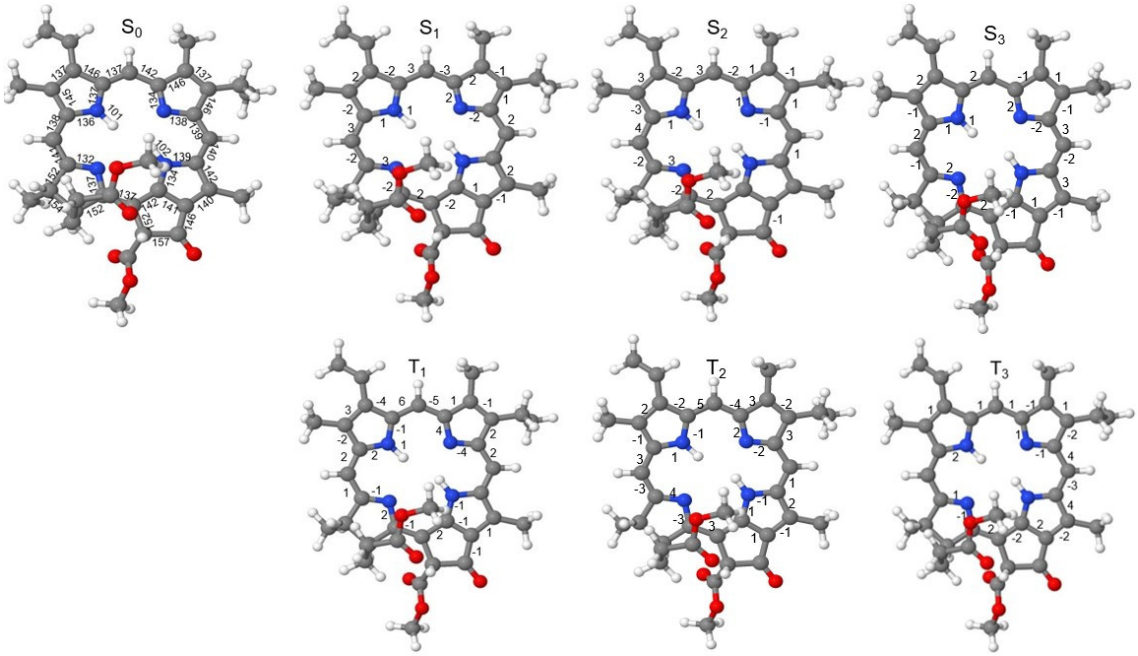


**Figure 16.** Selected bond lengths (in pm) of the ground state, and differences relative to the ground state structure. Only non-zero values are given.

The energies of the ground and excited states are presented in Figure 17. The adiabatic excitation energy of $S_1$ state is equal to 2.20 eV (2.18 eV taking into account the zero-point vibrational energy) and exhibiting a structural relaxation effect corresponding to a stabilization of 0.14 eV. In contrast, relaxation effects exert a comparatively minor influence on the $S_2$ and $S_3$ excited states (0.09 and 0.06 eV).

The adiabatic energy of the $T_1$ state is 1.28 eV (1.25 eV including ZPVE), which is within the range of the adiabatic energies of a series of chlorins calculated by Palma and coworkers(Palma et al., 2008) at the B3LYP/6-31G(d) level of theory in the gas phase. Adiabatically, the second, third and fourth triplet excited state energies amount to 1.61, 2.07 and 2.44 eV (1.70, 2.11, 2.45 eV taking into account ZPVE). Structural relaxation has a major impact on the $T_1$ state (0.27 eV)

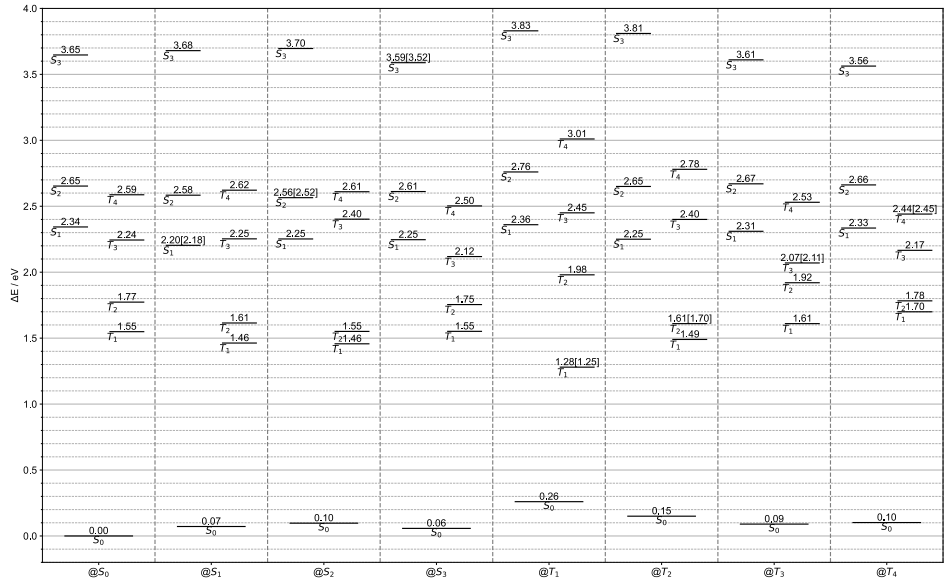


**Figure 17.** State energies (DFT, [eV]) calculated at the optimized geometries of the $S_0$, $S_1$, $S_2$, $S_3$, $T_1$, $T_2$, $T_3$, $T_4$ states of methylpheophorbide a. All energies are set relative to the ground state energy at $S_0$ geometry and computed under TDA.

and a less pronounced impact on the $T_2$ state (0.16 eV), $T_3$ state (0.17 eV) and $T_4$ state (0.15 eV). Since the $T_1$, $T_2$ and $T_3$ states exhibit lower energies than $S_1$ (2.20 eV), intersystem crossing is possible between the $S_1$ excited state and the $T_1$, $T_2$ and $T_3$ states.

**5.3.3 Q-band region of the absorption spectrum** The Q-band region of the calculated and the experimental absorption spectrum is shown in Figure 18. As noted in the previous protocol, The Franck-Condon approximation gives a reasonable description of the spectrum, since the Herzberg-Teller contribution has little influence on the shape of the spectrum.

To test the effect of the level of theory on the absorption properties of MPh, we employed the CAM-B3LYP/def2-SVP optimized geometries and performed single point calculations with the density functionals CAM-B3LYP, $\omega$B97X, PBE0 and the basis sets def2-SVP, def2-TZVP (see Table 19). The calculated VEEs for $S_1$ are found to be very similar to the three functionals, with

differences of $\leq 0.1$ eV. Larger differences between the three functionals are shown for the $S_2$ state. The utilization of the def2-SVP basis has a minimal impact on the VEEs, with blue shifts of less than 0.05 eV observed for the $S_1$ and $S_2$ transitions with the CAM-B3LYP functional, in accordance with the previous protocol.

As can be expected, the shape of the calculated absorption spectrum under TDA is similar but is blue-shifted. The calculated vibronic progression associated with the $S_0 \rightarrow S_1$ absorption spectrum shows a band maximum at 1.86 eV and spans the whole Q-region, while the band located at 2.20 eV describes the $S_0 \rightarrow S_2$ vibronic progression. Both bands correspond to 0-0 transitions, as can be seen in the vibronic spectrum at 0K (Figure 18). The $Q_y$ and $Q_x$ bands are in agreement with the Gouterman's model and MCD spectrum of MPh(Reimers et al., 2013).

Finally, we compared the VEEs calculated at the ground state geometry with the calculated band maxima. The VEEs are blue-shifted by 0.16 eV and 0.13 eV with respect to the calculated $S_1$ and $S_2$ band maxima (Figure 18), which is within the range found in a recent benchmark study by Bai and coworkers(Bai et al., 2020).

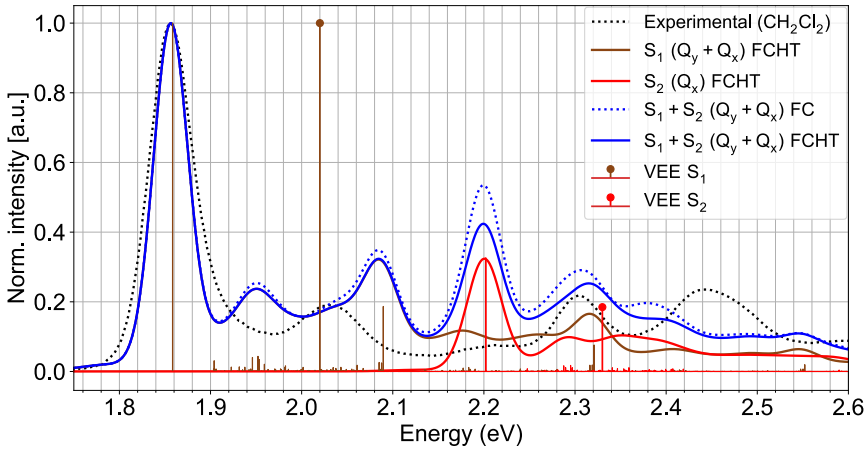


**Figure 18.** Computed vibronic structure of the Q region of the absorption spectrum employing the adiabatic Hessian model, and including Franck-Condon (FC) and Franck-Condon and Herzberg-Teller (FCHT) terms at 298.15 K. The Gaussian bandwidth was set to 150 $cm^{-1}$ and vibrational modes below 350 $cm^{-1}$ were discarded. The stick spectrum was calculated at 0 K. A stick spectrum calculated at 298.15 K is presented in Figure 35. The calculated spectra were displaced 0.32 eV to the left to align with the experimental spectrum.

#### 5.3.3.1 Vibronic structure calculated by VG and AHAS approximations

As mentioned in the previous protocol, the band shape of the absorption spectrum changes according to the approximation that is chosen (see Figure 19 and Figure 20). Additionally, it is observed that the calculated absorption spectra is blue-shifted with respect to the calculated absorption spectra under full TD-DFT.

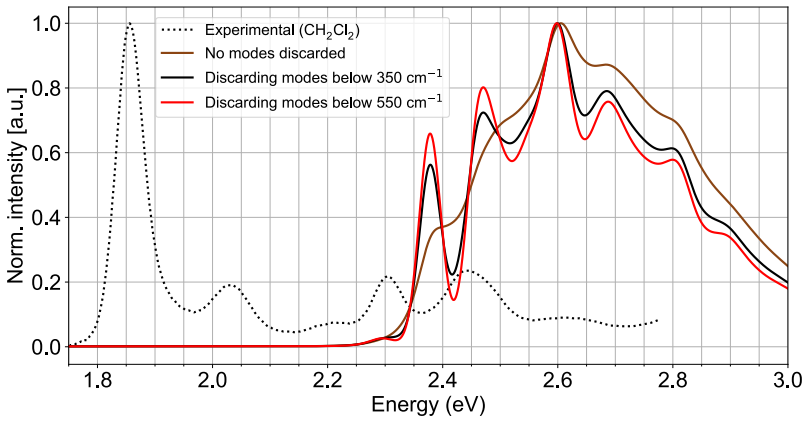


**Figure 19.** Computed vibronic structure of the Q region of the absorption spectrum employing the VG approximation and FCHT contribution at 298.15K. The Gaussian bandwidth was set to 150 $\mathrm{cm}^{-1}$.The vibrational modes below 350 $\mathrm{cm}^{-1}$ were discarded.

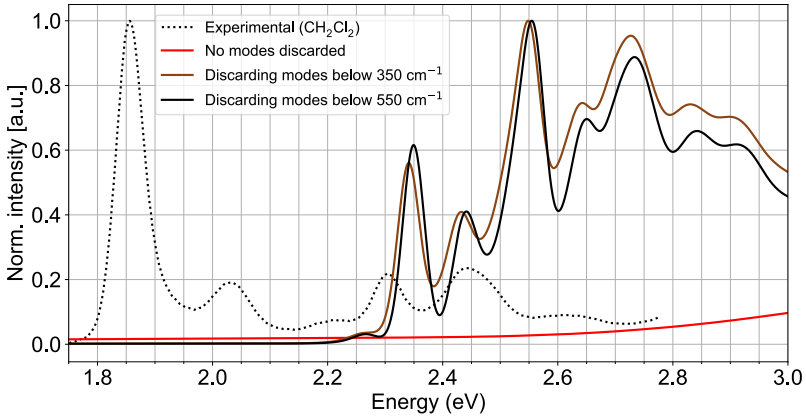


**Figure 20.** Computed vibronic structure of the Q region of the absorption spectrum employing the AHAS approximation and FCHT contribution at 298.15K. The Gaussian bandwidth was set to 150 $\mathrm{cm}^{-1}$.The vibrational modes below 350 $\mathrm{cm}^{-1}$ were discarded.

**5.3.4 Fluorescence and phosphorescence** As can be seen in Figure 22, the influence of the FCHT contribution on the fluorescence spectra is an increment of emission intensity, as observed in the previous protocol. The calculated fluorescence band maximum $\lambda_{\mathrm{F}}$ of MPh is 2.18 eV and the fluorescence rate constant is 1.38 x $10^8$ $s^{-1}$ using the FC approximation (Table 9). Including HT effects in the calculations results in a fluorescence rate constant of rate of 1.83 x $10^8$ $s^{-1}$ (Figure 21).

A larger overestimation of the fluorescence rate in comparison to the calculated value under TD-DFT might be due to the use of TDA, which contributes to a larger overestimation of the $S_1$ adiabatic energy difference in our calculations.

**Table 9.** *Adiabatic energy difference ($\Delta E_{S0\text{-}S1}$, eV), fluorescence rate constant ($k_F$, $s^{-1}$), fluorescence band maximum ($\lambda_F$, eV), transition dipole moment between the $S_1$ and $S_0$ states ($\mu^2$ [$S_1 \rightarrow S_0$], $au^2$) and oscillator strength $f_{osc}$, computed at the TDA-DFT/CAM-B3LYP(C-PCM)/def2-SVP level of theory.*

| **Property** | **Value**[b] | **Experiment**[c] **($s^{-1}$)** |
|---|---|---|
| $\Delta E_{S0–S1}$ | 2.20 | - |
| $k_F$ | 1.38 x $10^8$ | 0.32 x $10^8$ |
| $\lambda_F$ | 2.18 | 1.83 |
| $\mu^2$ ($S_1 \rightarrow S_0$) | 5.96 | - |
| $f_{osc}$ | 3.42 x $10^{-1}$ | - |

[a] ref. Wang et al., 2014 [b] calculated using the FC approximation

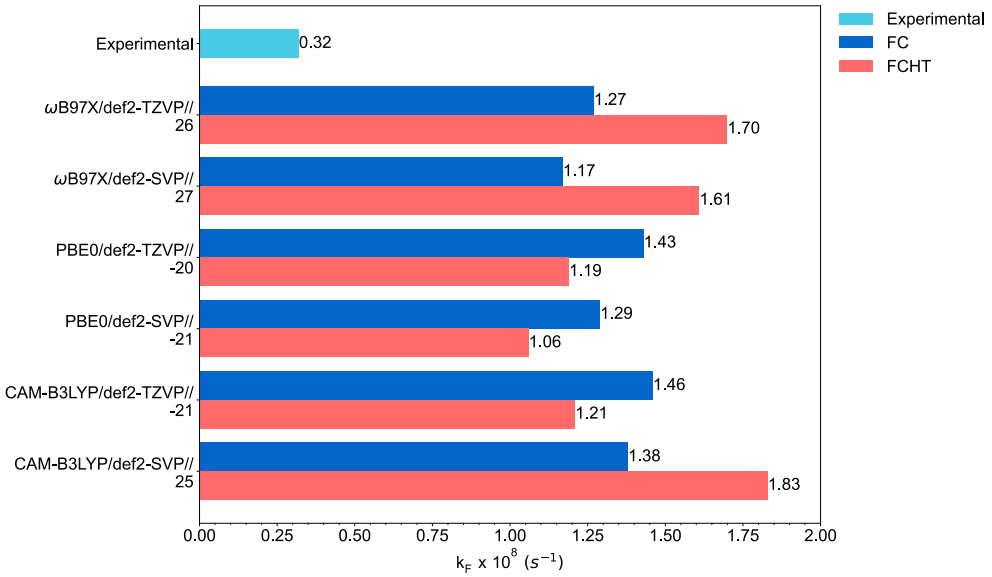


**Figure 21.** Fluorescence rate constants computed at different levels of theory employing the FC and FCHT approximations effects. The geometry obtained by the CAM-B3LYP/def2-SVP was fixed. The values under the labels are the relative Herzberg-Teller contributions.

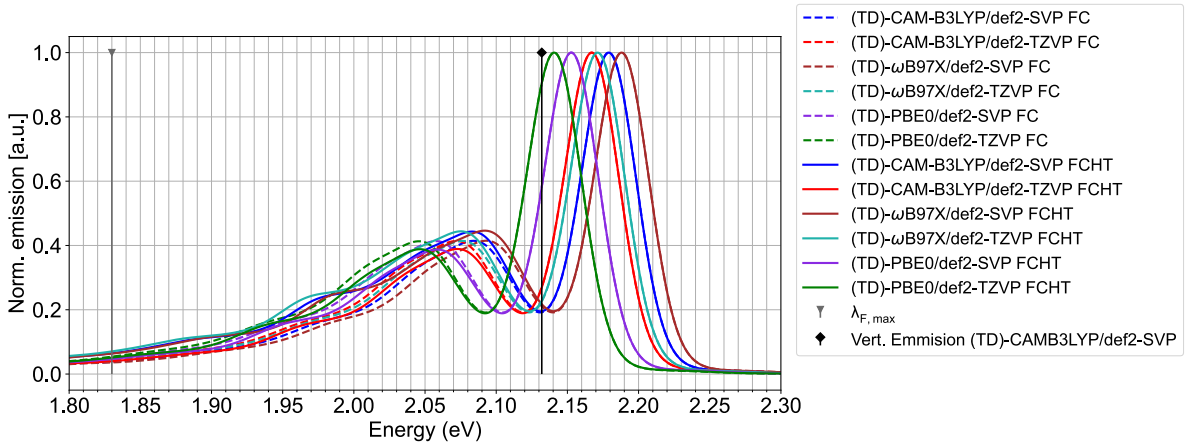


**Figure 22.** Predicted fluorescence spectra calculated with different functionals and basis sets using the FC and FCHT approximations. The CAM-B3LYP/def2-SVP optimized geometry was used in all calculations. The experimental band maximum is shown in gray.

The effect of the level of the theory on the fluorescence spectra and rate constant is shown in Figure 21 and Figure 22. Figure 21 indicates that the density functional exerts a minor influence on the fluorescence rate. The effect of the inclusion of HT effects is also small. As noted before, the influence of changing from the def2-SVP to the def2-TZVP basis set is a small red shift of the fluorescence band of up to 0.02 eV. Overall, the effect of the level of theory (basis set and functional) and Herzberg-Teller effects on the simulated fluorescence spectrum is small (Figure 22). Furthermore, the computed TDA-DFT band maximum agrees reasonably well with the experimental emission band maximum, with a deviation of ≈0.3 eV, which is within the expected range for the current methodology. Moreover, the vertical emission energy is red-shifted with respect to the band maximum by 0.05 eV. Due to the similarity of the calculated values and for consistency, we chose the TDA-DFT/CAM-B3LYP(C-PCM)/def2-SVP level of theory to calculate the fluorescence properties of our system considering only the FC approximation.

Experimentally it is found that MPh is essentially non-phosphorescent. Nevertheless, for the sake of completeness the phosphorescence rate constants ($k_P$) were calculated. It is assumed that the $T_{1,+1}$, $T_{1,0}$, $T_{1,-1}$ triplet sublevels are equally populated (high temperature average). Consistent with the experimental findings, a very slow phosphorescence process ($k_P$ = 1.25 x $10^{-1}$ $s^{-1}$) is predicted due to the small transition dipole moments ($10^{-6}$-$10^{-4}$ a.u.) (see Table 10).

**Table 10.** *Phosphorescence rate constants $k_P$ ($s^{-1}$), transition dipole moments $|\mu_{el}(S_0 \leftarrow T_{1,\alpha})|$ (a.u.) and radiative lifetimes $\tau_P$ (s) for the three spin sublevels of the $T_1$ state computed at the ground state minimum.*

| **Sublevel** | $\|\mu^2$ **($S_0 \leftarrow T_{1,a}$)**$\|$ | $k_P$ **(298.15K)** | $\tau_P$ |
|---|---|---|---|
| $T_{1,+1}$ | 6.23 x $10^{-6}$ | 2.16 x $10^{-2}$ | 4.63 x $10^{1}$ |
| $T_{1,0}$ | 7.15 x $10^{-5}$ | 4.39 x $10^{-2}$ | 2.28 x $10^{1}$ |
| $T_{1,-1}$ | 1.01 x $10^{-4}$ | 3.08 x $10^{-1}$ | 0.32 x $10^{1}$ |
| High temperature average | | 1.25 x $10^{-1}$ | 0.80 x $10^{1}$ |

**5.3.5 Intersystem crossing channels** From the $S_1$ minimum, accesible non-radiative ISC channels in MPh may arise from the $S_1 \rightarrow T_1$, $S_1 \rightarrow T_2$, and $S_1 \rightarrow T_3$ decay. The calculated ISC rates under AMFI SOC treatment are shown in Table 11. As expected from El-Sayed's rule, the SOCMEs between $S_1$ ($\pi\pi^*$) and $T_1$-$T_3$ ($\pi\pi^*$) states are small. As a consequence, a direct ISC rate of $\approx$ 7.43 x $10^6$ $s^{-1}$ is calculated, which is one order of magnitude smaller than the experimental value. Inclusion of Herzberg-Teller effects (vibronic SOC) significantly enhances the ISC rates by a factor of eight ($\approx$ 6.14 x $10^7$ $s^{-1}$). This value is in very good agreement with the experimental value. The fastest ISC rate induced by vibronic SOC is calculated for the transition $S_1(\pi \rightarrow \pi^*) \rightsquigarrow T_3(\pi \rightarrow \pi^*)$ which is related to the small energy gap. In order to gain more insight into how HT effects enhance the ISC rate, we compare the contributions of the derivatives of the SOCMEs with respect to the normal mode coordinates ($\partial$SOCME) of the three ISC channels. All calculated $\partial$SOCME values (Table 21) are small. For the $S_1(\pi \rightarrow \pi^*) \rightsquigarrow T_3(\pi \rightarrow \pi^*)$ channel the maximum variation of $\partial$SOCME is 0.022 $cm^{-1}$, which corresponds to an in-plane deformation of the chlorin macrocycle (Table 22). In contrast, the maximum variation of $\partial$SOCME for the $S_1(\pi \rightarrow \pi^*) \rightsquigarrow T_1(\pi \rightarrow \pi^*)$ and

$S_1(\pi\rightarrow\pi^*) \rightsquigarrow T_2(\pi\rightarrow\pi^*)$ channels is 0.003 and 0.008 $cm^{-1}$, respectively. The latter derivative is associated with an out-of-plane mode of the chlorin macrocycle. This indicates that the contributions of Herzberg-Teller effects to the ISC rate constants do not depend on a specific type of vibrational mode.

**Table 11.** *Spin-orbit coupling matrix elements (SOCMEs, $cm^{-1}$) and computed ISC rate constants $k_{ISC}$ ($s^{-1}$) for MPh (298.15K) using the Franck-Condon ($k_{ISC}^{FC}$) and Franck-Condon-Herzberg-Teller approximation ($k_{ISC}^{FCHT}$) and experimental results at room temperature employing the AMFI SOC-treatment and TDA-DFT approximation.*

| ISC channel | $\Delta E_{ST}$ (eV) | SOCME | $k_{ISC}^{FC}$ | $k_{ISC}^{FCHT}$ | $k_{ISC}$ (exp.) |
|---|---|---|---|---|---|
| $S_1$-$T_1$ | +0.92 | 0.16 | 5.80 x $10^5$ | 7.10 x $10^6$ | |
| $S_1$-$T_2$ | +0.59 | 0.44 | 3.10 x $10^6$ | 2.08 x $10^7$ | 7.90 x $10^7$ [a] |
| $S_1$-$T_3$ | +0.13 | 0.10 | 3.75 x $10^6$ | 3.35 x $10^7$ | |
| Total $k_{ISC}$ | - | - | 7.43 x $10^6$ | 6.14 x $10^7$ | |

[a] ref.Wang et al., 2014.

#### 5.3.5.1 Linearly interpolated paths

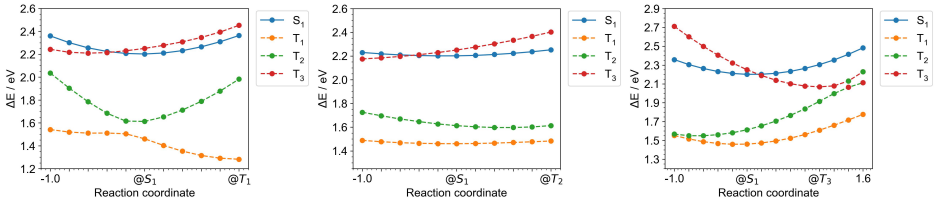


**(a)** $S_1 \rightarrow T_1$ **(b)** $S_1 \rightarrow T_2$ **(c)** $S_1 \rightarrow T_3$

**Figure 23.** Single-point calculations along a linearly interpolated path between the $S_1$(RC = 0)and target electronic state minima (RC = 1.0). The plotted energies are TDA-DFT energies relative to the $S_0$ energy.

To obtain further insight into the three non-radiative ISC channels and the decay mechanisms of MPh, linearly interpolated paths (LIP) were constructed, connecting the $S_1$ and low-lying triplet state minima (Figure 23). Close to the $S_1$ minimum, a crossing between the $S_1(\pi \rightarrow \pi^*)$ and $T_3(\pi \rightarrow \pi^*)$ PESs is found with a small energy barrier (0.001-0.02 eV) along the three relaxation pathways. Here the overlap between the vibrational wave functions of the $S_1(\pi \rightarrow \pi^*)$ and $T_3(\pi \rightarrow \pi^*)$ PESs is increased, which in turn benefits the $S_1(\pi \rightarrow \pi^*) \rightsquigarrow T_3(\pi \rightarrow \pi^*)$ channel. Figure 23(a)-(b) show that the $T_1$ and $T_2$ PESs do not intersect, which reflects that their vibrational coupling is small. Additionally, from the $T_2$ minimum (Figure 23(b)), the $T_1$ and $T_2$ PESs show parallel tracks, which may indicate a possible internal conversion between the $T_1$ and the $T_2$ excited states. Furthermore, The $T_2$ and $T_3$ excited states might be connected by an internal conversion mediated by an avoided crossing located at ≈0.06 eV above the $T_3$ minimum (Figure 23(c)).

To test the robustness of our results with respect to the choice of the Gaussian linewidth and the number of roots used in the spin-orbit-coupling-induced-mixing of the $S_1$, $T_1$, $T_2$ and $T_3$ states, we calculated the intersystem crossing rates for different values of these parameters (see Table 23, and Table 24). As can be seen, the effect of these parameters on the calculated ISC rates is negligible.

There is, however, a small effect of the level of theory (density functional and basis set) on the direct ($k_{ISC}^{FC}$) and vibronic ($k_{ISC}^{FCHT}$). Vibronic SOC enhances the ISC rate constant from a factor of 5 to a factor of 9 (see Figure 24). It is noteworthy that the overall predicted vibronic ISC rate constants ($k_{ISC}^{FCHT}$) calculated at different levels of theory are all in good agreement with experiment. ($k_{ISC}$ = 0.79 x $10^8$ $s^{-1}$).

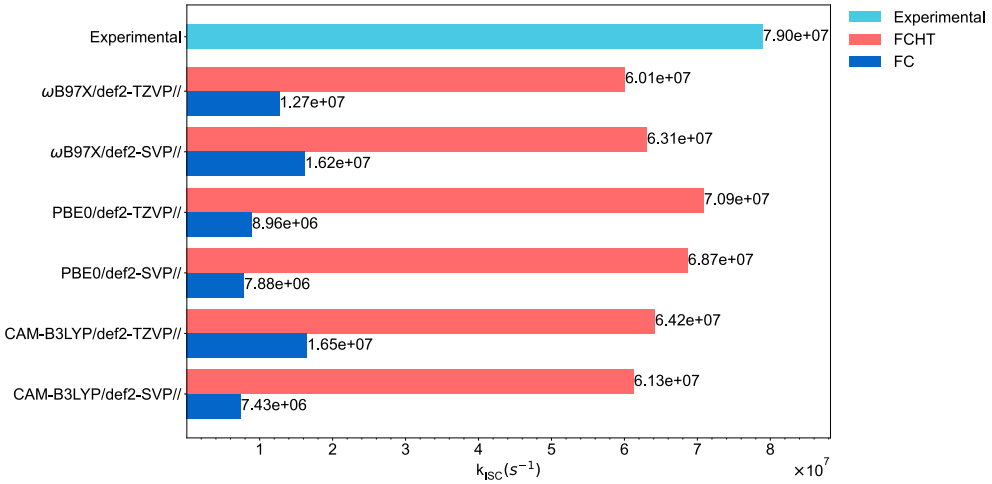


**Figure 24.** Effect of the level of theory on the ISC rate constants $k_{ISC}$ employing the FC (Franck-Condon) and Franck-Condon-Herzberg-Teller (FCHT) approximations. All calculations were performed at the CAM-B3LYP/def2-SVP optimized geometries, and using the SOCMEs calculated at the CAM-B3LYP/def2-SVP level of theory.

### 5.3.5.2 Jablonski diagram

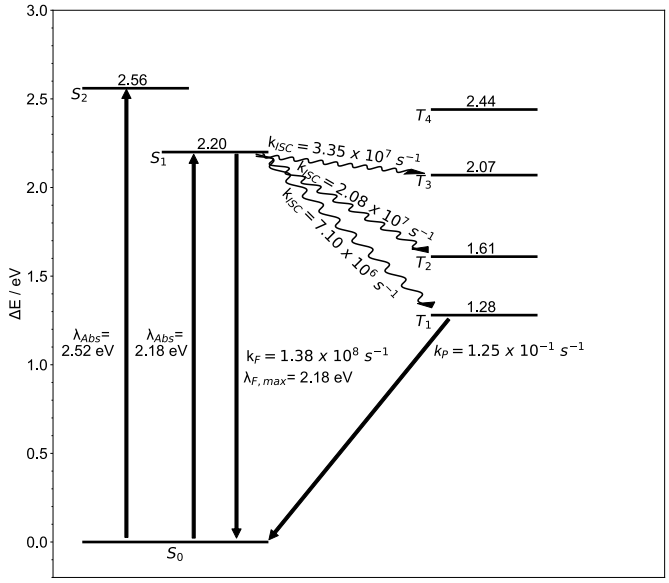


**Figure 25.** Jablonski diagram of MPh as a result of employing the second protocol.All energies are given relative to the ground state energy at the $S_0$ geometry.

The following decay mechanism (Figure 25) is proposed for MPh in toluene: once excited

to the bright $S_1$ state the system may decay via internal conversion to the electronic ground state, undergo fluorescence or ISC via three channels $\{S_1(\pi \rightarrow \pi^*) \rightsquigarrow T_1, T_2, T_3(\pi \rightarrow \pi^*)\}$. Our calculations indicate that fluorescence is the dominant deactivation channel with a rate constant $k_F$ = 1.65 x $10^8$ $s^{-1}$. This value is, however, an overestimation. An alternative decay mechanism involves an efficient due to the overestimation of the adiabatic energy of $S_1$. However, an alternative decay mechanism involves an efficient $S_1(\pi \rightarrow \pi^*) \rightsquigarrow T_3$ ISC ($k_{ISC}$ = 3.35 x $10^7$ $s^{-1}$), which is then followed by an internal conversion to the $T_2$ state. This state can then decay to $T_1$ via subsequent internal conversion. The $T_1$ and $T_2$ states may also be directly populated from the $S_1$ state, with rate constants of 7.10 x $10^6$ $s^{-1}$ and 2.08 x $10^7$ $s^{-1}$, respectively. The $T_1$ state can either decay via internal conversion to the electronic ground state or undergo an energy transfer to triplet oxygen in which singlet oxygen ($^1O_2$) is formed while the decay to the ground state is taking place (type II photoreaction), as is experimentally observed ($\Phi_\Delta$ = 0.62).

## 6 General conclusions

We have tested two protocols to investigate the photophysics of methylpheophorbide a in toluene using the CAM-B3LYP/def2-SVP level of theory. Additionally, the effect of different functionals (CAM-B3LYP, $\omega$B97X and PBE0) and different basis sets (def2-SVP and def2-TZVP) on the calculated photophysical properties was evaluated. Both of the protocols indicate that MPh has a bright $S_1$ and $S_2$ states in the visible region, which dominated by $\pi \rightarrow \pi^*$ electronic transitions. These transitions are associated with the Q-band. The shape of the Q-band of the absorption spectrum of MPh is reasonable well described in the Franck-Condon picture, with only small Herzberg-Teller contributions within both protocols. The calculated band maxima of the $Q_y$ and $Q_x$ bands exhibit blue shifts with respect to the experimental absorption bands, with a difference of approximately 0.14 and 0.03 for the first protocol and 0.3 and 0.2 eV for the second protocol,

respectively.

As a consequence of the energy overestimation by the method, The computed fluorescence rate constant under the first (1.24 x $10^8$ $s^{-1}$) and second(1.65 x $10^8$ $s^{-1}$) protocol are in agreement with the experimental rate constant (0.32 x $10^8$ $s^{-1}$) but are overestimated by a factor of about four and five, respectively, which leads to the prediction that fluorescence is faster than ISC, contrary to the experimental observation. Furthermore, the fluorescent band maximum of 1.99 and 2.18 eV for the first and second protocol, are in agreement with the experimental band maximum (1.83 eV). On the other hand, the effect of the level of theory on the calculated rate constants and spectra is similar between both protocols. Nevertheless, for the first protocol, the deviation between the computed and experimental band maxima ($\approx$0.21 eV) is lower than the deviation found for the second protocol ($\approx$0.3 eV).

Both protocols predict three triplet states ($T_1$, $T_2$, and $T_3$) below the first singlet-excited state ($S_1$). Therefore, there are three accessible ISC pathways: the $\mathrm{S}_1(\pi \rightarrow \pi^*) \rightsquigarrow \mathrm{T}_1(\pi \rightarrow \pi^*)$, $\mathrm{S}_1(\pi \rightarrow \pi^*) \rightsquigarrow \mathrm{T}_2(\pi \rightarrow \pi^*)$ and the $\mathrm{S}_1(\pi \rightarrow \pi^*) \rightsquigarrow \mathrm{T}_3(\pi \rightarrow \pi^*)$ channels. While the vibronic SOC calculated by the first protocol enhaced the ISC rate by a factor of five, the calculated vibronic SOC by the second protocol enhanced the ISC rate by a factor of eight. Additionally, both protocols reveals different dominant ISC channels. According to the first protocol, the dominant ISC channel is $\mathrm{S}_1(\pi \rightarrow \pi^*) \rightsquigarrow \mathrm{T}_1(\pi \rightarrow \pi^*)$, in which the rate constant is roughly a factor of seven higher than the $\mathrm{S}_1(\pi \rightarrow \pi^*) \rightsquigarrow \mathrm{T}_3(\pi \rightarrow \pi^*)$ rate constant due to the contribution of vibronic SOC. However, the second protocol established that the dominant ISC channel is $\mathrm{S}_1(\pi \rightarrow \pi^*) \rightsquigarrow \mathrm{T}_3(\pi \rightarrow \pi^*)$ with an enhanced rate constant by a factor of five in comparison to the $\mathrm{S}_1(\pi \rightarrow \pi^*) \rightsquigarrow \mathrm{T}_1(\pi \rightarrow \pi^*)$ rate constant because of the low energy gap, vibronic SOC and favorable FC factors. Moreover, both protocols shows that the effect of the level of theory on the direct ($k_{ISC}^{FC}$) and vibronic ($k_{ISC}^{FCHT}$) SOC approach is small. It is worth mentioning that both protocols predict that ISC and fluorescence are

competitive processes.

To conclude, the calculated phosphorescence rate constant by the first ($k_P \approx 7.26 \times 10^{-1}\ s^{-1}$) and the second ($k_P \approx 1.25 \times 10\ s^{-1}$) protocol is very small. Therefore, the phosphorescence process $S_0 \leftarrow T_1$ is not feasible, which is in line with the experimentally observed behavior.

## 7 Dissemination of results

- Poster: "Estudio teórico de los process fotofísicos de la metilfeoforbida a". Hernán Rueda, Martha Daza, Markus Doerr. XIX Congreso colombiano de química. Octubre 2023.


- Paper: Bueno et al., 2025

## References

Adamo, C., & Barone, V. (1999). Toward reliable density functional methods without adjustable parameters: The PBE0 model. *J. Chem. Phys.*, *110*, 6158.

Aksel, M., Bozkurt-Girit, O., & Bilgin, M. D. (2020). Pheophorbide a-mediated sonodynamic, photodynamic and sonophotodynamic therapies against prostate cancer. *Photodiagnosis*

*and Photodynamic Therapy*, *31*, 101909. https://doi.org/10.1016/j.pdpdt.2020.101909

Bai, S., Mansour, R., Stojanovi, L., Toldo, J. M., & Barbatti, M. (2020). On the origin of the shift between vertical excitation and band maximum in molecular photoabsorption. *Journal of Molecular Modeling*, *26*(5), 107. https://doi.org/10.1007/s00894-020-04355-y

Baiardi, A., Bloino, J., & Barone, V. (2013). General time dependent approach to vibronic spectroscopy including franck–condon, herzberg-teller, and duschinsky effects. *J. Chem. Theory Comput.*, *9*, 4097.

Balashova, I., Tolbin, A., Tarakanov, P., Krot, A., Fedorova, K., Sergeeva, I., Trashin, S., De Wael, K., Pushkarev, V., Koifman, M., & Ponomarev, G. (2021). A covalently linked dyad based on zinc phthalocyanine and methylpheophorbide a: Synthetic and physicochemical study. *MACROHETEROCYCLES*, *14*(1), 40–50. https://doi.org/10.6060/mhc210338p

Bannwarth, C., Ehlert, S., & Grimme, S. (2019). GFN2-xTB—an accurate and broadly parametrized self-consistent tight-binding quantum chemical method with multipole electrostatics and density-dependent dispersion contributions [Publisher: American Chemical Society]. *Journal of Chemical Theory and Computation*, *15*(3), 1652–1671. https://doi.org/10.1021/acs.jctc.8b01176

Barone, V., & Cossi, M. (1998). Quantum calculation of molecular energies and energy gradients in solution by a conductor solvent model [Publisher: American Chemical Society]. *The Journal of Physical Chemistry A*, *102*(11), 1995–2001. https://doi.org/10.1021/jp9716997

Becke, A. D. (1993). Density-functional thermochemistry. III. the role of exact exchange. *J. Chem. Phys.*, *98*, 5648.

Berraud-Pache, R., Neese, F., Bistoni, G., & Izsák, R. (2019). Computational design of near-infrared fluorescent organic dyes using an accurate new wave function approach [Publisher: American Chemical Society]. *The Journal of Physical Chemistry Letters*, *10*(17), 4822–4828. https://doi.org/10.1021/acs.jpclett.9b02240

Bhandari, S., Sarkar, S., Schubert, A., Yamada, A., Payne, J., Ptaszek, M., Geva, E., & Dunietz, B. D. (2021). Intersystem crossing in tetrapyrrolic macrocycles. a first-principles analysis [_eprint: https://doi.org/10.1021/acs.jpcc.1c03696]. *The Journal of Physical Chemistry C*, *125*(24), 13493–13500. https://doi.org/10.1021/acs.jpcc.1c03696

Briat, B., Schooley, D. A., Records, R., Bunnenberg, E., & Djerassi, C. (1967). Magnetic circular dichroism studies. III. investigation of some optically active chlorins [Publisher: American Chemical Society]. *Journal of the American Chemical Society*, *89*(24), 6170–6177. https://doi.org/10.1021/ja01000a030

Bueno, H. R., Pinzón, J. R., Daza, M. C., & Doerr, M. (2025). A computational study on the photophysics of methylpheophorbide a [Publisher: The Royal Society of Chemistry]. *Physical Chemistry Chemical Physics*, *27*(19), 10376–10386. https://doi.org/10.1039/D4CP04829F

Casanova-Paez, M., & Goerigk, L. (2020). Assessing the tamm-dancoff approximation, singlet-singlet, and singlet-triplet excitations with the latest long-range corrected double-hybrid density functionals [Place: Melville Publisher: Amer Inst Physics WOS:000562801800002]. *Journal of Chemical Physics*, *153*(6), 064106. https://doi.org/10.1063/5.0018354

Casida, M., & Huix-Rotllant, M. (2012). Progress in time-dependent density-functional theory [_eprint: https://doi.org/10.1146/annurev-physchem-032511-143803]. *Annual Review of Physical Chemistry*, *63*(1), 287–323. https://doi.org/10.1146/annurev-physchem-032511-143803

Castro Júnior, J. G. M., & Rocha, W. R. (2022). Theoretical investigation of [ru(bpy)2(HAT)]2+ (HATă=ă1,4,5,8,9,12-hexaazatriphenylene; bpyă=ă2,2ÿ]'-bipyridine): Photophysics and reactions in excited state. *Spectrochimica Acta Part A: Molecular and Biomolecular Spectroscopy*, *270*, 120817. https://doi.org/10.1016/j.saa.2021.120817

Cerezo, J., Zúñiga, J., Requena, A., Ávila Ferrer, F. J., & Santoro, F. (2013). Harmonic models in cartesian and internal coordinates to simulate the absorption spectra of carotenoids at finite temperatures. *J. Chem. Theory Comput.*, *9*, 4947.

Chai, J.-D., & Head-Gordon, M. (2008). Systematic optimization of long-range corrected hybrid density functionals. *J. Chem. Phys.*, *128*, 084106.

de Souza, B., Farias, G., Neese, F., & Izsák, R. (2019). Predicting phosphorescence rates of light organic molecules using time-dependent density functional theory and the path integral approach to dynamics. *Journal of Chemical Theory and Computation*, *15*(3), 1896–1904. https://doi.org/10.1021/acs.jctc.8b00841

de Souza, B., Neese, F., & Izsák, R. (2018). On the theoretical prediction of fluorescence rates from first principles using the path integral approach. *The Journal of Chemical Physics*, *148*(3), 034104. https://doi.org/10.1063/1.5010895

Dierksen, M., & Grimme, S. (2004). Density functional calculations of the vibronic structure of electronic absorption spectra [Publisher: American Institute of Physics]. *The Journal of Chemical Physics*, *120*(8), 3544–3554. https://doi.org/10.1063/1.1642595

do Casal, M. T., Veys, K., Bousquet, M. H. E., Escudero, D., & Jacquemin, D. (2023). First-principles calculations of excited-state decay rate constants in organic fluorophores [Publisher: American Chemical Society]. *The Journal of Physical Chemistry A*, *127*(48), 10033–10053. https://doi.org/10.1021/acs.jpca.3c06191

Ekström, U., Visscher, L., Bast, R., Thorvaldsen, A. J., & Ruud, K. (2010). Arbitrary-order density functional response theory from automatic differentiation [Publisher: American Chemical Society]. *Journal of Chemical Theory and Computation*, *6*(7), 1971–1980. https://doi.org/10.1021/ct100117s

Franz, J. (2021). *Two triplet minima are better than one : Uncovering the relexation mechanism of photo-activated (re^{i}(CO)_{3}(bpy)(s-sbpy))^{+}* [Doctoral dissertation]. https://doi.org/10.25365/thesis.70901

Ghosh, S., Verma, P., Cramer, C. J., Gagliardi, L., & Truhlar, D. G. (2018). Combining wave function methods with density functional theory for excited states [Publisher: American Chemical Society]. *Chemical Reviews*, *118*(15), 7249–7292. https://doi.org/10.1021/acs.chemrev.8b00193

Gómez, S., Galván, I. F., Lindh, R., & González, L. (2020). Motivation and basic concepts [Section: 1 _eprint: https://onlinelibrary.wiley.com/doi/pdf/10.1002/9781119417774.ch1]. In *Quantum chemistry and dynamics of excited states* (pp. 1–12). John Wiley & Sons, Ltd. https://doi.org/https://doi.org/10.1002/9781119417774.ch1

Gouterman, M. (1959). Study of the effects of substitution on the absorption spectra of porphin [Publisher: American Institute of Physics]. *The Journal of Chemical Physics*, *30*(5), 1139–1161. https://doi.org/10.1063/1.1730148

Gouterman, M. (1961). Spectra of porphyrins. *Journal of Molecular Spectroscopy*, *6*, 138–163. https://doi.org/10.1016/0022-2852(61)90236-3

Gouterman, M., Wagnière, G. H., & Snyder, L. C. (1963). Spectra of porphyrins: Part II. four orbital model. *Journal of Molecular Spectroscopy*, *11*(1), 108–127. https://doi.org/10.1016/0022-2852(63)90011-0

Gunaydin, G., Gedik, M., & Ayan, S. (2021). Photodynamic therapy—current limitations and novel approaches. *Frontiers in Chemistry*, *9*, 1–25. https://doi.org/10.3389/fchem.2021.691697

Gutzler, R., Garg, M., Ast, C. R., Kuhnke, K., & Kern, K. (2021). Light–matter interaction at atomic scales. *Nature Reviews Physics*, *3*(6), 441–453. https://doi.org/10.1038/s42254-021-00306-5

Ha, J. Y., Yi, G., Bae, H. H., Go, Y. S., Kim, Y. J., Lee, K. M., Hong, C. O., & Kim, K. K. (2022). Isolation, identification, and apoptosis activity of the photosensitizer methyl pheophorbide a from perilla frutescens leaves. *Applied Biological Chemistry*, *65*(1), 52. https://doi.org/10.1186/s13765-022-00719-5

Hirata, S., & Head-Gordon, M. (1999). Time-dependent density functional theory within the tamm–dancoff approximation. *Chemical Physics Letters*, *314*(3), 291–299. https://doi.org/10.1016/S0009-2614(99)01149-5

Hohenberg, P., & Kohn, W. (1964). Inhomogeneous electron gas. *Physical Review*, *136*(3), B864–B871. https://doi.org/10.1103/PhysRev.136.B864

Isborn, C. M., Luehr, N., Ufimtsev, I. S., & Martínez, T. J. (2011). Excited-state electronic structure with configuration interaction singles and tamm–dancoff time-dependent density functional theory on graphical processing units [Publisher: American Chemical Society]. *Journal of Chemical Theory and Computation*, *7*(6), 1814–1823. https://doi.org/10.1021/ct200030k

Izsák, R., & Neese, F. (2011). An overlap fitted chain of spheres exchange method. *The Journal of Chemical Physics*, *135*(14), 144105. https://doi.org/10.1063/1.3646921

Jensen, F. (2017). *Introduction to computational chemistry* (Third). Wiley.

Jiang, X., Yang, R., Lei, X., Xue, S., Wang, Z., Zhang, J., Yan, L., Xu, Z., Chen, Z., Zou, P., & Wang, G. (2023). Design, synthesis, application and research progress of fluorescent probes. *Journal of Fluorescence*. https://doi.org/10.1007/s10895-023-03344-7

Jimenez-Aleman, G. H., Castro, V., Londaitsbehere, A., Gutierrez-Rodríguez, M., Garaigorta, U., Solano, R., & Gastaminza, P. (2021). SARS-CoV-2 fears green: The chlorophyll catabolite pheophorbide a is a potent antiviral. *Pharmaceuticals*, *14*(10). https://doi.org/10.3390/ph14101048

Kleinschmidt, M., Tatchen, J., & Marian, C. M. (2006). SPOCK.CI: A multireference spin-orbit configuration interaction method for large molecules. *The Journal of Chemical Physics*, *124*(12), 124101. https://doi.org/10.1063/1.2173246

Kohn, W., & Sham, L. J. (1965). Self-consistent equations including exchange and correlation effects. *Physical Review*, *140*(4), A1133–A1138. https://doi.org/10.1103/PhysRev.140.A1133

Liu, J., Chen, W., Zheng, C., Hu, F., Zhai, J., Bai, Q., Sun, N., Qian, G., Zhang, Y., Dong, K., & Lu, T. (2022). Recent molecular design strategies for efficient photodynamic therapy and its synergistic therapy based on AIE photosensitizers. *European Journal of Medicinal Chemistry*, *244*, 114843. https://doi.org/10.1016/j.ejmech.2022.114843

Luo, L., Xiao, Z., Chen, B., Cai, F., Fang, L., Lin, L., & Luan, T. (2018). Natural porphyrins accelerating the phototransformation of benzo[a]pyrene in water. *Environmental Science & Technology*, *52*(6), 3634–3641. https://doi.org/10.1021/acs.est.7b05854

Marian, C. M. (2021). Understanding and controlling intersystem crossing in molecules [Publisher: Annual Reviews]. *Annual Review of Physical Chemistry*, *72*(1), 617–640. https://doi.org/10.1146/annurev-physchem-061020-053433

Martynov, A. G., Mack, J., May, A. K., Nyokong, T., Gorbunova, Y. G., & Tsivadze, A. Y. (2019). Methodological survey of simplified TD-DFT methods for fast and accurate interpretation of UV–vis–NIR spectra of phthalocyanines [Publisher: American Chemical Society]. *ACS Omega*, *4*(4), 7265–7284. https://doi.org/10.1021/acsomega.8b03500

Meng, Z., Xue, H., Wang, T., Chen, B., Dong, X., Yang, L., Dai, J., Lou, X., & Xia, F. (2022). Aggregation-induced emission photosensitizer-based photodynamic therapy in cancer: From chemical to clinical. *Journal of Nanobiotechnology*, *20*(1), 344. https://doi.org/10.1186/s12951-022-01553-z

Miranda, N., Gerola, A. P., Novello, C. R., Ueda-Nakamura, T., de Oliveira Silva, S., Dias-Filho, B. P., Hioka, N., de Mello, J. C. P., & Nakamura, C. V. (2017). Pheophorbide a, a compound isolated from the leaves of arrabidaea chica, induces photodynamic inactivation of trypanosoma cruzi. *Photodiagnosis and Photodynamic Therapy*, *19*, 256–265. https://doi.org/10.1016/j.pdpdt.2017.05.004

Miranda, N., Volpato, H., da Silva Rodrigues, J. H., Caetano, W., Ueda-Nakamura, T., de Oliveira Silva, S., & Nakamura, C. V. (2017). The photodynamic action of pheophorbide a induces cell death through oxidative stress in leishmania amazonensis. *Journal of Photochemistry and Photobiology B: Biology*, *174*, 342–354. https://doi.org/10.1016/j.jphotobiol.2017.08.016

Neese, F. (2009). Prediction of molecular properties and molecular spectroscopy with density functional theory: From fundamental theory to exchange-coupling. *Coordination Chemistry Reviews*, *253*, 526–563. https://doi.org/Densityfunctionaltheory

Neese, F. (2005). Efficient and accurate approximations to the molecular spin-orbit coupling operator and their use in molecular g-tensor calculations. *The Journal of Chemical Physics*, *122*(3), 034107. https://doi.org/10.1063/1.1829047

Neese, F. (2022). Software update: The ORCA program system—version 5.0. *WIREs Computational Molecular Science*, *12*(5), e1606. https://doi.org/10.1002/wcms.1606

Neese, F., Wennmohs, F., Hansen, A., & Becker, U. (2009). Efficient, approximate and parallel hartree–fock and hybrid DFT calculations. a 'chain-of-spheres' algorithm for the hartree–fock exchange. *Chemical Physics*, *356*(1), 98–109. https://doi.org/10.1016/j.chemphys.2008.10.036

Palma, M., Cárdenas-Jirón, G. I., & Menéndez Rodríguez, M. I. (2008). Effect of chlorin structure on theoretical electronic absorption spectra and on the energy released by porphyrin-based photosensitizers [Publisher: American Chemical Society]. *The Journal of Physical Chemistry A*, *112*(51), 13574–13583. https://doi.org/10.1021/jp804350n

Pang, E., Zhao, S., Wang, B., Niu, G., Song, X., & Lan, M. (2022). Strategies to construct efficient singlet oxygen-generating photosensitizers. *Coordination Chemistry Reviews*, *472*, 214780. https://doi.org/10.1016/j.ccr.2022.214780

Parusel, A. B. J., & Grimme, S. (2000). A theoretical study of the excited states of chlorophyll a and pheophytin a [Publisher: American Chemical Society]. *The Journal of Physical Chemistry B*, *104*(22), 5395–5398. https://doi.org/10.1021/jp000346w

Parusel, A. B. J., & Grimme, S. (2001). DFT/MRCI calculations on the excited states of porphyrin, hydroporphyrins, tetrazaporphyrins and metalloporphyrins. *Journal of Porphyrins and Phthalocyanines*, *5*(3), 225–232. https://doi.org/10.1002/jpp.310

Peach, M. J. G., Williamson, M. J., & Tozer, D. J. (2011). Influence of triplet instabilities in TDDFT [Publisher: American Chemical Society]. *Journal of Chemical Theory and Computation*, *7*(11), 3578–3585. https://doi.org/10.1021/ct200651r

Penfold, T. J., Gindensperger, E., Daniel, C., & Marian, C. M. (2018). Spin-vibronic mechanism for intersystem crossing [Publisher: American Chemical Society]. *Chemical Reviews*, *118*(15), 6975–7025. https://doi.org/10.1021/acs.chemrev.7b00617

Perun, S., Tatchen, J., & Marian, C. M. (2008). Singlet and triplet excited states and intersystem crossing in free-base porphyrin: TDDFT and DFT/MRCI study [Publisher: John Wiley & Sons, Ltd]. *ChemPhysChem*, *9*(2), 282–292. https://doi.org/10.1002/cphc.200700509

Pracht, P., Bohle, F., & Grimme, S. (2020). Automated exploration of the low-energy chemical space with fast quantum chemical methods [Publisher: The Royal Society of Chemistry]. *Physical Chemistry Chemical Physics*. https://doi.org/10.1039/C9CP06869D

Reimers, J. R., Cai, Z.-L., Kobayashi, R., Rätsep, M., Freiberg, A., & Krausz, E. (2013). Assignment of the q-bands of the chlorophylls: Coherence loss via qx  qy mixing. *Scientific Reports*, *3*(1), 2761. https://doi.org/10.1038/srep02761

Reimers, J. R., Rätsep, M., Linnanto, J., & Freiberg, A. (2022). Chlorophyll spectroscopy: Conceptual basis, modern high-resolution approaches, and current challenges. *Proceedings of the Estonian Academy of Sciences*, *71*(2), 127–164. https://doi.org/10.3176/proc.2022.2.04

Reiter, S., Bäuml, L., Hauer, J., & de Vivie-Riedle, R. (2022). Q-band relaxation in chlorophyll: New insights from multireference quantum dynamics [Publisher: The Royal Society of Chemistry]. *Physical Chemistry Chemical Physics*, *24*(44), 27212–27223. https://doi.org/10.1039/D2CP02914F

Rocca, D., Bai, Z., Li, R.-C., & Galli, G. (2012). A block variational procedure for the iterative diagonalization of non-hermitian random-phase approximation matrices. *The Journal of Chemical Physics*, *136*(3), 034111. https://doi.org/10.1063/1.3677667

Rodriguez Prada, K. I. (2018). *SINTESIS DE COMPUESTOS FOTOSENSIBILIZADORES DERIVADOS DE CLOROFILA CON POTENCIAL ACTIVIDAD BIOLOGICA [recurso electronico]* [Doctoral dissertation, Universidad Industrial de Santander]. https://uids-primo.hosted.exlibrisgroup.com/permalink/f/18autd3/uids_bucaramanga184702

Runge, E., & Gross, E. K. U. (1984). Density-functional theory for time-dependent systems. *Physical Review Letters*, *52*(12), 997–1000. https://doi.org/10.1103/PhysRevLett.52.997

Ryazanova, O. A., Zozulya, V. N., Voloshin, I. M., Dubey, L., Ilchenko, M. M., Dubey, I. Y., & Karachevtsev, V. A. (2020). Pheophorbide-phenazinium conjugate as a fluorescent light-up probe for g-quadruplex structure [Place: Amsterdam Publisher: Elsevier]. *Journal of Molecular Structure*, *1214*, 128218. https://doi.org/10.1016/j.molstruc.2020.128218

Saide, A., Lauritano, C., & Ianora, A. (2020). Pheophorbide a: State of the art [Place: Basel Publisher: Mdpi WOS:000541031900050]. *Marine Drugs*, *18*(5), 257. https://doi.org/10.3390/md18050257

Shrestha, K., Virgil, K., & Jakubikova, E. (2016). Electronic absorption spectra of tetrapyrrole-based pigments via TD-DFT: A reduced orbital space study [Publisher: American Chemical Society]. *The Journal of Physical Chemistry A*, *120*(29), 5816–5825. https://doi.org/10.1021/acs.jpca.6b04797

Sirohiwal, A., Berraud-Pache, R., Neese, F., Izsak, R., & Pantazis, D. A. (2020). Accurate computation of the absorption spectrum of chlorophyll alpha with pair natural orbital coupled cluster methods [Place: Washington Publisher: Amer Chemical Soc WOS:000580559100003]. *Journal of Physical Chemistry B*, *124*(40), 8761–8771. https://doi.org/10.1021/acs.jpcb.0c05761

Song, Y., Schubert, A., Maret, E., Burdick, R. K., Dunietz, B. D., Geva, E., & Ogilvie, J. P. (2019). Vibronic structure of photosynthetic pigments probed by polarized two-dimensional electronic spectroscopy and ab initio calculations [Publisher: The Royal Society of Chemistry]. *Chemical Science*, *10*(35), 8143–8153. https://doi.org/10.1039/C9SC02329A

Stanke, M. (2016). Adiabatic, born-oppenheimer, and non-adiabatic approaches. In J. Leszczynski (Ed.), *Handbook of computational chemistry* (pp. 1–51). Springer Netherlands. https://doi.org/10.1007/978-94-007-6169-8_41-1

Stratmann, R. E., Scuseria, G. E., & Frisch, M. J. (1998). An efficient implementation of time-dependent density-functional theory for the calculation of excitation energies of large molecules. *The Journal of Chemical Physics*, *109*(19), 8218–8224. https://doi.org/10.1063/1.477483

Suzuki, K., & Okamoto, R. (1984). Perturbation theory for quasidegenerate system in quantum mechanics. *Progress of Theoretical Physics*, *72*(3), 534–548. https://doi.org/10.1143/PTP.72.534

Szurko, A., Rams, M., Sochanik, A., Siero-Stotny, K., Kozielec, A. M., Montforts, F.-P., Wrzalik, R., & Ratuszna, A. (2009). Spectroscopic and biological studies of a novel synthetic chlorin derivative with prospects for use in PDT. *Bioorganic & Medicinal Chemistry*, *17*(24), 8197–8205. https://doi.org/10.1016/j.bmc.2009.10.029

Talotta, F. (2018). *Excited-state mechanisms and dynamics of the ruthenium nitrosyl complex trans-[RuCl(NO)(py)4]2+* [Doctoral dissertation]. https://doi.org/10.25365/thesis.55667

Turro, N. J., Ramamurthy, V., & Scaiano, J. C. (2009). *Principles of molecular photochemistry: An introduction*. University Science Books. https://books.google.com.co/books?id=NC5uUlqhQCYC

Wang, K.-K., Li, J., Kim, B.-J., Lee, J.-H., Shin, H.-W., Ko, S.-H., Lee, W.-Y., Lee, C.-H., Jung, S. H., & Kim, Y.-R. (2014). Photophysical properties of pheophorbide-a derivatives and their photodynamic therapeutic effects on a tumor cell line *In Vitro*. *International Journal of Photoenergy*, *2014*, 793723, 1–7. https://doi.org/10.1155/2014/793723

Weigend, F. (2006). Accurate coulomb-fitting basis sets for h to rn [Publisher: The Royal Society of Chemistry]. *Physical Chemistry Chemical Physics*, *8*(9), 1057–1065. https://doi.org/10.1039/B515623H

Weigend, F., & Ahlrichs, R. (2005). Balanced basis sets of split valence, triple zeta valence and quadruple zeta valence quality for h to rn: Design and assessment of accuracy [Publisher: The Royal Society of Chemistry]. *Physical Chemistry Chemical Physics*, *7*(18), 3297–3305. https://doi.org/10.1039/B508541A

Yanai, T., Tew, D. P., & Handy, N. C. (2004). A new hybrid exchange-correlation functional using the coulomb-attenuating method (CAM-b3lyp). *Chem. Phys. Lett.*, *393*, 51.

Yasuda, K., Ganguly, S., & Schuetz, E. G. (2018). Pheophorbide a: Fluorescent bcrp substrate to measure oral drug-drug interactions in real-time in vivo [Place: Bethesda Publisher: Amer Soc Pharmacology Experimental Therapeutics WOS:000452484200029]. *Drug Metabolism and Disposition*, *46*(11), 1725–1733. https://doi.org/10.1124/dmd.118.083584

Yin, S., Dahlbom, M. G., Canfield, P. J., Hush, N. S., Kobayashi, R., & Reimers, J. R. (2007). Assignment of the qy absorption spectrum of photosystem-i from thermosynechococcus elongatus based on CAM-b3lyp calculations at the PW91-optimized protein structure [Publisher: American Chemical Society]. *The Journal of Physical Chemistry B*, *111*(33), 9923–9930. https://doi.org/10.1021/jp070030p

Yoshinaga, M., & Rocha, W. R. (2021). Theoretical investigation of the 4,5-dibromorodamine methyl ester (TH9402) photosensitizer used in photodynamic therapy: Photophysics, re-

actions in the excited state, and interactions with DNA [Publisher: American Chemical Society]. *The Journal of Physical Chemistry B*, *125*(31), 8932–8943. https://doi.org/10.1021/acs.jpcb.1c05463

Zhang, A., Kwan, L., & Stillman, M. J. (2017). The spectroscopic impact of interactions with the four gouterman orbitals from peripheral decoration of porphyrins with simple electron withdrawing and donating groups [Publisher: The Royal Society of Chemistry]. *Organic & Biomolecular Chemistry*, *15*(43), 9081–9094. https://doi.org/10.1039/C7OB01960B

Zhang, A., & Stillman, M. J. (2018). Exploring function activated chlorins using MCD spectroscopy and DFT methods: Design of a chlorin with a remarkably intense, red q band [Place: Cambridge Publisher: Royal Soc Chemistry WOS:000431825300015]. *Physical Chemistry Chemical Physics*, *20*(18), 12470–12482. https://doi.org/10.1039/c8cp01010b

Zobel, J. P., & González, L. (2019). Nonadiabatic dynamics simulation predict intersystem crossing in nitroaromatic molecules on a picosecond time scale [Publisher: John Wiley & Sons, Ltd]. *ChemPhotoChem*, *3*(9), 833–845. https://doi.org/10.1002/cptc.201900108

# Appendix

## Appendix A: Choice of the computational protocol

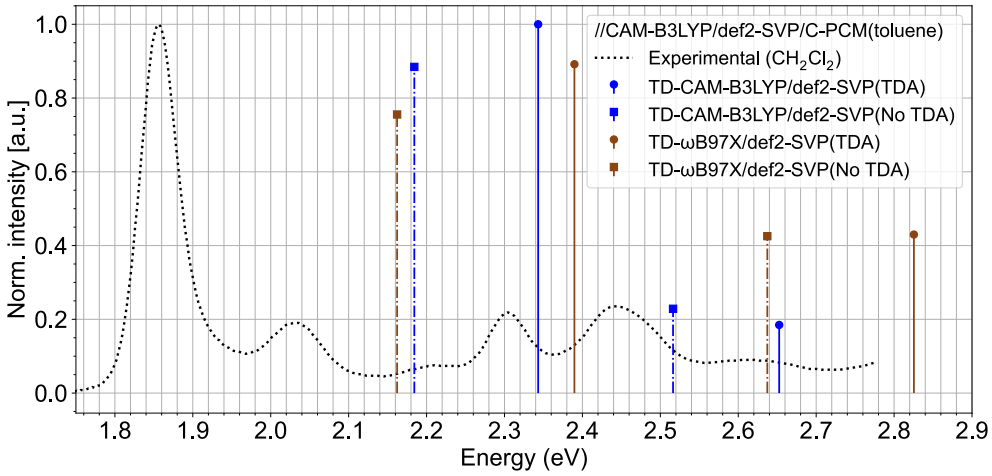


**Figure 26.** Effect of the density functional and the TDA approximation on the vertical excitation energies (eV) associated with the first ($S_1$) and second ($S_2$) singlet excited states computed at the ground state geometry. All calculations were performed using the CAM-B3LYP/def2-SVP optimized structure.

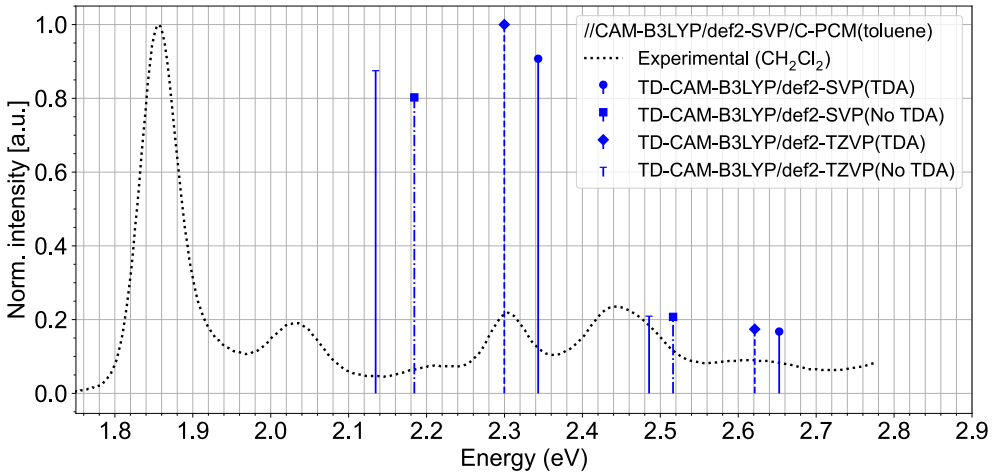


**Figure 27.** Effect of the basis set and the TDA approximation on the vertical excitation energies (eV) associated with the first ($S_1$) and second ($S_2$) singlet excited states computed at the ground state geometry. All calculations were performed using the CAM-B3LYP/def2-SVP optimized structure.

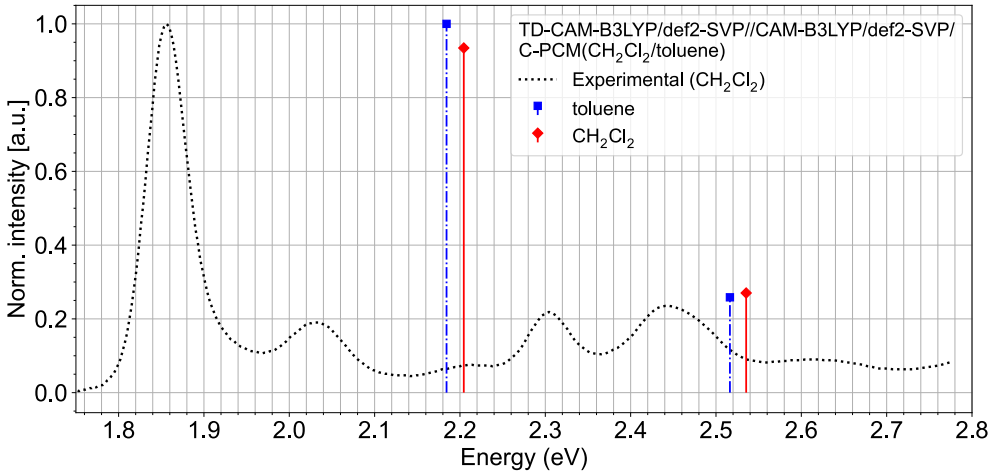


**Figure 28.** Effect of the solvent and full TD-DFT on the vertical excitation energies (eV) associated with the first ($S_1$) and second ($S_2$) singlet excited states computed at the ground state geometry.

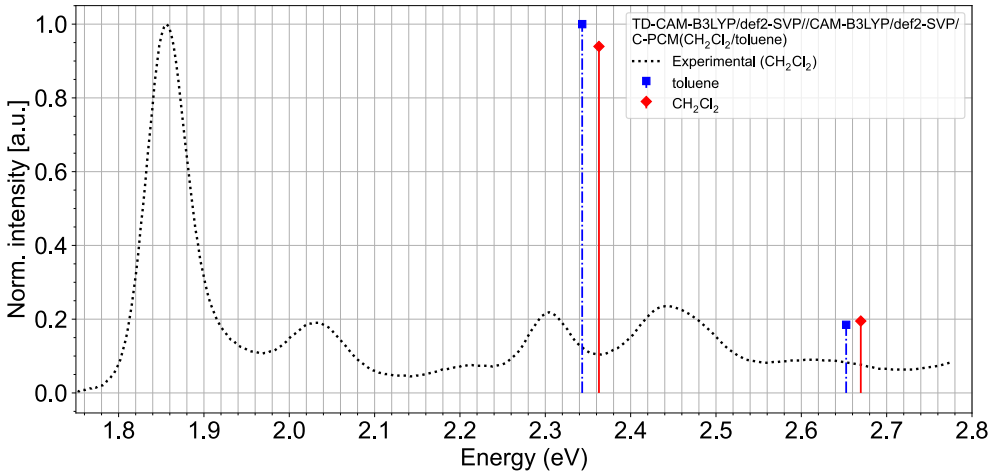


**Figure 29.** Effect of the solvent and TDA approximation on the vertical excitation energies (eV) associated with the first ($S_1$) and second ($S_2$) singlet excited states computed at the ground state geometry.

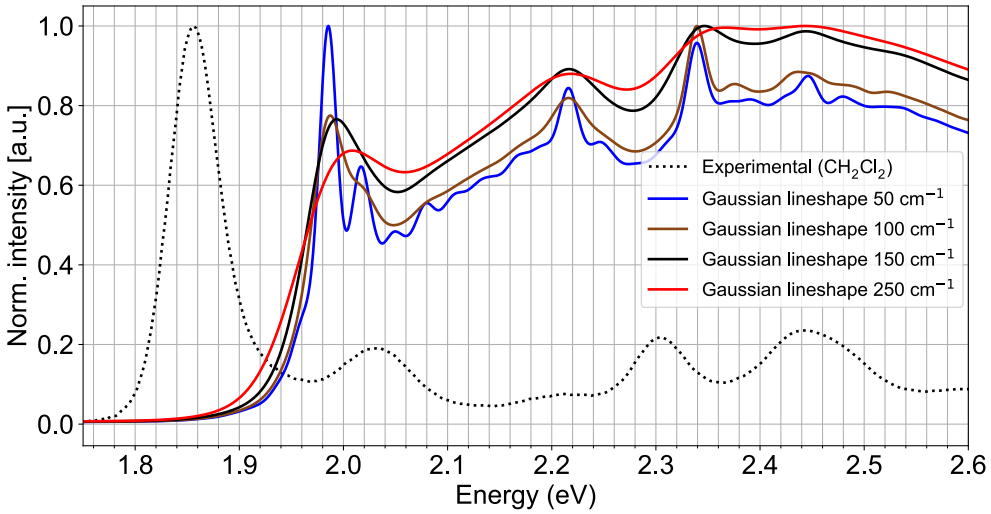


**Figure 30.** Effect of the Gaussian bandwidth on the Q-band region of the absorption spectrum employing the adiabatic Hessian model, and including Franck-Condon and Herzberg-Teller (FCHT) terms at 298.15 K. Vibrational modes below 100 $cm^{-1}$ were discarded.

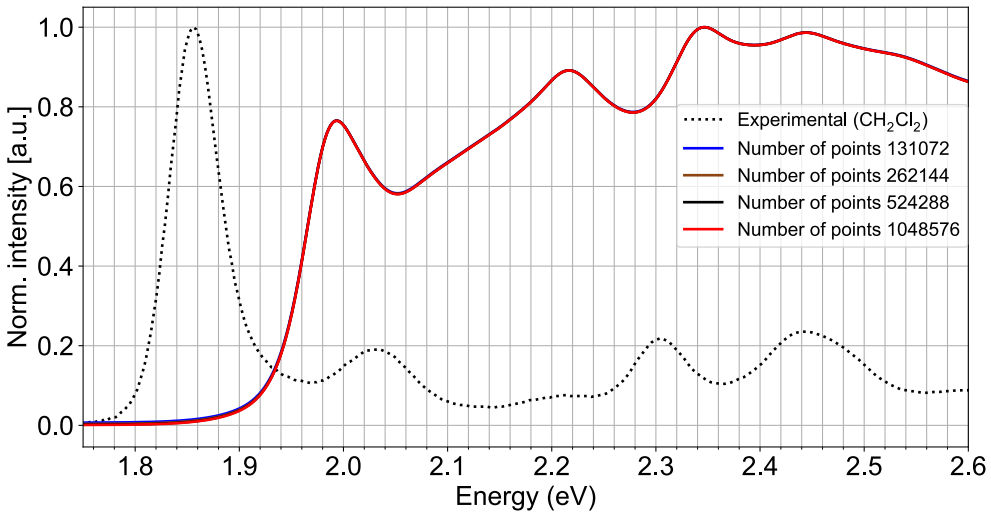


**Figure 31.** Effect of the number of points on the Q-band region of the absorption spectrum employing the adiabatic Hessian model, and including Franck-Condon and Herzberg-Teller (FCHT) terms at 298.15 K. The Gaussian bandwidth was set to 150 $cm^{-1}$ and vibrational modes below 100 $cm^{-1}$ were discarded.

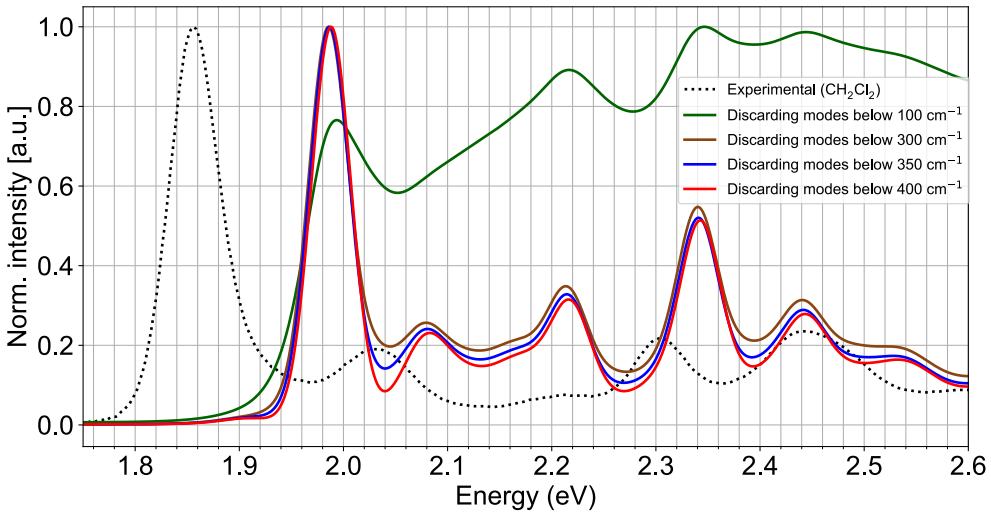


**Figure 32.** Effect of discarding vibrational modes employing the adiabatic Hessian model, and including Franck-Condon and Herzberg-Teller (FCHT) terms at 298.15 K. The Gaussian bandwidth was set to 150 $cm^{-1}$.

## Appendix B: Supporting Information for the First Protocol

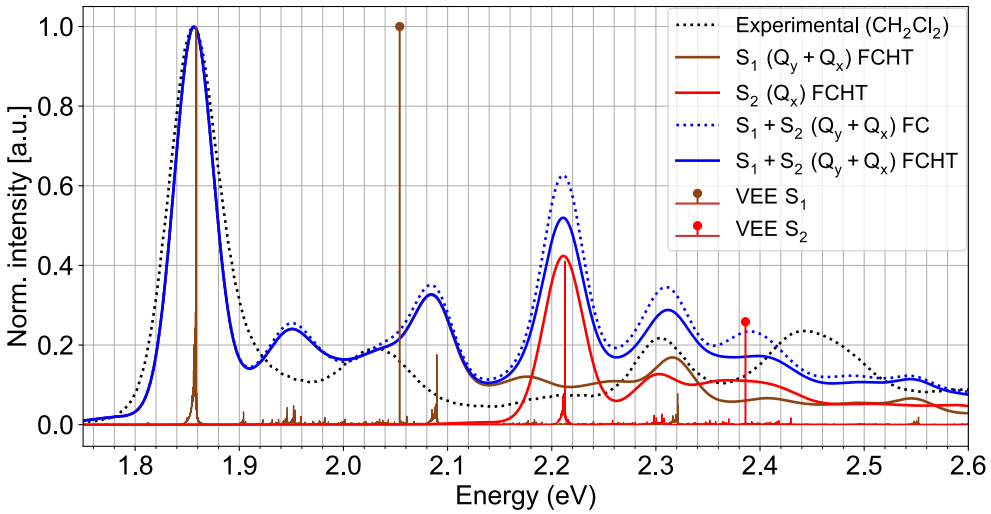


**Figure 33.** Computed vibronic structure and stick spectrum of the Q-band employing the adiabatic Hessian approximation, Franck-Condon and Franck-Condon-Herzberg-Teller contributions at 298.15K. The Gaussian linewidth was set to 150 $cm^{-1}$ and vibrational modes below 350 $cm^{-1}$ were removed. The calculated spectra and VEEs were shifted by 0.13 eV to align with the experimental band maximum.

**Table 12.** *Adiabatic energy differences between the lowest singlet excited state and the ground state computed at different levels of theory using the CAM-B3LYP/def2-SVP optimized structure.*

| Level of theory | $\Delta E_{S1\text{-}S0}$ (eV) | $\Delta E_{S2\text{-}S0}$ (eV) |
|---|---|---|
| CAM-B3LYP/def2-SVP | 2.01 | 2.38 |
| CAM-B3LYP/def2-TZVP | 1.99 | 2.38 |
| $\omega$B97X/def2-SVP | 1.89 | 2.42 |
| $\omega$B97X/def2-TZVP | 1.86 | 2.42 |
| PBE0/def2-SVP | 2.07 | 2.28 |
| PBE0/def2-TZVP | 2.05 | 2.28 |

**Table 13.** *TD-DFT spectroscopic parameters for the Q band calculated in toluene with different density functionals and bases and using the CAM-B3LYP/def2-SVP optimized structure.*

| Experimental (eV) | Functional | def2-SVP | | | def2-TZVP | | |
|---|---|---|---|---|---|---|---|
| | | VEE (eV) | $\lambda$ (nm) | $f_{osc.}$ | VEE (eV) | $\lambda$ (nm) | $f_{osc.}$ |
| 1.85 | CAM-B3LYP | 2.184 | 567.6 | 0.2921 | 2.135 | 580.7 | 0.3184 |
| | $\omega$B97X | 2.162 | 573.4 | 0.2494 | 2.113 | 586.7 | 0.2692 |
| | PBE0 | 2.195 | 565.0 | 0.3115 | 2.149 | 577.0 | 0.3401 |
| 2.31 | CAM-B3LYP | 2.516 | 492.7 | 0.0755 | 2.486 | 498.8 | 0.0762 |
| | $\omega$B97X | 2.637 | 470.1 | 0.1405 | 2.611 | 474.8 | 0.1524 |
| | PBE0 | 2.413 | 513.8 | 0.0612 | 2.385 | 519.8 | 0.0582 |

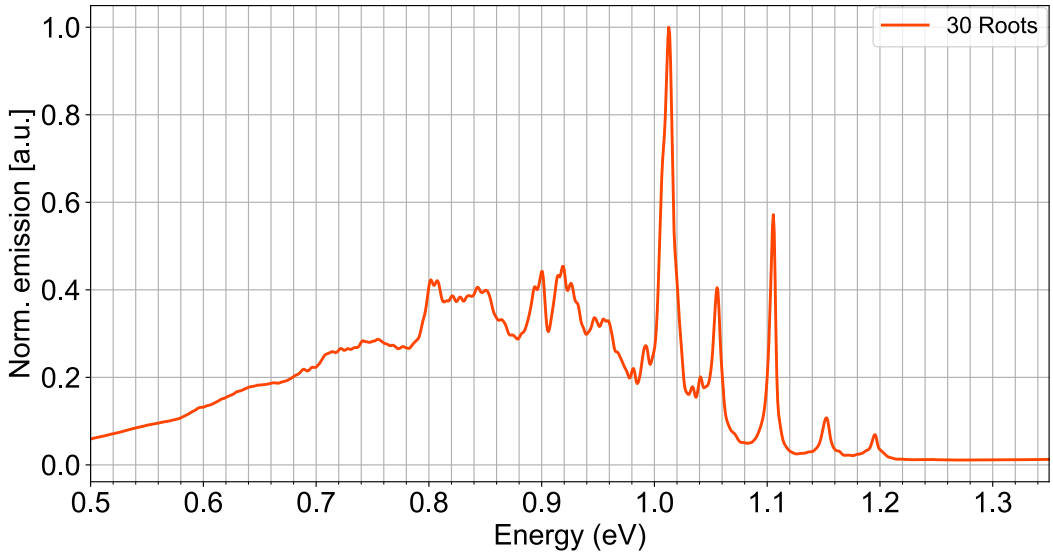


**Figure 34.** Computed phosphorescence spectrum employing the adiabatic Hessian approximation, Franck-Condon (FC) and Franck-Condon-Herzberg-Teller (FCHT) contributions at 298.15K. The Gaussian linewidth was set to 10 $cm^{-1}$ and vibrational normal modes below 100 $cm^{-1}$ were discarded.

**Table 14.** *Adiabatic energy difference between the lowest singlet excited state and the first, second and third triplet state computed at different levels of theory using the CAM-B3LYP/def2-SVP optimized structure.*

| **Level of theory** | **$\Delta E_{S1\text{-}T1}$ (eV)** | **$\Delta E_{S1\text{-}T2}$ (eV)** | **$\Delta E_{S1\text{-}T3}$ (eV)** |
|---|---|---|---|
| CAM-B3LYP/def2-SVP | 0.85 | 0.88 | 0.065 |
| CAM-B3LYP/def2-TZVP | 0.83 | 0.91 | 0.031 |
| $\omega$B97X/def2-SVP | 0.91 | 0.13 | -0.12 |
| $\omega$B97X/def2-TZVP | 0.91 | 0.027 | -0.17 |
| PBE0/def2-SVP | 1.17 | 0.68 | 0.071 |
| PBE0/def2-TZVP | 1.12 | 0.69 | 0.049 |

**Table 15.** *Effect of the Gaussian linewidth on the ISC rate constants $k_{ISC}$ ($s^{-1}$) at room temperature.*

| Channel | Parameters | | Results |
|---|---|---|---|
| | $E_{ST}$ (eV) | Gaussian linewidth ($cm^{-1}$) | $k_{ISC}^{FCHT}$ ($s^{-1}$) |
| $S_1 \rightsquigarrow T_1$ | 0.85 | 0.1 | 3.76 x $10^6$ |
| $S_1 \rightsquigarrow T_1$ | 0.85 | 1.0 | 5.94 x $10^5$ |
| $S_1 \rightsquigarrow T_1$ | 0.85 | 10.0 | 7.39 x $10^3$ |
| $S_1 \rightsquigarrow T_1$ | 0.85 | 100.0 | 7.62 x $10^3$ |
| $S_1 \rightsquigarrow T_2$ | 0.88 | 0.1 | 1.55 x $10^6$ |
| $S_1 \rightsquigarrow T_2$ | 0.88 | 1.0 | 9.11 x $10^5$ |
| $S_1 \rightsquigarrow T_2$ | 0.88 | 10.0 | 9.12 x $10^5$ |
| $S_1 \rightsquigarrow T_2$ | 0.88 | 100.0 | 9.08 x $10^5$ |
| $S_1 \rightsquigarrow T_3$ | 0.065 | 0.1 | 3.03 x $10^6$ |
| $S_1 \rightsquigarrow T_3$ | 0.065 | 1.0 | -6.46 x $10^4$ |
| $S_1 \rightsquigarrow T_3$ | 0.065 | 10.0 | 9.93 x $10^2$ |
| $S_1 \rightsquigarrow T_3$ | 0.065 | 100.0 | 9.93 x $10^2$ |

**Table 16.** *Harmonic frequencies $v_i$ ($cm^{-1}$) and triplet-sublevels-averaged ∂SOCMEs ($cm^{-1}$) with respect to the corresponding vibrational modes at the equilibrium geometry of $T_1$, $T_2$ and $T_3$ states.*

| Mode | $v_i@T_1$ | $S_1$-$T_1$ | Mode | $v_i@T_2$ | $S_1$-$T_2$ | Mode | $v_i@T_2$ | $S_1$-$T_3$ |
|---|---|---|---|---|---|---|---|---|
| 1 | 101.7 | 0.000 | 1 | 105.4 | 0.000 | 1 | 105.0 | 0.000 |
| 2 | 107.8 | 0.000 | 2 | 118.5 | 0.000 | 2 | 116.7 | 0.000 |
| 3 | 119.0 | 0.000 | 3 | 123.2 | 0.000 | 3 | 118.1 | 0.000 |
| 4 | 122.9 | 0.000 | 4 | 130.6 | 0.000 | 4 | 122.9 | 0.000 |
| 5 | 130.2 | 0.000 | 5 | 133.4 | 0.000 | 5 | 132.4 | 0.000 |
| 6 | 135.8 | 0.000 | 6 | 138.3 | 0.000 | 6 | 134.2 | 0.000 |
| 7 | 137.1 | 0.000 | 7 | 142.0 | 0.000 | 7 | 137.7 | 0.000 |
| 8 | 144.0 | 0.000 | 8 | 147.4 | 0.000 | 8 | 141.5 | 0.000 |

Continued on next page

**Table 16 continued from previous page**

| Mode | $\nu_i@T_1$ | $S_1$-$T_1$ | Mode | $\nu_i@T_2$ | $S_1$-$T_2$ | Mode | $\nu_i@T_2$ | $S_1$-$T_3$ |
|---|---|---|---|---|---|---|---|---|
| 9 | 147.8 | 0.000 | 9 | 151.5 | 0.000 | 9 | 147.4 | 0.000 |
| 10 | 157.4 | 0.000 | 10 | 158.3 | 0.000 | 10 | 158.6 | 0.000 |
| 11 | 165.5 | 0.000 | 11 | 162.8 | 0.000 | 11 | 163.4 | 0.000 |
| 12 | 173.7 | 0.000 | 12 | 173.1 | 0.000 | 12 | 173.6 | 0.000 |
| 13 | 187.1 | 0.000 | 13 | 182.0 | 0.000 | 13 | 180.0 | 0.000 |
| 14 | 194.7 | 0.000 | 14 | 186.3 | 0.000 | 14 | 191.0 | 0.000 |
| 15 | 196.1 | 0.000 | 15 | 195.5 | 0.000 | 15 | 194.5 | 0.000 |
| 16 | 207.2 | 0.000 | 16 | 196.3 | 0.000 | 16 | 196.3 | 0.000 |
| 17 | 214.0 | 0.000 | 17 | 210.4 | 0.000 | 17 | 214.3 | 0.000 |
| 18 | 216.4 | 0.000 | 18 | 214.8 | 0.000 | 18 | 217.3 | 0.000 |
| 19 | 222.1 | 0.000 | 19 | 221.1 | 0.000 | 19 | 222.9 | 0.000 |
| 20 | 233.5 | 0.000 | 20 | 232.8 | 0.000 | 20 | 236.1 | 0.000 |
| 21 | 238.8 | 0.000 | 21 | 235.9 | 0.000 | 21 | 239.9 | 0.000 |
| 22 | 246.6 | 0.000 | 22 | 240.3 | 0.000 | 22 | 243.6 | 0.000 |
| 23 | 251.3 | 0.000 | 23 | 252.9 | 0.000 | 23 | 248.8 | 0.000 |
| 24 | 254.6 | 0.000 | 24 | 256.3 | 0.000 | 24 | 256.5 | 0.000 |
| 25 | 262.0 | 0.000 | 25 | 264.5 | 0.000 | 25 | 258.4 | 0.000 |
| 26 | 265.4 | 0.001 | 26 | 269.6 | 0.000 | 26 | 265.7 | 0.000 |
| 27 | 270.8 | 0.000 | 27 | 270.4 | 0.000 | 27 | 267.9 | 0.001 |
| 28 | 278.2 | 0.000 | 28 | 280.0 | 0.000 | 28 | 281.4 | 0.000 |
| 29 | 284.6 | 0.000 | 29 | 287.0 | 0.000 | 29 | 286.1 | 0.000 |

Continued on next page

**Table 16 continued from previous page**

| Mode | $\nu_i@T_1$ | $S_1$-$T_1$ | Mode | $\nu_i@T_2$ | $S_1$-$T_2$ | Mode | $\nu_i@T_2$ | $S_1$-$T_3$ |
|---|---|---|---|---|---|---|---|---|
| 30 | 290.1 | 0.000 | 30 | 293.9 | 0.000 | 30 | 291.3 | 0.000 |
| 31 | 295.0 | 0.000 | 31 | 297.9 | 0.000 | 31 | 298.6 | 0.000 |
| 32 | 318.1 | 0.000 | 32 | 317.3 | 0.000 | 32 | 312.8 | 0.000 |
| 33 | 320.9 | 0.001 | 33 | 320.5 | 0.000 | 33 | 322.7 | 0.000 |
| 34 | 344.5 | 0.000 | 34 | 346.1 | 0.000 | 34 | 346.0 | 0.000 |
| 35 | 361.0 | 0.000 | 35 | 362.9 | 0.000 | 35 | 356.5 | 0.001 |
| 36 | 366.3 | 0.000 | 36 | 367.4 | 0.000 | 36 | 367.6 | 0.001 |
| 37 | 383.7 | 0.001 | 37 | 379.1 | 0.000 | 37 | 372.0 | 0.001 |
| 38 | 384.5 | 0.001 | 38 | 384.0 | 0.000 | 38 | 392.4 | 0.001 |
| 39 | 406.5 | 0.000 | 39 | 412.7 | 0.000 | 39 | 415.4 | 0.000 |
| 40 | 429.4 | 0.001 | 40 | 429.6 | 0.000 | 40 | 428.1 | 0.000 |
| 41 | 445.8 | 0.001 | 41 | 444.4 | 0.000 | 41 | 444.2 | 0.001 |
| 42 | 459.6 | 0.001 | 42 | 461.5 | 0.000 | 42 | 459.3 | 0.000 |
| 43 | 468.0 | 0.002 | 43 | 466.2 | 0.000 | 43 | 470.6 | 0.001 |
| 44 | 479.1 | 0.001 | 44 | 476.6 | 0.000 | 44 | 484.0 | 0.002 |
| 45 | 491.5 | 0.002 | 45 | 488.9 | 0.000 | 45 | 489.1 | 0.002 |
| 46 | 521.4 | 0.003 | 46 | 522.3 | 0.000 | 46 | 508.8 | 0.003 |
| 47 | 535.7 | 0.003 | 47 | 535.3 | 0.001 | 47 | 531.4 | 0.001 |
| 48 | 548.9 | 0.002 | 48 | 555.1 | 0.000 | 48 | 544.7 | 0.001 |
| 49 | 573.5 | 0.000 | 49 | 575.7 | 0.000 | 49 | 551.8 | 0.001 |
| 50 | 592.0 | 0.001 | 50 | 592.2 | 0.000 | 50 | 571.1 | 0.000 |

Continued on next page

**Table 16 continued from previous page**

| Mode | $v_i@T_1$ | $S_1$-$T_1$ | Mode | $v_i@T_2$ | $S_1$-$T_2$ | Mode | $v_i@T_2$ | $S_1$-$T_3$ |
|---|---|---|---|---|---|---|---|---|
| 51 | 603.4 | 0.001 | 51 | 611.3 | 0.000 | 51 | 591.8 | 0.001 |
| 52 | 617.9 | 0.001 | 52 | 620.5 | 0.000 | 52 | 610.8 | 0.000 |
| 53 | 620.9 | 0.001 | 53 | 634.2 | 0.000 | 53 | 616.1 | 0.001 |
| 54 | 640.2 | 0.001 | 54 | 643.7 | 0.000 | 54 | 637.8 | 0.001 |
| 55 | 651.1 | 0.002 | 55 | 655.5 | 0.000 | 55 | 654.9 | 0.001 |
| 56 | 659.6 | 0.001 | 56 | 668.9 | 0.000 | 56 | 662.6 | 0.001 |
| 57 | 667.5 | 0.001 | 57 | 683.6 | 0.000 | 57 | 671.2 | 0.001 |
| 58 | 684.2 | 0.001 | 58 | 687.3 | 0.000 | 58 | 686.1 | 0.001 |
| 59 | 689.6 | 0.000 | 59 | 695.3 | 0.000 | 59 | 688.0 | 0.000 |
| 60 | 706.3 | 0.000 | 60 | 701.6 | 0.000 | 60 | 702.9 | 0.000 |
| 61 | 706.8 | 0.000 | 61 | 708.3 | 0.000 | 61 | 703.2 | 0.002 |
| 62 | 716.6 | 0.000 | 62 | 722.8 | 0.000 | 62 | 706.5 | 0.000 |
| 63 | 718.6 | 0.001 | 63 | 725.9 | 0.000 | 63 | 710.6 | 0.001 |
| 64 | 723.4 | 0.001 | 64 | 732.4 | 0.001 | 64 | 720.9 | 0.000 |
| 65 | 728.5 | 0.001 | 65 | 735.8 | 0.000 | 65 | 725.2 | 0.002 |
| 66 | 730.0 | 0.000 | 66 | 739.3 | 0.001 | 66 | 734.2 | 0.000 |
| 67 | 753.5 | 0.000 | 67 | 753.9 | 0.000 | 67 | 738.4 | 0.000 |
| 68 | 755.3 | 0.001 | 68 | 756.0 | 0.000 | 68 | 756.2 | 0.001 |
| 69 | 765.2 | 0.001 | 69 | 767.9 | 0.000 | 69 | 762.0 | 0.002 |
| 70 | 769.4 | 0.000 | 70 | 780.2 | 0.000 | 70 | 769.5 | 0.001 |
| 71 | 779.3 | 0.001 | 71 | 783.6 | 0.000 | 71 | 771.4 | 0.001 |

Continued on next page

**Table 16 continued from previous page**

| Mode | $\nu_i@T_1$ | $S_1$-$T_1$ | Mode | $\nu_i@T_2$ | $S_1$-$T_2$ | Mode | $\nu_i@T_2$ | $S_1$-$T_3$ |
|---|---|---|---|---|---|---|---|---|
| 72 | 792.3 | 0.002 | 72 | 791.5 | 0.001 | 72 | 779.5 | 0.001 |
| 73 | 795.1 | 0.001 | 73 | 796.6 | 0.000 | 73 | 792.2 | 0.003 |
| 74 | 798.6 | 0.001 | 74 | 802.3 | 0.000 | 74 | 796.6 | 0.000 |
| 75 | 801.0 | 0.003 | 75 | 808.4 | 0.000 | 75 | 798.0 | 0.002 |
| 76 | 812.3 | 0.001 | 76 | 812.8 | 0.000 | 76 | 810.8 | 0.001 |
| 77 | 829.8 | 0.002 | 77 | 835.5 | 0.001 | 77 | 827.4 | 0.002 |
| 78 | 845.4 | 0.002 | 78 | 842.3 | 0.001 | 78 | 843.6 | 0.001 |
| 79 | 846.6 | 0.001 | 79 | 848.1 | 0.000 | 79 | 861.8 | 0.001 |
| 80 | 866.7 | 0.001 | 80 | 848.2 | 0.000 | 80 | 869.1 | 0.000 |
| 81 | 874.3 | 0.001 | 81 | 872.0 | 0.000 | 81 | 875.0 | 0.001 |
| 82 | 901.1 | 0.000 | 82 | 877.7 | 0.000 | 82 | 899.1 | 0.001 |
| 83 | 904.8 | 0.001 | 83 | 905.1 | 0.000 | 83 | 902.3 | 0.001 |
| 84 | 910.9 | 0.002 | 84 | 910.6 | 0.000 | 84 | 909.8 | 0.000 |
| 85 | 916.5 | 0.000 | 85 | 916.6 | 0.000 | 85 | 914.0 | 0.000 |
| 86 | 931.1 | 0.000 | 86 | 930.5 | 0.000 | 86 | 930.7 | 0.000 |
| 87 | 940.6 | 0.000 | 87 | 937.6 | 0.000 | 87 | 936.1 | 0.000 |
| 88 | 944.1 | 0.000 | 88 | 956.9 | 0.000 | 88 | 953.2 | 0.000 |
| 89 | 952.4 | 0.000 | 89 | 958.3 | 0.000 | 89 | 955.3 | 0.000 |
| 90 | 960.7 | 0.001 | 90 | 964.2 | 0.000 | 90 | 965.0 | 0.001 |
| 91 | 972.7 | 0.001 | 91 | 985.5 | 0.000 | 91 | 987.1 | 0.000 |
| 92 | 991.6 | 0.000 | 92 | 995.7 | 0.000 | 92 | 991.2 | 0.000 |

Continued on next page

**Table 16 continued from previous page**

| Mode | $\nu_i@T_1$ | $S_1$-$T_1$ | Mode | $\nu_i@T_2$ | $S_1$-$T_2$ | Mode | $\nu_i@T_2$ | $S_1$-$T_3$ |
|---|---|---|---|---|---|---|---|---|
| 93 | 998.6 | 0.001 | 93 | 998.8 | 0.000 | 93 | 993.6 | 0.001 |
| 94 | 1002.7 | 0.000 | 94 | 1016.0 | 0.000 | 94 | 1019.1 | 0.000 |
| 95 | 1012.5 | 0.000 | 95 | 1019.3 | 0.000 | 95 | 1022.6 | 0.000 |
| 96 | 1023.8 | 0.001 | 96 | 1026.8 | 0.000 | 96 | 1026.3 | 0.001 |
| 97 | 1042.7 | 0.000 | 97 | 1041.3 | 0.000 | 97 | 1038.1 | 0.000 |
| 98 | 1044.4 | 0.000 | 98 | 1042.5 | 0.000 | 98 | 1040.8 | 0.000 |
| 99 | 1044.8 | 0.000 | 99 | 1044.7 | 0.000 | 99 | 1042.8 | 0.001 |
| 100 | 1047.9 | 0.001 | 100 | 1046.5 | 0.000 | 100 | 1043.2 | 0.001 |
| 101 | 1056.0 | 0.001 | 101 | 1051.6 | 0.000 | 101 | 1055.8 | 0.000 |
| 102 | 1060.2 | 0.001 | 102 | 1062.4 | 0.000 | 102 | 1060.2 | 0.000 |
| 103 | 1073.0 | 0.000 | 103 | 1073.3 | 0.000 | 103 | 1072.6 | 0.000 |
| 104 | 1080.5 | 0.001 | 104 | 1076.3 | 0.000 | 104 | 1075.7 | 0.000 |
| 105 | 1089.6 | 0.000 | 105 | 1088.8 | 0.000 | 105 | 1089.7 | 0.000 |
| 106 | 1093.9 | 0.001 | 106 | 1094.9 | 0.000 | 106 | 1097.2 | 0.000 |
| 107 | 1101.7 | 0.001 | 107 | 1106.4 | 0.000 | 107 | 1103.4 | 0.001 |
| 108 | 1107.3 | 0.000 | 108 | 1114.8 | 0.001 | 108 | 1107.6 | 0.000 |
| 109 | 1128.3 | 0.000 | 109 | 1130.5 | 0.000 | 109 | 1125.9 | 0.000 |
| 110 | 1132.1 | 0.001 | 110 | 1135.9 | 0.000 | 110 | 1134.4 | 0.000 |
| 111 | 1136.8 | 0.001 | 111 | 1137.2 | 0.000 | 111 | 1137.1 | 0.000 |
| 112 | 1144.6 | 0.000 | 112 | 1142.5 | 0.000 | 112 | 1143.3 | 0.001 |
| 113 | 1151.5 | 0.000 | 113 | 1146.2 | 0.000 | 113 | 1151.8 | 0.000 |

Continued on next page

**Table 16 continued from previous page**

| Mode | $\nu_i@T_1$ | $S_1$-$T_1$ | Mode | $\nu_i@T_2$ | $S_1$-$T_2$ | Mode | $\nu_i@T_2$ | $S_1$-$T_3$ |
|---|---|---|---|---|---|---|---|---|
| 114 | 1155.2 | 0.000 | 114 | 1155.6 | 0.000 | 114 | 1155.9 | 0.000 |
| 115 | 1162.2 | 0.001 | 115 | 1168.3 | 0.000 | 115 | 1157.7 | 0.000 |
| 116 | 1178.3 | 0.000 | 116 | 1178.1 | 0.000 | 116 | 1178.0 | 0.000 |
| 117 | 1178.4 | 0.000 | 117 | 1178.7 | 0.000 | 117 | 1178.7 | 0.000 |
| 118 | 1189.2 | 0.000 | 118 | 1183.5 | 0.000 | 118 | 1179.6 | 0.000 |
| 119 | 1199.0 | 0.001 | 119 | 1195.1 | 0.000 | 119 | 1197.1 | 0.000 |
| 120 | 1203.4 | 0.000 | 120 | 1196.7 | 0.000 | 120 | 1204.1 | 0.000 |
| 121 | 1204.8 | 0.001 | 121 | 1205.6 | 0.000 | 121 | 1209.4 | 0.000 |
| 122 | 1212.0 | 0.000 | 122 | 1207.9 | 0.000 | 122 | 1212.8 | 0.000 |
| 123 | 1215.7 | 0.000 | 123 | 1212.9 | 0.000 | 123 | 1221.5 | 0.000 |
| 124 | 1225.7 | 0.001 | 124 | 1223.4 | 0.000 | 124 | 1225.5 | 0.000 |
| 125 | 1227.1 | 0.000 | 125 | 1230.5 | 0.000 | 125 | 1236.5 | 0.001 |
| 126 | 1238.7 | 0.000 | 126 | 1234.1 | 0.000 | 126 | 1246.3 | 0.000 |
| 127 | 1242.3 | 0.001 | 127 | 1258.6 | 0.000 | 127 | 1260.7 | 0.000 |
| 128 | 1260.5 | 0.000 | 128 | 1259.5 | 0.000 | 128 | 1267.7 | 0.000 |
| 129 | 1269.5 | 0.001 | 129 | 1287.5 | 0.000 | 129 | 1278.8 | 0.000 |
| 130 | 1275.4 | 0.000 | 130 | 1288.3 | 0.000 | 130 | 1289.1 | 0.000 |
| 131 | 1287.2 | 0.000 | 131 | 1292.8 | 0.000 | 131 | 1295.7 | 0.000 |
| 132 | 1298.0 | 0.000 | 132 | 1305.3 | 0.000 | 132 | 1308.7 | 0.000 |
| 133 | 1299.7 | 0.001 | 133 | 1307.9 | 0.000 | 133 | 1311.6 | 0.000 |
| 134 | 1307.3 | 0.000 | 134 | 1323.7 | 0.000 | 134 | 1323.0 | 0.000 |

Continued on next page

**Table 16 continued from previous page**

| Mode | $\nu_i@T_1$ | $S_1$-$T_1$ | Mode | $\nu_i@T_2$ | $S_1$-$T_2$ | Mode | $\nu_i@T_2$ | $S_1$-$T_3$ |
|---|---|---|---|---|---|---|---|---|
| 135 | 1314.6 | 0.000 | 135 | 1326.8 | 0.000 | 135 | 1326.2 | 0.001 |
| 136 | 1333.8 | 0.000 | 136 | 1341.8 | 0.000 | 136 | 1331.7 | 0.000 |
| 137 | 1339.9 | 0.001 | 137 | 1358.6 | 0.000 | 137 | 1337.5 | 0.000 |
| 138 | 1348.6 | 0.001 | 138 | 1365.4 | 0.000 | 138 | 1351.7 | 0.000 |
| 139 | 1362.8 | 0.001 | 139 | 1371.6 | 0.000 | 139 | 1360.9 | 0.001 |
| 140 | 1371.5 | 0.001 | 140 | 1377.2 | 0.001 | 140 | 1371.6 | 0.000 |
| 141 | 1381.0 | 0.000 | 141 | 1379.2 | 0.000 | 141 | 1380.2 | 0.000 |
| 142 | 1384.8 | 0.000 | 142 | 1389.6 | 0.000 | 142 | 1382.5 | 0.000 |
| 143 | 1392.6 | 0.000 | 143 | 1397.2 | 0.000 | 143 | 1386.5 | 0.001 |
| 144 | 1394.2 | 0.001 | 144 | 1398.2 | 0.000 | 144 | 1396.7 | 0.000 |
| 145 | 1400.5 | 0.000 | 145 | 1401.8 | 0.000 | 145 | 1398.8 | 0.000 |
| 146 | 1400.6 | 0.000 | 146 | 1406.9 | 0.000 | 146 | 1399.2 | 0.000 |
| 147 | 1402.1 | 0.000 | 147 | 1413.9 | 0.000 | 147 | 1402.2 | 0.001 |
| 148 | 1415.6 | 0.000 | 148 | 1418.1 | 0.000 | 148 | 1408.8 | 0.001 |
| 149 | 1419.9 | 0.000 | 149 | 1427.1 | 0.000 | 149 | 1416.4 | 0.000 |
| 150 | 1421.3 | 0.000 | 150 | 1431.8 | 0.000 | 150 | 1420.2 | 0.000 |
| 151 | 1432.9 | 0.001 | 151 | 1440.2 | 0.000 | 151 | 1432.9 | 0.000 |
| 152 | 1437.4 | 0.001 | 152 | 1446.1 | 0.000 | 152 | 1445.3 | 0.000 |
| 153 | 1443.4 | 0.000 | 153 | 1447.6 | 0.000 | 153 | 1448.2 | 0.000 |
| 154 | 1447.5 | 0.000 | 154 | 1450.1 | 0.000 | 154 | 1449.1 | 0.000 |
| 155 | 1449.1 | 0.000 | 155 | 1452.2 | 0.000 | 155 | 1451.2 | 0.000 |

Continued on next page

**Table 16 continued from previous page**

| Mode | $\nu_i@T_1$ | $S_1$-$T_1$ | Mode | $\nu_i@T_2$ | $S_1$-$T_2$ | Mode | $\nu_i@T_2$ | $S_1$-$T_3$ |
|---|---|---|---|---|---|---|---|---|
| 156 | 1452.7 | 0.001 | 156 | 1455.5 | 0.000 | 156 | 1453.9 | 0.000 |
| 157 | 1453.4 | 0.000 | 157 | 1455.5 | 0.000 | 157 | 1455.1 | 0.000 |
| 158 | 1456.4 | 0.000 | 158 | 1458.4 | 0.000 | 158 | 1457.1 | 0.001 |
| 159 | 1457.5 | 0.000 | 159 | 1458.8 | 0.000 | 159 | 1458.2 | 0.000 |
| 160 | 1457.9 | 0.000 | 160 | 1459.3 | 0.000 | 160 | 1459.2 | 0.000 |
| 161 | 1458.4 | 0.000 | 161 | 1462.4 | 0.000 | 161 | 1459.7 | 0.000 |
| 162 | 1460.5 | 0.001 | 162 | 1463.8 | 0.000 | 162 | 1463.5 | 0.000 |
| 163 | 1464.3 | 0.000 | 163 | 1464.7 | 0.000 | 163 | 1464.3 | 0.000 |
| 164 | 1465.1 | 0.001 | 164 | 1465.5 | 0.000 | 164 | 1464.5 | 0.000 |
| 165 | 1465.5 | 0.000 | 165 | 1466.0 | 0.000 | 165 | 1465.1 | 0.000 |
| 166 | 1466.4 | 0.000 | 166 | 1466.2 | 0.000 | 166 | 1466.1 | 0.000 |
| 167 | 1466.4 | 0.000 | 167 | 1466.4 | 0.000 | 167 | 1467.0 | 0.000 |
| 168 | 1467.0 | 0.000 | 168 | 1467.4 | 0.000 | 168 | 1467.4 | 0.000 |
| 169 | 1467.5 | 0.000 | 169 | 1470.2 | 0.000 | 169 | 1472.6 | 0.001 |
| 170 | 1471.0 | 0.001 | 170 | 1473.9 | 0.000 | 170 | 1476.8 | 0.001 |
| 171 | 1478.5 | 0.000 | 171 | 1478.4 | 0.000 | 171 | 1477.9 | 0.000 |
| 172 | 1480.3 | 0.000 | 172 | 1483.5 | 0.000 | 172 | 1484.2 | 0.000 |
| 173 | 1483.2 | 0.000 | 173 | 1484.3 | 0.000 | 173 | 1484.7 | 0.000 |
| 174 | 1489.2 | 0.000 | 174 | 1488.4 | 0.000 | 174 | 1497.4 | 0.000 |
| 175 | 1518.9 | 0.001 | 175 | 1532.9 | 0.000 | 175 | 1505.8 | 0.001 |
| 176 | 1534.8 | 0.000 | 176 | 1551.2 | 0.000 | 176 | 1521.7 | 0.001 |

Continued on next page

**Table 16 continued from previous page**

| Mode | $\nu_i@T_1$ | $S_1$-$T_1$ | Mode | $\nu_i@T_2$ | $S_1$-$T_2$ | Mode | $\nu_i@T_2$ | $S_1$-$T_3$ |
|---|---|---|---|---|---|---|---|---|
| 177 | 1544.8 | 0.000 | 177 | 1559.2 | 0.000 | 177 | 1533.2 | 0.001 |
| 178 | 1551.9 | 0.000 | 178 | 1600.6 | 0.000 | 178 | 1586.6 | 0.000 |
| 179 | 1561.2 | 0.000 | 179 | 1620.6 | 0.000 | 179 | 1601.1 | 0.001 |
| 180 | 1578.5 | 0.001 | 180 | 1629.2 | 0.000 | 180 | 1605.9 | 0.001 |
| 181 | 1600.0 | 0.001 | 181 | 1661.5 | 0.000 | 181 | 1632.8 | 0.000 |
| 182 | 1630.8 | 0.001 | 182 | 1705.8 | 0.000 | 182 | 1659.8 | 0.000 |
| 183 | 1696.8 | 0.000 | 183 | 1720.4 | 0.000 | 183 | 1690.1 | 0.000 |
| 184 | 1722.7 | 0.000 | 184 | 1732.6 | 0.000 | 184 | 1712.6 | 0.000 |
| 185 | 1730.5 | 0.000 | 185 | 1818.2 | 0.000 | 185 | 1839.9 | 0.000 |
| 186 | 1743.4 | 0.001 | 186 | 1844.3 | 0.000 | 186 | 1843.6 | 0.000 |
| 187 | 1828.8 | 0.000 | 187 | 1848.9 | 0.000 | 187 | 1856.0 | 0.000 |
| 188 | 1842.6 | 0.000 | 188 | 2115.5 | 0.004 | 188 | 2013.4 | 0.002 |
| 189 | 1851.4 | 0.000 | 189 | 2971.5 | 0.022 | 189 | 2627.2 | 0.017 |
| 190 | 3049.8 | 0.000 | 190 | 3051.3 | 0.000 | 190 | 3039.3 | 0.000 |
| 191 | 3051.7 | 0.000 | 191 | 3052.1 | 0.000 | 191 | 3050.0 | 0.000 |
| 192 | 3052.5 | 0.000 | 192 | 3052.5 | 0.000 | 192 | 3053.1 | 0.000 |
| 193 | 3053.0 | 0.000 | 193 | 3054.6 | 0.001 | 193 | 3053.6 | 0.000 |
| 194 | 3054.0 | 0.000 | 194 | 3055.0 | 0.000 | 194 | 3054.2 | 0.000 |
| 195 | 3064.0 | 0.000 | 195 | 3066.6 | 0.000 | 195 | 3060.7 | 0.000 |
| 196 | 3065.4 | 0.000 | 196 | 3072.1 | 0.000 | 196 | 3061.9 | 0.000 |
| 197 | 3071.6 | 0.000 | 197 | 3072.5 | 0.000 | 197 | 3072.4 | 0.000 |

Continued on next page

**Table 16 continued from previous page**

| Mode | $\nu_i@T_1$ | $S_1$-$T_1$ | Mode | $\nu_i@T_2$ | $S_1$-$T_2$ | Mode | $\nu_i@T_2$ | $S_1$-$T_3$ |
|---|---|---|---|---|---|---|---|---|
| 198 | 3071.8 | 0.000 | 198 | 3075.8 | 0.002 | 198 | 3072.5 | 0.000 |
| 199 | 3074.0 | 0.000 | 199 | 3078.3 | 0.001 | 199 | 3075.5 | 0.000 |
| 200 | 3082.3 | 0.000 | 200 | 3086.5 | 0.001 | 200 | 3083.6 | 0.000 |
| 201 | 3092.8 | 0.000 | 201 | 3094.4 | 0.000 | 201 | 3090.9 | 0.000 |
| 202 | 3099.8 | 0.001 | 202 | 3096.9 | 0.001 | 202 | 3092.5 | 0.000 |
| 203 | 3111.0 | 0.000 | 203 | 3111.9 | 0.000 | 203 | 3102.3 | 0.000 |
| 204 | 3119.2 | 0.000 | 204 | 3120.3 | 0.000 | 204 | 3103.7 | 0.000 |
| 205 | 3122.0 | 0.000 | 205 | 3121.7 | 0.000 | 205 | 3123.4 | 0.000 |
| 206 | 3123.0 | 0.000 | 206 | 3128.2 | 0.000 | 206 | 3129.6 | 0.000 |
| 207 | 3129.0 | 0.000 | 207 | 3135.1 | 0.001 | 207 | 3129.9 | 0.000 |
| 208 | 3141.9 | 0.000 | 208 | 3141.3 | 0.000 | 208 | 3135.8 | 0.000 |
| 209 | 3141.9 | 0.000 | 209 | 3142.5 | 0.001 | 209 | 3139.5 | 0.000 |
| 210 | 3143.8 | 0.000 | 210 | 3146.2 | 0.000 | 210 | 3141.5 | 0.000 |
| 211 | 3144.4 | 0.000 | 211 | 3149.2 | 0.001 | 211 | 3144.5 | 0.000 |
| 212 | 3145.9 | 0.000 | 212 | 3149.7 | 0.001 | 212 | 3148.5 | 0.000 |
| 213 | 3159.2 | 0.000 | 213 | 3156.9 | 0.000 | 213 | 3150.1 | 0.000 |
| 214 | 3161.1 | 0.000 | 214 | 3160.0 | 0.000 | 214 | 3163.1 | 0.000 |
| 215 | 3164.9 | 0.000 | 215 | 3164.8 | 0.000 | 215 | 3165.4 | 0.000 |
| 216 | 3165.5 | 0.000 | 216 | 3166.6 | 0.000 | 216 | 3166.6 | 0.000 |
| 217 | 3168.3 | 0.000 | 217 | 3170.4 | 0.000 | 217 | 3170.5 | 0.000 |
| 218 | 3173.4 | 0.000 | 218 | 3171.5 | 0.000 | 218 | 3173.3 | 0.000 |

Continued on next page

**Table 16 continued from previous page**

| Mode | $\nu_i$@$T_1$ | $S_1$-$T_1$ | Mode | $\nu_i$@$T_2$ | $S_1$-$T_2$ | Mode | $\nu_i$@$T_2$ | $S_1$-$T_3$ |
|---|---|---|---|---|---|---|---|---|
| 219 | 3185.9 | 0.000 | 219 | 3181.5 | 0.000 | 219 | 3180.6 | 0.000 |
| 220 | 3201.7 | 0.000 | 220 | 3201.5 | 0.000 | 220 | 3201.6 | 0.000 |
| 221 | 3201.7 | 0.000 | 221 | 3202.2 | 0.000 | 221 | 3202.0 | 0.000 |
| 222 | 3226.6 | 0.000 | 222 | 3231.2 | 0.002 | 222 | 3224.7 | 0.000 |
| 223 | 3234.7 | 0.000 | 223 | 3246.8 | 0.001 | 223 | 3226.0 | 0.001 |
| 224 | 3235.5 | 0.000 | 224 | 3248.2 | 0.000 | 224 | 3244.8 | 0.001 |
| 225 | 3280.3 | 0.000 | 225 | 3271.6 | 0.000 | 225 | 3272.6 | 0.000 |
| 226 | 3539.7 | 0.000 | 226 | 3431.2 | 0.002 | 226 | 3533.9 | 0.001 |
| 227 | 3635.6 | 0.000 | 227 | 3596.2 | 0.001 | 227 | 3645.3 | 0.000 |

**Table 17.** *The five largest coupling vibrational normal modes calculated at their own $T_n(\pi\rightarrow\pi^*)$ minimum of methylpheophorbide a (MPh).*

| ISC $S_1(\pi\rightarrow\pi^*) \rightsquigarrow T_1(\pi\rightarrow\pi^*)$ | ISC $S_1(\pi\rightarrow\pi^*) \rightsquigarrow T_2(\pi\rightarrow\pi^*)$ | ISC $S_1(\pi\rightarrow\pi^*) \rightsquigarrow T_3(\pi\rightarrow\pi^*)$ |
|---|---|---|
| 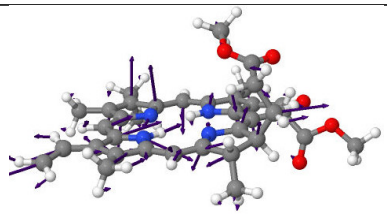 | 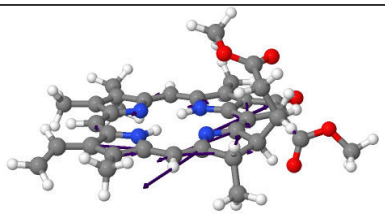 | 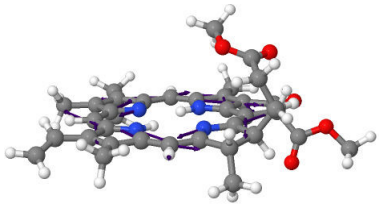 |
| 46 | 189 | 189 |
| 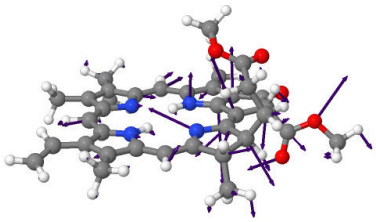 | 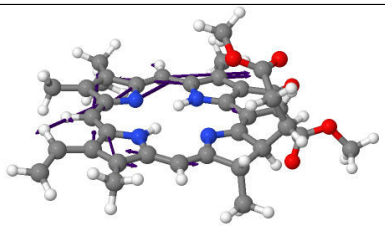 | 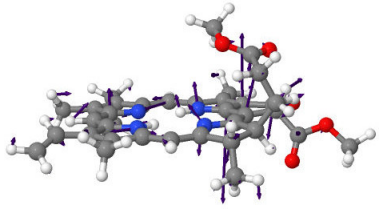 |

| 75 | 188 | 73 |
|---|---|---|
| 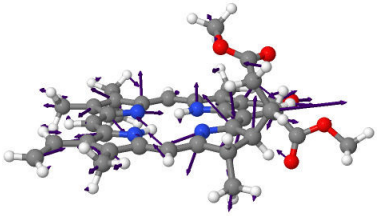 | 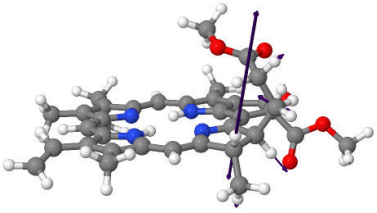 | 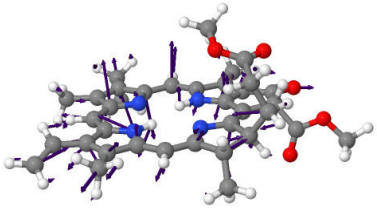 |
| 47 | 198 | 46 |
| 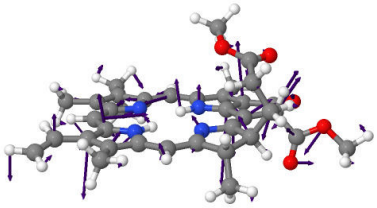 | 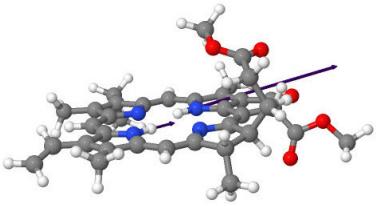 | 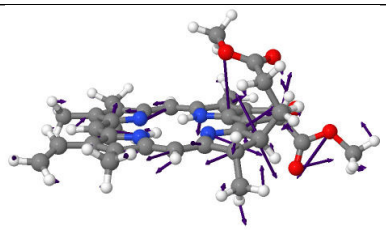 |
| 72 | 226 | 75 |
| 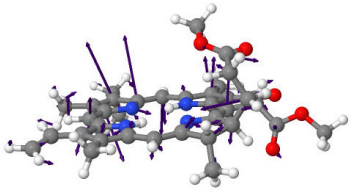 | 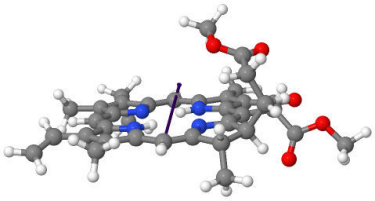 | 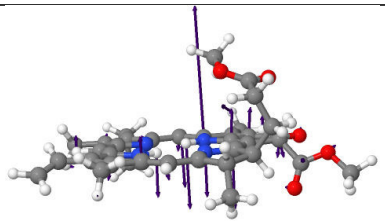 |
| 48 | 222 | 61 |

**Appendix C: Supporting Information for the Second Protocol**

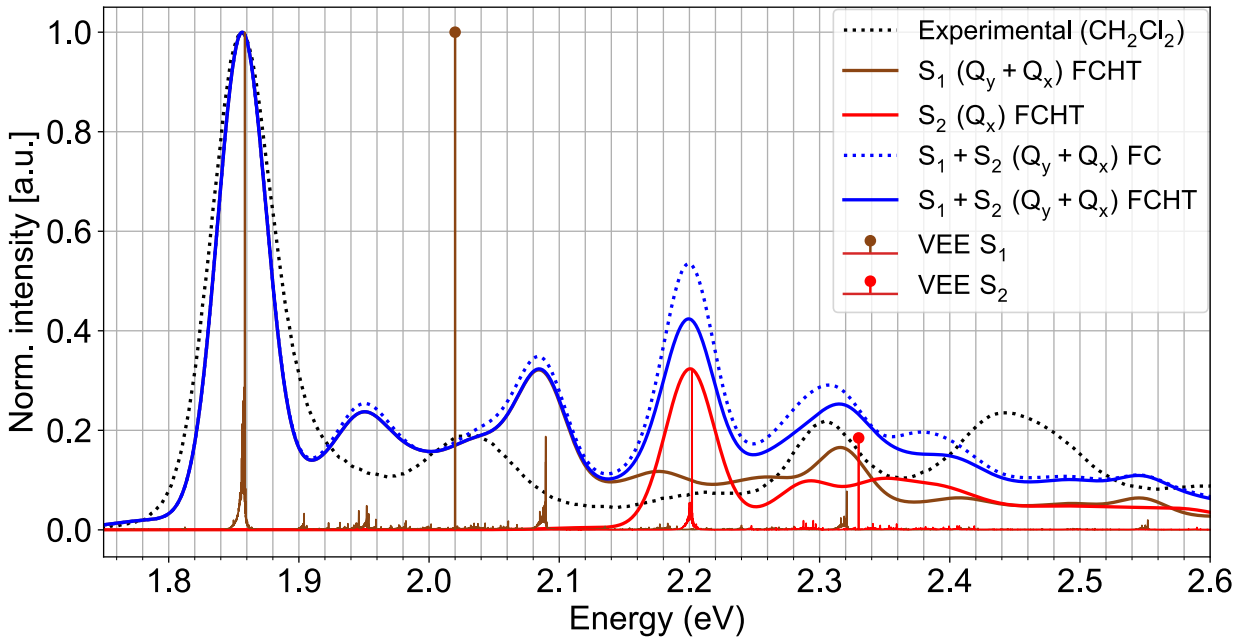


**Figure 35.** Computed vibronic structure and stick spectrum of the Q-band employing the adiabatic Hessian approximation, Franck-Condon and Franck-Condon-Herzberg-Teller contributions at 298.15 K. The Gaussian linewidth was set to 150 $cm^{-1}$ and vibrational modes below 350 $cm^{-1}$ were removed. The calculated spectra and VEEs were shifted by 0.32 eV to align with the experimental band maximum.

**Table 18.** *Adiabatic energy differences between the lowest singlet excited state and the ground state computed at different levels of theory using the CAM-B3LYP/def2-SVP optimized structure.*

| Level of theory | $\Delta E_{S1\text{-}S0}$ (eV) | $\Delta E_{S2\text{-}S0}$ (eV) |
|---|---|---|
| CAM-B3LYP/def2-SVP | 2.20 | 2.56 |
| CAM-B3LYP/def2-TZVP | 2.19 | 2.56 |
| $\omega$B97X/def2-SVP | 2.21 | 2.68 |
| $\omega$B97X/def2-TZVP | 2.20 | 2.68 |
| PBE0/def2-SVP | 2.18 | 2.42 |
| PBE0/def2-TZVP | 2.17 | 2.41 |

**Table 19.** *TDA-DFT spectroscopic parameters for the Q band calculated in toluene with different density functionals and bases and using the CAM-B3LYP/def2-SVP optimized structure.*

| Experimental (eV) | Functional | def2-SVP | | | def2-TZVP | | |
|---|---|---|---|---|---|---|---|
| | | VEE (eV) | $\lambda$ (nm) | $f_{osc.}$ | VEE (eV) | $\lambda$ (nm) | $f_{osc.}$ |
| 1.85 | CAM-B3LYP | 2.343 | 529.1 | 0.3302 | 2.300 | 539.1 | 0.3639 |
| | $\omega$B97X | 2.390 | 518.8 | 0.2945 | 2.346 | 528.4 | 0.3190 |
| | PBE0 | 2.290 | 541.4 | 0.3258 | 2.251 | 550.7 | 0.3613 |
| 2.31 | CAM-B3LYP | 2.653 | 467.4 | 0.0610 | 2.621 | 473.0 | 0.0634 |
| | $\omega$B97X | 2.826 | 438.8 | 0.1420 | 2.801 | 442.6 | 0.1574 |
| | PBE0 | 2.511 | 493.8 | 0.0427 | 2.479 | 500.2 | 0.0399 |

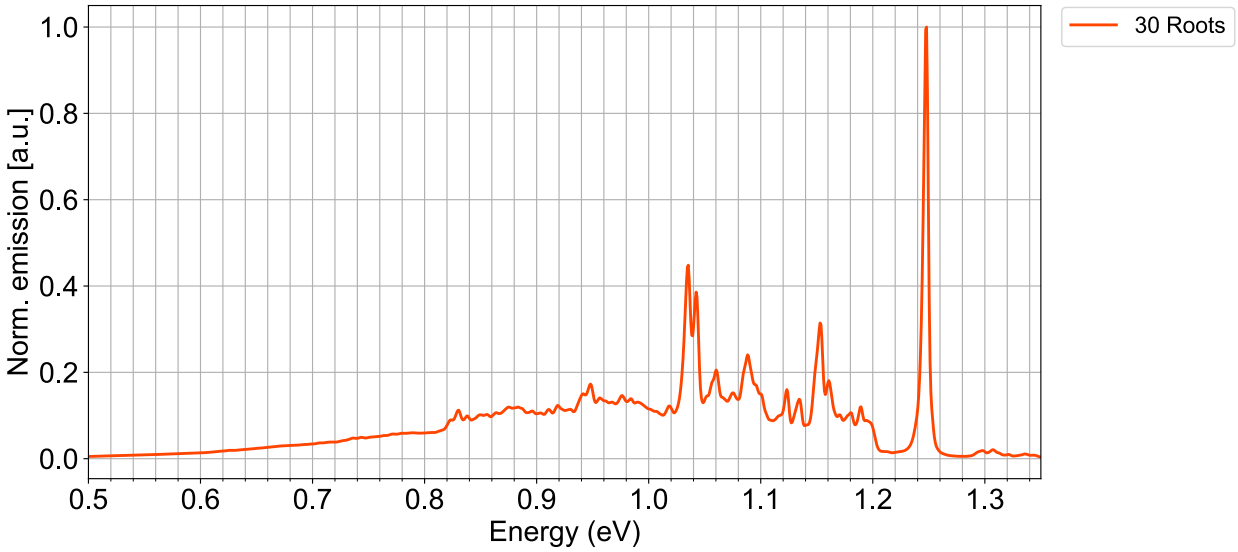


**Figure 36.** Computed phosphorescence spectrum employing the adiabatic Hessian approximation, Franck-Condon (FC) and Franck-Condon-Herzberg-Teller (FCHT) contributions at 298.15 K. The Gaussian linewidth was set to 10 $cm^{-1}$ and vibrational normal modes below 100 $cm^{-1}$ were discarded.

**Table 20.** *Adiabatic energy difference between the lowest singlet excited state and the first, second and third triplet state computed at different levels of theory using the CAM-B3LYP/def2-SVP optimized structure.*

| **Level of theory** | **$\Delta E_{S1\text{-}T1}$ (eV)** | **$\Delta E_{S1\text{-}T2}$ (eV)** | **$\Delta E_{S1\text{-}T3}$ (eV)** |
|---|---|---|---|
| CAM-B3LYP/def2-SVP | 0.92 | 0.59 | 0.13 |
| CAM-B3LYP/def2-TZVP | 0.90 | 0.52 | 0.11 |
| $\omega$B97X/def2-SVP | 0.94 | 0.53 | 0.10 |
| $\omega$B97X/def2-TZVP | 0.92 | 0.46 | 0.07 |
| PBE0/def2-SVP | 0.85 | 0.62 | 0.16 |
| PBE0/def2-TZVP | 0.84 | 0.56 | 0.14 |

**Table 21.** *Harmonic frequencies $v_i$ ($cm^{-1}$) and triplet-sublevels-averaged ∂SOCMEs ($cm^{-1}$) with respect to the corresponding vibrational modes at the equilibrium geometry of $T_1$, $T_2$ and $T_3$ states.*

| Mode | $v_i$@$T_1$ | $S_1$-$T_1$ | Mode | $v_i$@$T_2$ | $S_1$-$T_2$ | Mode | $v_i$@$T_2$ | $S_1$-$T_3$ |
|---|---|---|---|---|---|---|---|---|
| 1 | 100.5 | 0.000 | 1 | 105.4 | 0.000 | 1 | 100.6 | 0.000 |
| 2 | 108.7 | 0.000 | 2 | 118.5 | 0.001 | 2 | 108.2 | 0.000 |
| 3 | 118.1 | 0.000 | 3 | 123.2 | 0.000 | 3 | 116.8 | 0.000 |
| 4 | 122.4 | 0.000 | 4 | 130.6 | 0.000 | 4 | 123.9 | 0.000 |
| 5 | 126.7 | 0.000 | 5 | 133.4 | 0.000 | 5 | 131.9 | 0.000 |
| 6 | 132.3 | 0.000 | 6 | 138.3 | 0.000 | 6 | 136.6 | 0.000 |
| 7 | 135.4 | 0.000 | 7 | 142.0 | 0.000 | 7 | 143.9 | 0.000 |
| 8 | 141.1 | 0.000 | 8 | 147.4 | 0.000 | 8 | 155.5 | 0.000 |
| 9 | 144.4 | 0.000 | 9 | 151.5 | 0.000 | 9 | 158.2 | 0.000 |
| 10 | 157.1 | 0.000 | 10 | 158.3 | 0.000 | 10 | 159.7 | 0.000 |
| 11 | 164.4 | 0.000 | 11 | 162.8 | 0.001 | 11 | 169.2 | 0.000 |
| 12 | 173.2 | 0.000 | 12 | 173.1 | 0.000 | 12 | 174.5 | 0.000 |
| 13 | 186.2 | 0.000 | 13 | 182.0 | 0.000 | 13 | 181.7 | 0.000 |
| 14 | 189.3 | 0.000 | 14 | 186.3 | 0.001 | 14 | 186.3 | 0.000 |
| 15 | 195.7 | 0.000 | 15 | 195.5 | 0.000 | 15 | 188.9 | 0.000 |
| 16 | 196.9 | 0.000 | 16 | 196.3 | 0.001 | 16 | 196.6 | 0.000 |
| 17 | 211.2 | 0.000 | 17 | 210.4 | 0.000 | 17 | 198.5 | 0.000 |
| 18 | 213.7 | 0.000 | 18 | 214.8 | 0.000 | 18 | 212.3 | 0.000 |
| 19 | 223.0 | 0.000 | 19 | 221.1 | 0.001 | 19 | 217.7 | 0.000 |
| 20 | 233.3 | 0.000 | 20 | 232.8 | 0.001 | 20 | 223.5 | 0.000 |

Continued on next page

**Table 21 continued from previous page**

| Mode | $v_i@T_1$ | $S_1$-$T_1$ | Mode | $v_i@T_2$ | $S_1$-$T_2$ | Mode | $v_i@T_2$ | $S_1$-$T_3$ |
|---|---|---|---|---|---|---|---|---|
| 21 | 239.1 | 0.000 | 21 | 235.9 | 0.000 | 21 | 234.6 | 0.000 |
| 22 | 246.3 | 0.000 | 22 | 240.3 | 0.001 | 22 | 241.8 | 0.000 |
| 23 | 252.1 | 0.000 | 23 | 252.9 | 0.000 | 23 | 243.1 | 0.000 |
| 24 | 257.7 | 0.000 | 24 | 256.3 | 0.000 | 24 | 250.8 | 0.000 |
| 25 | 263.9 | 0.001 | 25 | 264.5 | 0.001 | 25 | 261.7 | 0.000 |
| 26 | 267.1 | 0.000 | 26 | 269.6 | 0.001 | 26 | 266.6 | 0.000 |
| 27 | 272.2 | 0.000 | 27 | 270.4 | 0.001 | 27 | 269.1 | 0.001 |
| 28 | 276.4 | 0.000 | 28 | 280.0 | 0.001 | 28 | 282.7 | 0.000 |
| 29 | 286.0 | 0.000 | 29 | 287.0 | 0.001 | 29 | 286.1 | 0.000 |
| 30 | 291.2 | 0.000 | 30 | 293.9 | 0.001 | 30 | 290.1 | 0.000 |
| 31 | 296.4 | 0.000 | 31 | 297.9 | 0.001 | 31 | 294.0 | 0.000 |
| 32 | 316.6 | 0.000 | 32 | 317.3 | 0.000 | 32 | 300.0 | 0.000 |
| 33 | 321.5 | 0.001 | 33 | 320.5 | 0.002 | 33 | 312.5 | 0.000 |
| 34 | 345.3 | 0.000 | 34 | 346.1 | 0.001 | 34 | 327.0 | 0.000 |
| 35 | 362.3 | 0.000 | 35 | 362.9 | 0.001 | 35 | 344.4 | 0.000 |
| 36 | 368.4 | 0.000 | 36 | 367.4 | 0.001 | 36 | 360.1 | 0.001 |
| 37 | 383.1 | 0.002 | 37 | 379.1 | 0.004 | 37 | 368.3 | 0.000 |
| 38 | 386.4 | 0.001 | 38 | 384.0 | 0.001 | 38 | 374.7 | 0.001 |
| 39 | 409.8 | 0.000 | 39 | 412.7 | 0.000 | 39 | 390.9 | 0.001 |
| 40 | 429.6 | 0.001 | 40 | 429.6 | 0.002 | 40 | 416.6 | 0.000 |
| 41 | 443.6 | 0.001 | 41 | 444.4 | 0.002 | 41 | 429.4 | 0.000 |

Continued on next page

**Table 21 continued from previous page**

| Mode | $\nu_i@T_1$ | $S_1$-$T_1$ | Mode | $\nu_i@T_2$ | $S_1$-$T_2$ | Mode | $\nu_i@T_2$ | $S_1$-$T_3$ |
|---|---|---|---|---|---|---|---|---|
| 42 | 462.4 | 0.001 | 42 | 461.5 | 0.004 | 42 | 445.2 | 0.001 |
| 43 | 469.1 | 0.002 | 43 | 466.2 | 0.002 | 43 | 461.3 | 0.000 |
| 44 | 480.2 | 0.001 | 44 | 476.6 | 0.002 | 44 | 471.0 | 0.001 |
| 45 | 493.5 | 0.002 | 45 | 488.9 | 0.003 | 45 | 486.2 | 0.001 |
| 46 | 521.1 | 0.003 | 46 | 522.3 | 0.004 | 46 | 489.5 | 0.002 |
| 47 | 538.0 | 0.003 | 47 | 535.3 | 0.007 | 47 | 509.3 | 0.002 |
| 48 | 552.8 | 0.002 | 48 | 555.1 | 0.005 | 48 | 529.2 | 0.001 |
| 49 | 575.3 | 0.000 | 49 | 575.7 | 0.001 | 49 | 542.7 | 0.001 |
| 50 | 593.1 | 0.000 | 50 | 592.2 | 0.001 | 50 | 548.9 | 0.001 |
| 51 | 610.6 | 0.001 | 51 | 611.3 | 0.002 | 51 | 570.2 | 0.000 |
| 52 | 615.3 | 0.000 | 52 | 620.5 | 0.003 | 52 | 592.6 | 0.000 |
| 53 | 620.0 | 0.001 | 53 | 634.2 | 0.002 | 53 | 610.9 | 0.000 |
| 54 | 639.1 | 0.001 | 54 | 643.7 | 0.002 | 54 | 618.9 | 0.001 |
| 55 | 650.8 | 0.002 | 55 | 655.5 | 0.003 | 55 | 636.3 | 0.000 |
| 56 | 663.6 | 0.001 | 56 | 668.9 | 0.002 | 56 | 658.3 | 0.001 |
| 57 | 673.8 | 0.001 | 57 | 683.6 | 0.002 | 57 | 664.1 | 0.001 |
| 58 | 685.6 | 0.001 | 58 | 687.3 | 0.001 | 58 | 672.2 | 0.000 |
| 59 | 691.7 | 0.000 | 59 | 695.3 | 0.002 | 59 | 688.3 | 0.001 |
| 60 | 706.0 | 0.000 | 60 | 701.6 | 0.001 | 60 | 690.1 | 0.000 |
| 61 | 707.7 | 0.000 | 61 | 708.3 | 0.001 | 61 | 700.2 | 0.002 |
| 62 | 720.6 | 0.001 | 62 | 722.8 | 0.001 | 62 | 700.7 | 0.001 |

Continued on next page

**Table 21 continued from previous page**

| Mode | $v_i@T_1$ | $S_1$-$T_1$ | Mode | $v_i@T_2$ | $S_1$-$T_2$ | Mode | $v_i@T_2$ | $S_1$-$T_3$ |
|---|---|---|---|---|---|---|---|---|
| 63 | 721.8 | 0.000 | 63 | 725.9 | 0.002 | 63 | 707.9 | 0.000 |
| 64 | 725.0 | 0.001 | 64 | 732.4 | 0.004 | 64 | 713.1 | 0.002 |
| 65 | 730.0 | 0.002 | 65 | 735.8 | 0.003 | 65 | 721.5 | 0.000 |
| 66 | 732.6 | 0.000 | 66 | 739.3 | 0.005 | 66 | 729.0 | 0.002 |
| 67 | 753.3 | 0.001 | 67 | 753.9 | 0.001 | 67 | 736.6 | 0.001 |
| 68 | 755.8 | 0.001 | 68 | 756.0 | 0.001 | 68 | 741.2 | 0.001 |
| 69 | 768.6 | 0.001 | 69 | 767.9 | 0.002 | 69 | 758.0 | 0.001 |
| 70 | 776.2 | 0.000 | 70 | 780.2 | 0.002 | 70 | 768.7 | 0.002 |
| 71 | 782.8 | 0.000 | 71 | 783.6 | 0.002 | 71 | 772.0 | 0.001 |
| 72 | 789.8 | 0.002 | 72 | 791.5 | 0.008 | 72 | 775.7 | 0.001 |
| 73 | 795.9 | 0.002 | 73 | 796.6 | 0.001 | 73 | 783.1 | 0.002 |
| 74 | 799.3 | 0.001 | 74 | 802.3 | 0.001 | 74 | 791.7 | 0.003 |
| 75 | 801.4 | 0.003 | 75 | 808.4 | 0.002 | 75 | 797.2 | 0.000 |
| 76 | 812.9 | 0.001 | 76 | 812.8 | 0.001 | 76 | 800.5 | 0.000 |
| 77 | 833.0 | 0.001 | 77 | 835.5 | 0.003 | 77 | 812.3 | 0.001 |
| 78 | 846.0 | 0.001 | 78 | 842.3 | 0.003 | 78 | 844.8 | 0.001 |
| 79 | 853.4 | 0.001 | 79 | 848.1 | 0.004 | 79 | 850.9 | 0.002 |
| 80 | 869.0 | 0.001 | 80 | 848.2 | 0.000 | 80 | 869.9 | 0.000 |
| 81 | 876.2 | 0.000 | 81 | 872.0 | 0.001 | 81 | 877.6 | 0.001 |
| 82 | 891.0 | 0.002 | 82 | 877.7 | 0.001 | 82 | 883.5 | 0.001 |
| 83 | 902.3 | 0.000 | 83 | 905.1 | 0.001 | 83 | 886.3 | 0.001 |

Continued on next page

**Table 21 continued from previous page**

| Mode | $\nu_i@T_1$ | $S_1$-$T_1$ | Mode | $\nu_i@T_2$ | $S_1$-$T_2$ | Mode | $\nu_i@T_2$ | $S_1$-$T_3$ |
|---|---|---|---|---|---|---|---|---|
| 84 | 908.6 | 0.000 | 84 | 910.6 | 0.000 | 84 | 905.7 | 0.001 |
| 85 | 916.7 | 0.000 | 85 | 916.6 | 0.001 | 85 | 911.5 | 0.000 |
| 86 | 931.6 | 0.000 | 86 | 930.5 | 0.000 | 86 | 915.4 | 0.000 |
| 87 | 940.7 | 0.000 | 87 | 937.6 | 0.000 | 87 | 929.1 | 0.000 |
| 88 | 948.8 | 0.000 | 88 | 956.9 | 0.000 | 88 | 936.2 | 0.000 |
| 89 | 956.0 | 0.000 | 89 | 958.3 | 0.000 | 89 | 955.3 | 0.000 |
| 90 | 963.6 | 0.001 | 90 | 964.2 | 0.001 | 90 | 959.9 | 0.000 |
| 91 | 989.5 | 0.000 | 91 | 985.5 | 0.000 | 91 | 965.6 | 0.001 |
| 92 | 994.8 | 0.001 | 92 | 995.7 | 0.002 | 92 | 989.2 | 0.000 |
| 93 | 996.7 | 0.000 | 93 | 998.8 | 0.000 | 93 | 994.7 | 0.000 |
| 94 | 1004.6 | 0.001 | 94 | 1016.0 | 0.000 | 94 | 995.2 | 0.000 |
| 95 | 1014.7 | 0.000 | 95 | 1019.3 | 0.000 | 95 | 1010.6 | 0.001 |
| 96 | 1025.6 | 0.001 | 96 | 1026.8 | 0.002 | 96 | 1020.6 | 0.000 |
| 97 | 1038.6 | 0.000 | 97 | 1041.3 | 0.001 | 97 | 1027.7 | 0.001 |
| 98 | 1041.2 | 0.000 | 98 | 1042.5 | 0.000 | 98 | 1035.1 | 0.000 |
| 99 | 1045.5 | 0.001 | 99 | 1044.7 | 0.002 | 99 | 1043.0 | 0.000 |
| 100 | 1047.0 | 0.001 | 100 | 1046.5 | 0.001 | 100 | 1043.5 | 0.000 |
| 101 | 1057.3 | 0.001 | 101 | 1051.6 | 0.001 | 101 | 1046.6 | 0.001 |
| 102 | 1071.9 | 0.000 | 102 | 1062.4 | 0.000 | 102 | 1047.3 | 0.001 |
| 103 | 1078.1 | 0.001 | 103 | 1073.3 | 0.000 | 103 | 1056.6 | 0.000 |
| 104 | 1087.0 | 0.001 | 104 | 1076.3 | 0.002 | 104 | 1074.6 | 0.000 |

Continued on next page

**Table 21 continued from previous page**

| Mode | $\nu_i@T_1$ | $S_1$-$T_1$ | Mode | $\nu_i@T_2$ | $S_1$-$T_2$ | Mode | $\nu_i@T_2$ | $S_1$-$T_3$ |
|---|---|---|---|---|---|---|---|---|
| 105 | 1090.8 | 0.000 | 105 | 1088.8 | 0.001 | 105 | 1078.4 | 0.001 |
| 106 | 1096.8 | 0.001 | 106 | 1094.9 | 0.002 | 106 | 1088.6 | 0.000 |
| 107 | 1104.4 | 0.001 | 107 | 1106.4 | 0.001 | 107 | 1093.5 | 0.000 |
| 108 | 1126.7 | 0.000 | 108 | 1114.8 | 0.001 | 108 | 1098.4 | 0.000 |
| 109 | 1133.7 | 0.000 | 109 | 1130.5 | 0.001 | 109 | 1114.7 | 0.000 |
| 110 | 1136.5 | 0.001 | 110 | 1135.9 | 0.001 | 110 | 1116.4 | 0.001 |
| 111 | 1138.7 | 0.001 | 111 | 1137.2 | 0.001 | 111 | 1132.2 | 0.000 |
| 112 | 1144.7 | 0.000 | 112 | 1142.5 | 0.001 | 112 | 1134.3 | 0.000 |
| 113 | 1152.1 | 0.000 | 113 | 1146.2 | 0.001 | 113 | 1141.9 | 0.000 |
| 114 | 1157.8 | 0.000 | 114 | 1155.6 | 0.000 | 114 | 1147.0 | 0.001 |
| 115 | 1174.3 | 0.001 | 115 | 1168.3 | 0.000 | 115 | 1155.6 | 0.000 |
| 116 | 1177.8 | 0.000 | 116 | 1178.1 | 0.000 | 116 | 1160.6 | 0.000 |
| 117 | 1178.8 | 0.000 | 117 | 1178.7 | 0.000 | 117 | 1162.3 | 0.000 |
| 118 | 1187.4 | 0.000 | 118 | 1183.5 | 0.000 | 118 | 1178.5 | 0.000 |
| 119 | 1199.1 | 0.000 | 119 | 1195.1 | 0.000 | 119 | 1179.2 | 0.000 |
| 120 | 1203.1 | 0.000 | 120 | 1196.7 | 0.001 | 120 | 1194.2 | 0.000 |
| 121 | 1211.0 | 0.000 | 121 | 1205.6 | 0.001 | 121 | 1202.7 | 0.000 |
| 122 | 1212.9 | 0.001 | 122 | 1207.9 | 0.001 | 122 | 1205.6 | 0.000 |
| 123 | 1223.6 | 0.001 | 123 | 1212.9 | 0.001 | 123 | 1210.9 | 0.000 |
| 124 | 1227.4 | 0.000 | 124 | 1223.4 | 0.002 | 124 | 1213.4 | 0.000 |
| 125 | 1234.7 | 0.001 | 125 | 1230.5 | 0.001 | 125 | 1224.5 | 0.000 |

Continued on next page

**Table 21 continued from previous page**

| Mode | $\nu_i@T_1$ | $S_1$-$T_1$ | Mode | $\nu_i@T_2$ | $S_1$-$T_2$ | Mode | $\nu_i@T_2$ | $S_1$-$T_3$ |
|---|---|---|---|---|---|---|---|---|
| 126 | 1241.1 | 0.001 | 126 | 1234.1 | 0.001 | 126 | 1236.6 | 0.000 |
| 127 | 1244.2 | 0.000 | 127 | 1258.6 | 0.000 | 127 | 1250.5 | 0.000 |
| 128 | 1265.3 | 0.000 | 128 | 1259.5 | 0.001 | 128 | 1257.3 | 0.001 |
| 129 | 1272.5 | 0.000 | 129 | 1287.5 | 0.000 | 129 | 1264.1 | 0.000 |
| 130 | 1287.9 | 0.000 | 130 | 1288.3 | 0.000 | 130 | 1279.8 | 0.000 |
| 131 | 1289.4 | 0.000 | 131 | 1292.8 | 0.001 | 131 | 1288.8 | 0.000 |
| 132 | 1306.8 | 0.001 | 132 | 1305.3 | 0.001 | 132 | 1293.9 | 0.000 |
| 133 | 1310.4 | 0.001 | 133 | 1307.9 | 0.001 | 133 | 1303.3 | 0.001 |
| 134 | 1311.5 | 0.000 | 134 | 1323.7 | 0.001 | 134 | 1307.5 | 0.000 |
| 135 | 1325.5 | 0.000 | 135 | 1326.8 | 0.000 | 135 | 1318.0 | 0.001 |
| 136 | 1331.3 | 0.000 | 136 | 1341.8 | 0.001 | 136 | 1323.4 | 0.001 |
| 137 | 1343.1 | 0.000 | 137 | 1358.6 | 0.001 | 137 | 1325.1 | 0.001 |
| 138 | 1346.8 | 0.001 | 138 | 1365.4 | 0.002 | 138 | 1331.0 | 0.000 |
| 139 | 1362.2 | 0.001 | 139 | 1371.6 | 0.000 | 139 | 1345.1 | 0.000 |
| 140 | 1372.6 | 0.001 | 140 | 1377.2 | 0.000 | 140 | 1368.3 | 0.000 |
| 141 | 1379.0 | 0.000 | 141 | 1379.2 | 0.001 | 141 | 1372.8 | 0.001 |
| 142 | 1383.6 | 0.000 | 142 | 1389.6 | 0.000 | 142 | 1378.3 | 0.000 |
| 143 | 1389.6 | 0.001 | 143 | 1397.2 | 0.001 | 143 | 1385.9 | 0.000 |
| 144 | 1394.1 | 0.000 | 144 | 1398.2 | 0.000 | 144 | 1390.5 | 0.000 |
| 145 | 1396.3 | 0.001 | 145 | 1401.8 | 0.000 | 145 | 1393.8 | 0.000 |
| 146 | 1398.4 | 0.000 | 146 | 1406.9 | 0.000 | 146 | 1397.8 | 0.000 |

Continued on next page

**Table 21 continued from previous page**

| Mode | $\nu_i@T_1$ | $S_1$-$T_1$ | Mode | $\nu_i@T_2$ | $S_1$-$T_2$ | Mode | $\nu_i@T_2$ | $S_1$-$T_3$ |
|---|---|---|---|---|---|---|---|---|
| 147 | 1400.6 | 0.000 | 147 | 1413.9 | 0.000 | 147 | 1398.3 | 0.000 |
| 148 | 1413.4 | 0.000 | 148 | 1418.1 | 0.000 | 148 | 1407.1 | 0.001 |
| 149 | 1417.6 | 0.000 | 149 | 1427.1 | 0.001 | 149 | 1411.8 | 0.000 |
| 150 | 1423.1 | 0.000 | 150 | 1431.8 | 0.000 | 150 | 1416.7 | 0.000 |
| 151 | 1435.7 | 0.000 | 151 | 1440.2 | 0.000 | 151 | 1424.2 | 0.000 |
| 152 | 1442.3 | 0.000 | 152 | 1446.1 | 0.000 | 152 | 1430.7 | 0.001 |
| 153 | 1447.3 | 0.000 | 153 | 1447.6 | 0.000 | 153 | 1443.2 | 0.000 |
| 154 | 1449.7 | 0.000 | 154 | 1450.1 | 0.001 | 154 | 1446.3 | 0.000 |
| 155 | 1450.2 | 0.000 | 155 | 1452.2 | 0.000 | 155 | 1448.6 | 0.000 |
| 156 | 1451.6 | 0.000 | 156 | 1455.5 | 0.000 | 156 | 1454.2 | 0.000 |
| 157 | 1454.2 | 0.000 | 157 | 1455.5 | 0.001 | 157 | 1454.9 | 0.000 |
| 158 | 1456.2 | 0.000 | 158 | 1458.4 | 0.000 | 158 | 1455.9 | 0.000 |
| 159 | 1456.9 | 0.000 | 159 | 1458.8 | 0.000 | 159 | 1456.9 | 0.000 |
| 160 | 1457.9 | 0.000 | 160 | 1459.3 | 0.000 | 160 | 1458.6 | 0.000 |
| 161 | 1458.1 | 0.000 | 161 | 1462.4 | 0.000 | 161 | 1459.4 | 0.000 |
| 162 | 1463.0 | 0.001 | 162 | 1463.8 | 0.000 | 162 | 1461.3 | 0.000 |
| 163 | 1464.1 | 0.000 | 163 | 1464.7 | 0.000 | 163 | 1461.5 | 0.000 |
| 164 | 1464.4 | 0.001 | 164 | 1465.5 | 0.000 | 164 | 1462.7 | 0.000 |
| 165 | 1464.8 | 0.000 | 165 | 1466.0 | 0.000 | 165 | 1464.0 | 0.000 |
| 166 | 1465.7 | 0.000 | 166 | 1466.2 | 0.000 | 166 | 1464.3 | 0.000 |
| 167 | 1466.1 | 0.000 | 167 | 1466.4 | 0.000 | 167 | 1464.7 | 0.000 |

Continued on next page

**Table 21 continued from previous page**

| Mode | $\nu_i@T_1$ | $S_1$-$T_1$ | Mode | $\nu_i@T_2$ | $S_1$-$T_2$ | Mode | $\nu_i@T_2$ | $S_1$-$T_3$ |
|---|---|---|---|---|---|---|---|---|
| 168 | 1466.3 | 0.000 | 168 | 1467.4 | 0.000 | 168 | 1466.2 | 0.000 |
| 169 | 1467.4 | 0.000 | 169 | 1470.2 | 0.000 | 169 | 1467.1 | 0.000 |
| 170 | 1478.0 | 0.000 | 170 | 1473.9 | 0.000 | 170 | 1473.1 | 0.000 |
| 171 | 1482.8 | 0.000 | 171 | 1478.4 | 0.000 | 171 | 1474.6 | 0.001 |
| 172 | 1484.1 | 0.000 | 172 | 1483.5 | 0.000 | 172 | 1477.9 | 0.000 |
| 173 | 1486.3 | 0.001 | 173 | 1484.3 | 0.000 | 173 | 1479.3 | 0.001 |
| 174 | 1490.4 | 0.001 | 174 | 1488.4 | 0.000 | 174 | 1483.9 | 0.000 |
| 175 | 1517.9 | 0.001 | 175 | 1532.9 | 0.000 | 175 | 1487.5 | 0.000 |
| 176 | 1538.0 | 0.001 | 176 | 1551.2 | 0.001 | 176 | 1500.7 | 0.001 |
| 177 | 1547.4 | 0.001 | 177 | 1559.2 | 0.000 | 177 | 1507.8 | 0.000 |
| 178 | 1556.8 | 0.000 | 178 | 1600.6 | 0.000 | 178 | 1532.6 | 0.000 |
| 179 | 1576.1 | 0.001 | 179 | 1620.6 | 0.000 | 179 | 1589.5 | 0.000 |
| 180 | 1600.0 | 0.001 | 180 | 1629.2 | 0.001 | 180 | 1622.8 | 0.000 |
| 181 | 1632.3 | 0.001 | 181 | 1661.5 | 0.000 | 181 | 1634.2 | 0.001 |
| 182 | 1642.4 | 0.002 | 182 | 1705.8 | 0.000 | 182 | 1644.7 | 0.000 |
| 183 | 1677.3 | 0.002 | 183 | 1720.4 | 0.000 | 183 | 1663.1 | 0.000 |
| 184 | 1720.7 | 0.000 | 184 | 1732.6 | 0.000 | 184 | 1667.9 | 0.000 |
| 185 | 1730.1 | 0.000 | 185 | 1818.2 | 0.000 | 185 | 1723.5 | 0.000 |
| 186 | 1733.0 | 0.001 | 186 | 1844.3 | 0.000 | 186 | 1842.0 | 0.000 |
| 187 | 1831.0 | 0.000 | 187 | 1848.9 | 0.001 | 187 | 1843.9 | 0.000 |
| 188 | 1842.7 | 0.000 | 188 | 2115.5 | 0.001 | 188 | 1858.1 | 0.000 |

Continued on next page

**Table 21 continued from previous page**

| Mode | $\nu_i@T_1$ | $S_1$-$T_1$ | Mode | $\nu_i@T_2$ | $S_1$-$T_2$ | Mode | $\nu_i@T_2$ | $S_1$-$T_3$ |
|---|---|---|---|---|---|---|---|---|
| 189 | 1851.9 | 0.000 | 189 | 2971.5 | 0.001 | 189 | 1951.0 | 0.002 |
| 190 | 3052.1 | 0.000 | 190 | 3051.3 | 0.000 | 190 | 2722.8 | 0.022 |
| 191 | 3052.1 | 0.000 | 191 | 3052.1 | 0.000 | 191 | 3042.8 | 0.000 |
| 192 | 3052.7 | 0.000 | 192 | 3052.5 | 0.000 | 192 | 3050.1 | 0.000 |
| 193 | 3054.1 | 0.000 | 193 | 3054.6 | 0.000 | 193 | 3054.3 | 0.000 |
| 194 | 3054.6 | 0.000 | 194 | 3055.0 | 0.000 | 194 | 3054.9 | 0.000 |
| 195 | 3065.8 | 0.000 | 195 | 3066.6 | 0.000 | 195 | 3056.2 | 0.000 |
| 196 | 3068.8 | 0.000 | 196 | 3072.1 | 0.000 | 196 | 3062.2 | 0.000 |
| 197 | 3071.6 | 0.000 | 197 | 3072.5 | 0.000 | 197 | 3066.1 | 0.001 |
| 198 | 3072.1 | 0.000 | 198 | 3075.8 | 0.001 | 198 | 3072.5 | 0.000 |
| 199 | 3077.6 | 0.000 | 199 | 3078.3 | 0.000 | 199 | 3073.2 | 0.000 |
| 200 | 3084.9 | 0.000 | 200 | 3086.5 | 0.000 | 200 | 3077.9 | 0.000 |
| 201 | 3093.1 | 0.000 | 201 | 3094.4 | 0.001 | 201 | 3084.4 | 0.000 |
| 202 | 3094.2 | 0.000 | 202 | 3096.9 | 0.001 | 202 | 3089.3 | 0.000 |
| 203 | 3115.0 | 0.000 | 203 | 3111.9 | 0.000 | 203 | 3091.4 | 0.000 |
| 204 | 3125.5 | 0.000 | 204 | 3120.3 | 0.000 | 204 | 3107.6 | 0.000 |
| 205 | 3125.6 | 0.000 | 205 | 3121.7 | 0.000 | 205 | 3108.9 | 0.000 |
| 206 | 3128.7 | 0.000 | 206 | 3128.2 | 0.000 | 206 | 3128.8 | 0.000 |
| 207 | 3132.8 | 0.000 | 207 | 3135.1 | 0.000 | 207 | 3133.9 | 0.000 |
| 208 | 3145.6 | 0.000 | 208 | 3141.3 | 0.000 | 208 | 3134.1 | 0.000 |
| 209 | 3145.9 | 0.000 | 209 | 3142.5 | 0.000 | 209 | 3140.4 | 0.000 |

Continued on next page

**Table 21 continued from previous page**

| Mode | $\nu_i@T_1$ | $S_1$-$T_1$ | Mode | $\nu_i@T_2$ | $S_1$-$T_2$ | Mode | $\nu_i@T_2$ | $S_1$-$T_3$ |
|---|---|---|---|---|---|---|---|---|
| 210 | 3148.2 | 0.000 | 210 | 3146.2 | 0.000 | 210 | 3144.1 | 0.000 |
| 211 | 3150.0 | 0.000 | 211 | 3149.2 | 0.000 | 211 | 3145.2 | 0.000 |
| 212 | 3151.4 | 0.000 | 212 | 3149.7 | 0.000 | 212 | 3151.3 | 0.000 |
| 213 | 3161.3 | 0.000 | 213 | 3156.9 | 0.000 | 213 | 3152.2 | 0.000 |
| 214 | 3164.4 | 0.000 | 214 | 3160.0 | 0.000 | 214 | 3152.3 | 0.000 |
| 215 | 3165.5 | 0.000 | 215 | 3164.8 | 0.000 | 215 | 3165.2 | 0.000 |
| 216 | 3167.0 | 0.000 | 216 | 3166.6 | 0.000 | 216 | 3166.4 | 0.000 |
| 217 | 3170.4 | 0.000 | 217 | 3170.4 | 0.000 | 217 | 3168.1 | 0.000 |
| 218 | 3175.0 | 0.000 | 218 | 3171.5 | 0.000 | 218 | 3170.8 | 0.000 |
| 219 | 3188.4 | 0.000 | 219 | 3181.5 | 0.000 | 219 | 3175.7 | 0.000 |
| 220 | 3201.4 | 0.000 | 220 | 3201.5 | 0.000 | 220 | 3183.2 | 0.000 |
| 221 | 3203.2 | 0.000 | 221 | 3202.2 | 0.000 | 221 | 3201.9 | 0.000 |
| 222 | 3229.0 | 0.000 | 222 | 3231.2 | 0.000 | 222 | 3204.0 | 0.000 |
| 223 | 3235.2 | 0.000 | 223 | 3246.8 | 0.000 | 223 | 3227.7 | 0.001 |
| 224 | 3237.4 | 0.000 | 224 | 3248.2 | 0.000 | 224 | 3229.5 | 0.000 |
| 225 | 3281.9 | 0.000 | 225 | 3271.6 | 0.000 | 225 | 3239.9 | 0.001 |
| 226 | 3529.6 | 0.000 | 226 | 3431.2 | 0.000 | 226 | 3276.6 | 0.000 |
| 227 | 3635.4 | 0.000 | 227 | 3596.2 | 0.000 | 227 | 3515.7 | 0.001 |
| - | - | - | - | - | - | 228 | 3652.6 | 0.002 |

**Table 22.** *The five largest coupling vibrational normal modes calculated at their own $T_n(\pi\rightarrow\pi^*)$ minimum of methylpheophorbide a (MPh).*

| ISC $S_1(\pi\rightarrow\pi^*) \rightsquigarrow T_1(\pi\rightarrow\pi^*)$ | ISC $S_1(\pi\rightarrow\pi^*) \rightsquigarrow T_2(\pi\rightarrow\pi^*)$ | ISC $S_1(\pi\rightarrow\pi^*) \rightsquigarrow T_3(\pi\rightarrow\pi^*)$ |
|---|---|---|
| 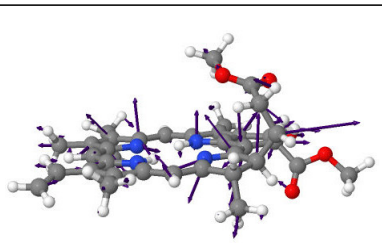 | 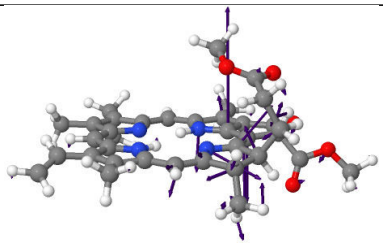 | 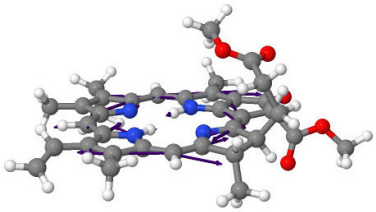 |
| 47 | 72 | 190 |
| 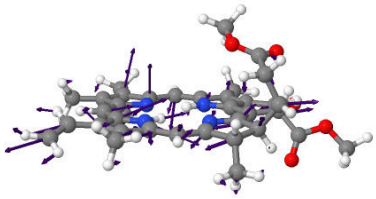 | 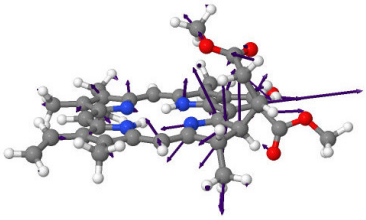 | 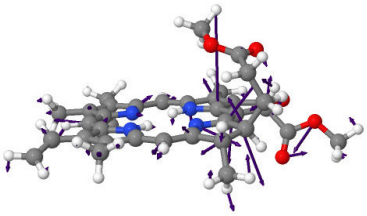 |
| 46 | 47 | 74 |
| 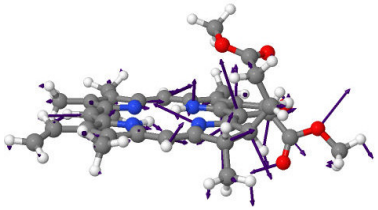 | 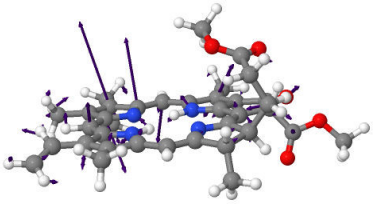 | 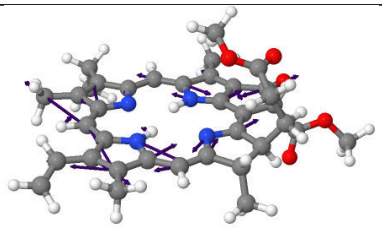 |
| 75 | 48 | 189 |
| 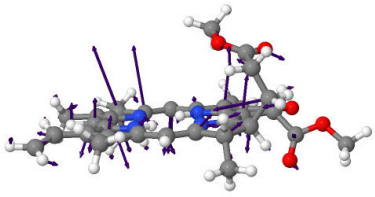 | 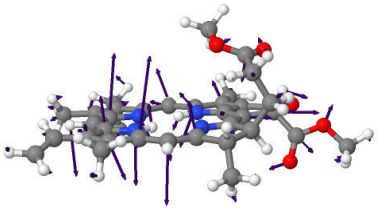 | 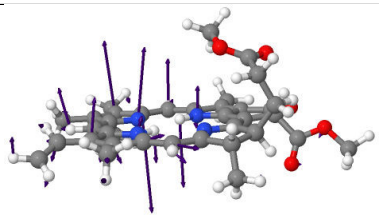 |
| 48 | 66 | 70 |

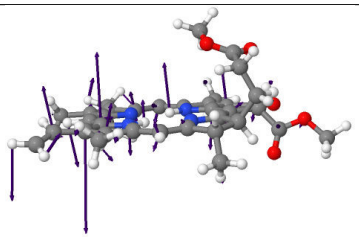

72

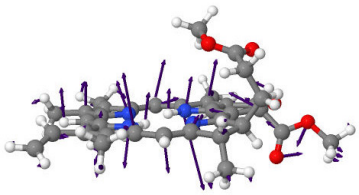

64

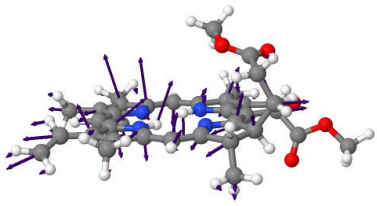

47

**Table 23.** *Effect of the Gaussian linewidth on the ISC rate constants $k_{ISC}$ ($s^{-1}$) at room temperature.*

| Channel | Parameters | | Results |
|---|---|---|---|
| | $E_{ST}$ (eV) | Gaussian linewidth ($cm^{-1}$) | $k_{ISC}^{FCHT}$ ($s^{-1}$) |
| $S_1 \rightsquigarrow T_1$ | 0.92 | 0.1 | 7.10 x $10^6$ |
| $S_1 \rightsquigarrow T_1$ | 0.92 | 1.0 | 7.10 x $10^6$ |
| $S_1 \rightsquigarrow T_1$ | 0.92 | 10.0 | 7.10 x $10^6$ |
| $S_1 \rightsquigarrow T_1$ | 0.92 | 100.0 | 7.11 x $10^6$ |
| $S_1 \rightsquigarrow T_2$ | 0.59 | 0.1 | 2.08 x $10^7$ |
| $S_1 \rightsquigarrow T_2$ | 0.59 | 1.0 | 2.08 x $10^7$ |
| $S_1 \rightsquigarrow T_2$ | 0.59 | 10.0 | 2.08 x $10^7$ |
| $S_1 \rightsquigarrow T_2$ | 0.59 | 100.0 | 2.11 x $10^7$ |
| $S_1 \rightsquigarrow T_3$ | 0.13 | 0.1 | 3.32 x $10^7$ |
| $S_1 \rightsquigarrow T_3$ | 0.13 | 1.0 | 3.34 x $10^7$ |
| $S_1 \rightsquigarrow T_3$ | 0.13 | 10.0 | 3.35 x $10^7$ |
| $S_1 \rightsquigarrow T_3$ | 0.13 | 100.0 | 3.39 x $10^7$ |

**Table 24.** *Effect of the number of roots on the ISC rate constant $k_{ISC}$.*

| Number of roots | Channel | Result $k_{ISC}^{FCHT}$ ($s^{-1}$) |
|---|---|---|
| 5 | $S_1 \rightsquigarrow T_1$ | 7.11 x $10^6$ |
| 15 | $S_1 \rightsquigarrow T_1$ | 7.11 x $10^6$ |
| 25 | $S_1 \rightsquigarrow T_1$ | 7.11 x $10^6$ |
| 5 | $S_1 \rightsquigarrow T_2$ | 2.08 x $10^7$ |
| 15 | $S_1 \rightsquigarrow T_2$ | 2.08 x $10^7$ |
| 25 | $S_1 \rightsquigarrow T_2$ | 2.08 x $10^7$ |
| 5 | $S_1 \rightsquigarrow T_3$ | 3.35 x $10^7$ |
| 15 | $S_1 \rightsquigarrow T_3$ | 3.35 x $10^7$ |
| 25 | $S_1 \rightsquigarrow T_3$ | 3.35 x $10^7$ |